

© 2018

Raymond Raphael Fullon

ALL RIGHTS RESERVED

# Investigation into the active sites for two dimensional electrocatalysts

by

Raymond Raphael Fullon

A Dissertation submitted to the

School of Graduate Studies

Rutgers, The State University of New Jersey

in partial fulfillment of the requirements

for the degree of

Doctor of Philosophy

Graduate Program in Materials Science & Engineering

written under the direction of

Professor Manish Chhowalla

and approved by

---

---

---

---

New Brunswick, New Jersey

October, 2018

# **ABSTRACT OF THE DISSERTATION**

Investigation into the active sites for two dimensional electrocatalysts

By RAYMOND RAPHAEL FULLON

Dissertation Director:

Prof. Manish Chhowalla

Two dimensional (2D) materials are an exceptional class of materials that have many remarkable optoelectronic, mechanical, and chemical properties. In combination with the layered structure of 2D materials, they allow us many opportunities and scientific pathways to explore. The most well-known 2D material, graphene, has been widely studied and researched and found to be a single atomically thin nanosheet of carbon in the lateral dimension. Due to the high cost of synthesizing graphene, alternatives have been investigated that allow for solution processing such as graphene oxide suspensions in water. Recently, a class of 2D materials beyond graphene have been of significant interest, transition metal dichalcogenides (TMDs) due to their varied ability to be

semiconducting, insulating or metallic. 2D materials have found applications in electronics, electrochemistry, superconducting, photovoltaics and many more.

As global demand for energy increases, it is clear that depending on fossil fuels is not sustainable. In order to combat our fossil fuel dependence, cost effective and efficient alternatives must be found such as hydrogen powered fuel cells. However, the high cost of producing hydrogen and catalysts found in fuel cells have prevents its commercialization. Developing cost-effective and high performing catalysts that can electrocatalytically produce hydrogen and can function within fuel cells are imperative for realizing this alternative fuel.

2D materials such as  $\text{MoS}_2$  and graphene oxide have recently been shown to be active for the hydrogen evolution reaction (HER) and the oxygen reduction reaction (ORR), respectively. In any electrocatalytic reaction, the active site is a location on the catalyst where the reaction takes place. Determining the active site and its location is challenging, as electrocatalytic reactions occur on such a small scale and it can be difficult to isolate from external influences. Insight into the active site is crucial for using these materials in electrocatalysis, as a fundamental understanding of the active site yields the best routes to developing high performing catalysts.

In this thesis, we developed a method of fabrication electrochemical microcells on individual monolayers of 2D materials using electron beam lithography. These microcells allow us to electrochemically test 2D materials for electrocatalytic reactions. We first developed this method on 2D  $\text{MoS}_2$  grown by chemical vapor deposition. Using this method, we measured the electrocatalytic performance of the edge and, previously thought to be inactive, basal plane of 2D  $\text{MoS}_2$ , and found no relationship between edges

and HER activity. Investigation into the contact resistance of our microcell devices yielded important insight into its importance in HER measurements. When the contact resistance is decreased, the electrocatalytic performance was enhanced. If sufficiently decreased, the basal plane of MoS<sub>2</sub> was found to have high performance for the HER. In addition, we have recently developed a microwave reduction process to achieve high quality graphene oxide with high graphene character. Microwave reduced graphene oxide (MWrGO) was doped with nitrogen by annealing in ammonia (NH<sub>3</sub>) gas at elevated temperature. Defects were found to be highly important for nitrogen incorporation and once nitrogen had been incorporated into the MWrGO lattice we determined the configuration of the doped nitrogen. Our electrocatalytic results showed that when the pyridinic nitrogen bonding configuration dominates the nitrogen content, the ORR activity in acidic conditions is improved. In order to further investigate this behavior, we sought to fabricate electrochemical microcells on graphene grown by chemical vapor deposition and nitrogen doped graphene (N-graphene) doped by NH<sub>3</sub> annealing. A method for patterning the graphene was developed using negative electron beam lithography, but was found to damage N-graphene. Attempts were made to maintain the nitrogen content throughout the device processing but were not successful. Our electrocatalytic results did demonstrate that electrocatalytic measurements for the ORR could be made on CVD graphene, and is a promising technique moving forward.

## **Dedication**

To Pauleen, without your love and unwavering support I would never have made it here.

To my family, you have all been there for me whenever I needed help; whether it be pagkain or payo.

To Lola Lydia, merong Dr. Fullon na!

## **Acknowledgements**

While some may claim that this accomplishment is my own, there are many individuals without whom this would not have been possible.

I would like to begin by thanking my thesis advisor, Prof. Manish Chhowalla. During my time here at Rutgers University, Prof. Chhowalla has guided me, sometimes with a necessary forceful hand, and trained me to be a better scientist. He has given me an immeasurable number of skills and lessons in both science and life, the first and foremost of which is to always ask the right questions and focus on the fundamentals. From amazing life stories to scientific training to consistent support, Prof. Chhowalla has been the guiding force behind my successful and productive experience at Rutgers.

I would like to acknowledge my parents, Ramon and Lourdes Fullon. I thank my dad for my amazing sense of humor, instilling in me a curiosity in science and technology when I was young and for teaching me patience and service. I thank my mom for instilling in me my diligent work ethic and consistent push to prioritize my education and for always knowing what to say when I need it. I would like to thank my older sisters, Ate Michele Fullon, Ate Carissa Fullon and Ate Isabel McCarthy, for their support over the years and not treating me too terribly as the bunso. I thank the entirety of my family, including my brother-in-law, Johnny McCarthy and my niece and godsons, James, Maddie and Gabriel, for their steadfast encouragement and loving support during this process that was brand new for all of us.

I thank Dr. Damien Voiry, a Post-Doc in our group, for being my research mentor, teaching me the nitty gritty of research in 2D materials and how to make my figures look

beautiful. He has shown me how to be a true chemist and materials scientist, as well as a fast runner. In addition, I thank Dr. Jieun Yang, another Post-Doc in our group, for teaching me much of what I know and understand about carbon materials as well as our weekly coffee commiserations about how things never work in the lab. I would also like to thank previous and present members of the Nano-Devices and Materials group for their collaborative spirit, scientific support, and mutual suffering and happiness during the approximately 18,000 hours spent in the lab over the past few years. This includes: Dr. Cecilia C. C. Silva, Dr. Rajesh Kappera, Dr. Muharrem Acerce, Daniel Kaplan, Tristan Turner, Calvin Lee, Elisa Kowk, Dustin Ng, Daniel Kondracki, Wesley Jen, Dr. Sol Torrel, Dr. Ibrahim Bozkurt, Jacob Kupferberg, Yan Wang, Jessica Johnson, Michaela Csorny, Anne Cardenas, Vandana Gollarhalli, Brian MacDowall, Dr. Bangjun Guo, Dr. Abdul Rahman Mohmad, Dr. Xiuju Song, Dr. Shengwen Liu, and Ryan Crichton. I would like to thank the many graduate students and post-docs who have offered support and advice in and outside of science. This includes: Dr. Christopher Petoukhoff, Dr. Zeqing Shen, Dr. Catrice Carter, Dr. Riyanka Pai, Dr. Paul Kim, Dr. Nicholas Faenza, Dr. Subhabrata Bera, Dr. Joseph Prati, Dr. Rut Rivera, Elaheh Taghaddos, Ross Rucker, Shawn Ward, Arya Tewatia and Ted Tsoulos.

Part of the device work in this thesis was performed during my time at Los Alamos National Laboratory. I thank Dr. Aditya Mohite and Dr. Gautam Gupta for the opportunity to work in their lab and their support during this time. Thank you to my fellow visiting graduate students, Dr. Kunttal Keyshar, Dr. Jing Zhang and Dr. Fangze Liu, and Dr. Navaneetha Subbaiyan for making the experience worthwhile and fun.



I am thankful for all of the administrative staff in the Materials Science & Engineering department who have helped me ensure I stay on track, including Claudia Kuchinow, Nancy Pamula, Nahed Assal, Sheela Sekhar and Michelle Sole. I would like to recognize my thesis committee members, Prof. Lisa Klein, Prof. Deirdre O'Carroll and Prof. Tewodros Asefa. I thank you all for serving on my committee and your time in reviewing my thesis and participating in my defense.

Finally, I am profoundly indebted and express my deepest gratitude to my fiancée, Pauleen Kate Ocampo. None of this would have been possible without her love and infinite support as my number one fan. Pauleen was an endless well of encouragement and support, even when the hours were long, experiments occupied the vast majority of my time and when the pursuit of science took me to New Mexico. It takes a special kind of strength and fortitude to be in a relationship with a research focused graduate student. I would not be here without her.

## Table of Contents

<b>Abstract .....</b>	<b>ii</b>
<b>Dedication.....</b>	<b>v</b>
<b>Acknowledgements.....</b>	<b>vi</b>
<b>List of Figures .....</b>	<b>xiii</b>
<b>Chapter 1. Introduction.....</b>	<b>1</b>
1.1 Motivation .....	1
1.2 Objectives of Work .....	3
1.3 Organization of the Thesis .....	4
<b>Chapter 2. Two Dimensional Materials .....</b>	<b>6</b>
2.1 Graphene & Graphene Oxide.....	7
2.1.1 Reduction of Graphene Oxide .....	9
2.1.2 Nitrogen doping of Graphene & Graphene Oxide.....	12
2.2 Transition Metal Dichalcogenides .....	14
2.3.1 Phase Transition in MoS <sub>2</sub> .....	16
2.4 Synthesis of Two Dimensional Materials .....	18
2.4.1 Top-down approach.....	18
2.4.2 Bottom-up approach .....	21

2.5 Characterization .....	22
2.5.1 Raman Spectroscopy in Graphene & Graphene Oxide .....	22
2.5.2 Raman spectroscopy in MoS <sub>2</sub> .....	24
2.5.3 X-Ray Photoelectron Spectroscopy (XPS).....	27
<b>Chapter 3. Electrochemistry .....</b>	<b>30</b>
3.1 Water Electrolysis .....	33
3.1.1 Molybdenum Disulfide for the Hydrogen Evolution Reaction .....	35
3.1.2 Mechanism of the HER on Molybdenum Disulfide .....	39
3.2 Fuel Cells and the Oxygen Reduction Reaction.....	41
3.2.1 Graphene catalysts for the Oxygen Reduction Reaction .....	43
3.2.2 Mechanism of the Oxygen Reduction Reaction on Nitrogen doped Graphene .....	46
<b>Chapter 4. Experimental Methods .....</b>	<b>52</b>
4.1 Synthesis.....	52
4.2 Electrochemical Characterization .....	56
4.3 Electron Beam Lithography & Device Fabrication .....	62
<b>Chapter 5. Electrochemical Microcells on 2D MoS<sub>2</sub> nanosheets</b>	
<b>.....</b>	<b>65</b>
5.1 Physical Characterization of 2D MoS <sub>2</sub> .....	66
5.2 Devices with 1T Phase Contacts .....	69

5.3 Devices for Electrochemical Microcells with 2D MoS <sub>2</sub> .....	71
5.4 Microcell Electrochemical Measurements .....	74
<b>Chapter 6. Electrochemical Characterization of 2D MoS<sub>2</sub> for the Hydrogen Evolution Reaction .....</b>	<b>76</b>
6.1 Electrochemical Impedance Spectroscopy .....	76
6.2 Electrocatalytic Performance of 2D MoS <sub>2</sub> .....	78
6.3 Contact Resistance and Electrocatalytic Performance for the Hydrogen Evolution Reaction.....	80
6.4 Sulfur Vacancies as the Active Site for the Hydrogen Evolution Reaction in 2D MoS <sub>2</sub> .....	82
6.5 Conclusions .....	84
<b>Chapter 7. Nitrogen doped Microwaved Reduced Graphene Oxide for the Oxygen Reduction Reaction .....</b>	<b>86</b>
7.1 High Quality Graphene via Microwave Reduction.....	86
7.2 NH <sub>3</sub> Annealing of MWrGO .....	89
7.3 Physical Characterization of N-MWrGO .....	90
7.4 Preparation of N-MWrGO Ink for Electrocatalysis .....	95
7.5 Electrocatalytic Performance for the ORR of N-MWrGO.....	98
7.7 Conclusions .....	104

## **Chapter 8. Nitrogen-Doped Graphene for the Oxygen**

### **Reduction Reaction .....106**

8.1 NH <sub>3</sub> Annealing of Graphene .....	106
8.2 Physical Characterization of N-Graphene .....	107
8.3 Patterning of N-graphene .....	110
8.4 Electrocatalytic Performance of N-Graphene Electrochemical Microcells .....	113
8.5 Optimization of Electrochemical Microcells on N-graphene .....	115
8.6 Maintaining Nitrogen in N-Graphene .....	121
8.6.1 Annealing Patterned Graphene in NH <sub>3</sub> .....	121
8.6.2 Open Windows without Patterning N-Graphene .....	123
8.7 Conclusions .....	129

### **Chapter 9. Future Work and Conclusions .....131**

9.1 Future Work .....	131
9.1.1 Nitrogen Bonding Configuration in Graphene based Materials .....	131
9.1.2 Electrochemical activity of other 2D Materials .....	131
9.1.3 Beyond Electrochemistry .....	132
9.2 Conclusions .....	133

### **References .....138**

### **Appendix. Acknowledgement of Previous Publications.....149**

## List of Figures

<b>2.1</b>	(a) Bulk layered materials molybdenum sulfide and graphite <sup>26</sup> and corresponding (b) single layer forms of molybdenum sulfide and graphene. <sup>26</sup> Blue, yellow and black spheres represent molybdenum, sulfur and carbon atoms, respectively	6
<b>2.2</b>	The different methods for graphene production of varying quality and their corresponding cost. In parentheses, the main applications of each production method are listed.	8
<b>2.3</b>	Nanosheets of graphene oxide (GO) are composed of carbon sheets that have been functionalized by several different functional groups such as epoxide, hydroxyl, carbonyl and carboxylic groups.	9
<b>2.4</b>	(a) Initial sheet of GO before any reduction. (b) High temperature annealing can reduce GO, however it also stabilizes some functional groups and creates holes and defects. <sup>87</sup> Electrical characteristics (c) before reduction and (d) after varying amounts of time being exposed to hydrazine and hydrogen plasma <sup>82</sup>	10
<b>2.5</b>	Nitrogen can incorporate into graphene material in three main bonding configurations: (a) pyridinic, (b) pyrrolic and (c) graphitic.	12
<b>2.6</b>	(a) Transfer characteristics of pristine graphene at a drain-source voltage ( $V_{sd}$ ) of -0.5 V in comparison to nitrogen doped graphene at $V_{sd}$ of 0.5 V and 1.0 V. N-graphene exhibits clear n-type behavior (b) Current-gate voltage curves of a device containing GO annealed in $NH_3$ at 900 °C. The was measured in air (red), vacuum (green) and in vacuum after electrical annealing (blue) to remove physisorbed oxygen	14
<b>2.7</b>	Representative structure of a transition metal dichalcogenides where M is a transition metal and X is a chalcogen atom.	15
<b>2.8</b>	Theoretically calculated band structures of (a) bulk $MoS_2$ , (b) quadrilayer $MoS_2$ (c) bilayer $MoS_2$ and (d) monolayer $MoS_2$ . Solid arrows indicate the lowest energy transition available within the band structure.	16
<b>2.9</b>	Crystal structure of (a) 2H and (b) 1T polymorphs for TMDs	17
<b>2.10</b>	Mechanical exfoliation of graphite to yield graphene. (a) Adhesive tape is applied to a sample of HOPG crystal. (b) As the tape is pulled off of the HOPG crystal a few layers are mechanically exfoliated as they stick to the tape. (c) The tape with a few layers of graphene is pressed onto a target substrate (d) and as the tape is pulled off of the target substrate, the bottom layer remains on the substrate to yield a clean monolayer.	18
<b>2.11</b>	(a) Schematic of the synthesis of GO showing oxidation and exfoliation to yield GO sheets.(b) Dispersions of transition metal dichalcogenides nanosheets in water synthesized using organometallic chemistry.	20

<b>2.12</b>	(a) Typical Raman spectra of graphite, monolayer graphene (1LG), three layer graphene (3LG), disordered graphene, graphene oxide and nanographene. (b) Molecular schematic showing the $E_{2g}$ vibrational mode in graphene. <sup>149</sup> (c) The breathing mode found in graphene	23
<b>2.13</b>	(a) Evolution of Raman spectra of as-deposited 1T MoS <sub>2</sub> to 2H MoS <sub>2</sub> as annealing temperature increases. Pristine bulk and monolayer MoS <sub>2</sub> are included as a reference. Characteristic peaks for 2H and 1T phase MoS <sub>2</sub> can be seen. (b) Raman spectra for varying layers of MoS <sub>2</sub> . The separation between the two main vibrational modes of MoS <sub>2</sub> , $E_{2g}^1$ and $A_{1g}$ , decreases with the number of layers	25
<b>2.14</b>	Increase in PL intensity as the thickness of the MoS <sub>2</sub> layer decreases down to a monolayer <sup>123</sup>	26
<b>2.15</b>	(a) C1s spectra from XPS for GO and rGO that had undergone different levels of reduction. The main oxygen functional groups for GO are labeled in each of the GO samples. (b) A typical N1s spectra from XPS for nitrogen doped graphene species. The different nitrogen bonding configurations are labeled at their respective binding energy.	28
<b>2.16</b>	A typical (a) Mo 3d and (b) S 2p spectra for exfoliated MoS <sub>2</sub> . The peaks can be deconvoluted in order to determine the concentration of the 1T and 2H phase.	29
<b>3.1</b>	A classic example of an electrolytic cell. Copper ions are reduced at the cathode to form copper metal while water is oxidized at the anode producing oxygen and hydrogen ions. Electrons are supplied to the cell by an external circuit to drive the reaction	31
<b>3.2</b>	A standard three electrode cell will contain a working electrode, reference electrode and counter electrode within a glass enclosure. Holes for gas purging are also found along the top of the cell.	32
<b>3.3</b>	Electrolyzers will split water into its main components of hydrogen and oxygen. OER occurs at the anode for the production of oxygen gas while HER is at the cathode for the reduction of protons to hydrogen gas. Ideal electrolyzers will use a membrane to facilitate the flow of protons and prevent mixing of the gases.	33
<b>3.4</b>	(a) Polarization curves of MoS <sub>2</sub> samples grown on gold substrates after sintering at 400 °C and 550 °C (b) Evolution of the exchange current density as a function of the MoS <sub>2</sub> area coverage (c) Demonstration of the direct relationship found between the MoS <sub>2</sub> edge length and exchange current density <sup>18</sup>	36
<b>3.5</b>	(a) Polarization curves of 2H and 1T phase MoS <sub>2</sub> prepared by chemical exfoliation. Edge oxidized counterparts are also shown. (b) Tafel analysis of the corresponding polarization curves for 2H and 1T phase MoS <sub>2</sub> and their edge oxidized counterparts.	38
<b>3.6</b>	Schematic operation of a hydrogen-oxygen fuel cell	41

<b>3.7</b>	Rotating Ring Disk Electrode measurements for the ORR in air-saturated 0.1 M KOH of graphene, Pt/C and N-Graphene	44
<b>3.8</b>	The common nitrogen dopant configurations in graphitic carbons and their corresponding XPS energies used for identification	46
<b>3.9</b>	Simulated structure of the 4 electron transfers during the ORR on nitrogen doped graphene. <b>(a)</b> Initialized position of the OOH above the nitrogen doped graphene. <b>(b)</b> Adsorption of the OOH <b>(c)</b> The O-O is broken and hydroxide molecules are formed <b>(d)</b> A water molecule is generated by interaction with H <sup>+</sup> with one hydroxide molecule. <b>(e)</b> The final water molecule is generated. Gray, blue, red and small white spheres represent carbon, nitrogen, oxygen, and hydrogen atoms, respectively.	48
<b>4.1</b>	<b>(a)</b> A digital image of a tube furnace with gas line connections. In order to demonstrate the apparatus, a schematic of CVD growth is superimposed. Graphene is shown above MoS <sub>2</sub> growth. <b>(b)</b> An example of the graphene after it has been transferred from the copper foil growth substrate to SiO <sub>2</sub> /Si substrate. <b>(c)</b> Triangular MoS <sub>2</sub> samples after transferring from the SiO <sub>2</sub> /Si growth substrate to higher quality SiO <sub>2</sub> /Si substrates for device fabrication	55
<b>4.2</b>	<b>(a)</b> A typical cyclic voltammagram for an ideal reversible reaction demonstrating the regions where oxidation and reduction occur. <b>(b)</b> Polarization curves that have been extracted from ideal catalysts for the water splitting reactions (OER and HER) and the fuel cell reactions (HOR and ORR).	57
<b>4.3</b>	<b>(a)</b> A rotating rind disk electrode (RRDE) is composed of a disk electrode in the center with a concentric ring electrode. The two electrode are separated by an insulating material and are both can be contacted independently. <b>(b)</b> Polarization curves that can be extracted from data measured using an RRDE setup. Current density measured at the disk can be differentiated from current measured at the ring as shown	59
<b>4.4</b>	A typical Nyquit plot showign the impedance for an electrochemical system. Regions where the kinetics of the reaction or the mass transfer in the electrochemical system control the impedance are shown at high and low frequencies, respectively	61
<b>4.5</b>	A standard workflow used in electron beam lithography for transferring a pattern written by the electron beam to the substrate. In this case the pattern is written and the underlying substrate is etched. When the resist is removed or washed away, the etched pattern remains on the substrate	62
<b>4.6</b>	Completed electronic devices on <b>(a)</b> mechanically exfoliated MoS <sub>2</sub> and <b>(b)</b> CVD grown graphene. Two contacts are deposited in order to electrically probe the materials.	64



<b>5.1</b>	(a) Raman spectra for the samples of our CVD grown MoS <sub>2</sub> demonstrate that they are single layer. A few layer spectra is also included for reference. (b) A PL spectrum for our CVD MoS <sub>2</sub> shows a high intensity, indicating that our single layer MoS <sub>2</sub> exhibits a direct band gap.	66
<b>5.2</b>	XPS spectra for the (a) Mo 3d and (b) S 2p demonstrate that our MoS <sub>2</sub> samples are free of impurities such as oxides and are in the 2H phase.	67
<b>5.3</b>	(a) Large-area SEM images of our as grown CVD MoS <sub>2</sub> samples. (b) Higher magnification SEM images shows individual nanosheets with sharp edges.	68
<b>5.4</b>	AFM image of a CVD grown MoS <sub>2</sub> nanosheet	69
<b>5.5</b>	Successive steps for the fabrication of MoS <sub>2</sub> electrochemical microcells with 1T contacts and 2H basal planes. Initially, (a) pristine MoS <sub>2</sub> is coated with PMMA (b). When exposed to the electron beam, some PMMA (c) is removed. Upon exposure to n-butyllithium (d) we can convert to the 1T phase. (e) Gold is evaporated to coat the entire sample and after lift off (f) an electrical contact to the 1T phase region of the MoS <sub>2</sub> remains. (g) Raman spectra of the 1T phase region and 2H phase region of our MoS <sub>2</sub> samples confirm the phase transition	70
<b>5.6</b>	Optical pictures showing the different steps of the microcell fabrication. (a and b) The MoS <sub>2</sub> nanosheets are transferred on the 300 nm SiO <sub>2</sub> /Si wafer and covered with PMMA. (c and d) Electrode patterns are open on the PMMA layer. (e and f) The gold electrodes are then fabricated to contact selected individual nanosheets. Each MoS <sub>2</sub> nanosheet is contacted by 2 electrodes. (g and h) The microcell is covered with PMMA (passivation layer) and windows are opened via e-beam lithography to expose solely the MoS <sub>2</sub> nanosheets	73
<b>5.7</b>	(a) Photograph of the electrochemical microcell. (b) Schematic of the electrochemical set-up showing a single layer of MoS <sub>2</sub> deposited on SiO <sub>2</sub> and contacted by one gold electrode. Glassy carbon counter electrode and Ag/AgCl reference electrode are also shown. Only the MoS <sub>2</sub> sheet is contacted with the 0.5 M H <sub>2</sub> SO <sub>4</sub> electrolyte. (c,d) Optical microscope images of the different types of microcells: (c) edge covered and (d) edge exposed.	75
<b>6.1</b>	(a) Nyquist plots showing the impedance for devices with high and low contact resistance in black and red, respectively (b) Polarization curves measured from two MoS <sub>2</sub> microcells with (solid line) and without iR correction (triangles). Curves for devices with high and low contact resistances are shown.	77
<b>6.2</b>	(a) Polarization curves obtained from MoS <sub>2</sub> devices with various contact resistances from 80 MΩ mm to 7 x 10 <sup>-2</sup> Ω mm. As contact resistance decreases, the electrocatalytic performance increases (b) Evolution of the turnover frequency (TOF) with the overpotential. Our TOF values are compared to those obtained from metallic 2H-phase MoS <sub>2</sub> edges grown on gold.	79

<b>6.3</b>	Variation of the <b>(a)</b> onset potential, <b>(b)</b> Tafel slope and the <b>(c)</b> current density measured at an overpotential of 400 mV with the contact resistance. The HER activity of the MoS <sub>2</sub> electrodes is progressively enhanced as the contact resistance decreases. No significant differences between edge-exposed and edge-covered devices have been observed from the samples, suggesting that both the surface and the edges of the MoS <sub>2</sub> crystal are active.	81
<b>6.4</b>	<b>(a)</b> STEM image of a single-layer CVD-grown MoS <sub>2</sub> nanosheet showing different types of defects: single sulfur vacancy (orange circles) and double sulfur vacancy (yellow circles). <b>(b)</b> Intensity profiles along lines L1-L3. Higher contrast is obtained from the Mo atoms compared to one sulfur atom (~30% of the Mo intensity) and two sulfur atoms (~45% of the Mo intensity). In absence of one sulfur atom (L3), the intensity decreases to <10%. <b>(c)</b> STEM image of a large-area single-layer MoS <sub>2</sub> nanosheet. The vast majority of the defects are formed by single sulfur vacancies. <b>(d)</b> The differential hydrogen adsorption energy ( $\Delta E$ ) in 2H-phase MoS <sub>2</sub> decreases significantly with an increased carrier concentration. When the carrier concentration approaches $7 \times 10^{14} \text{ cm}^{-2}$ , $\Delta E$ in 2H-phase MoS <sub>2</sub> is close to that in the 1T phase.	83
<b>7.1</b>	<b>(a)</b> A digital image of a reduced graphene oxide fiber sample before microwave reduction. The fiber is placed into a vial that has been purged with argon gas and is sealed hand tight <b>(b)</b> Digital images of the microwave reduction process. Pulses of a 1-2 seconds are applied to the vial resulting in an arc flash after a few ms of irradiation <b>(c)</b> C1s spectra obtained from x-ray photoelectron spectroscopy for graphite, CVD graphene, microwaved reduced graphene Oxide (MWrGO), reduced graphene oxide (rGO) and graphene oxide (GO). Each spectra can be deconvoluted to observe oxygen functional groups as well as the composition of the carbon-carbon bonds <b>(d)</b> Raman spectra of MWrGO and other graphene-based samples. The spectra for MWrGO is similar to the spectrum of CVD graphene with a high and symmetrical 2D band and a minimal D band.	87
<b>7.2</b>	Raman spectra obtained on MWrGO after annealing at 700 °C in ammonia (NH <sub>3</sub> ) gas for differing lengths of time. As annealing time increases the 2D peak of MWrGO continually decrease while the D peak increases, suggesting the introduction of defects and disorder as nitrogen is incorporated into the MWrGO lattice	91
<b>7.3</b>	<b>(a)</b> C1s and <b>(b)</b> N1s spectra obtained from XPS for MWrGO after annealing at 700 °C in ammonia (NH <sub>3</sub> ) gas at different lengths of time. The C1s spectra can be deconvoluted to determine the carbon composition as well as the oxygen functional group content. The C1s shows very little oxidation as annealing time increases with a slight increase in sp <sup>3</sup> hybridized carbon concentration. This implies that the defects can mostly be attributed to nitrogen incorporation. The N1s spectra can be deconvoluted into the three main nitrogen bonding configurations. Initially no nitrogen is found, but after 4 hours we see a clear distinct nitrogen peak	93

<b>7.4</b>	Evolution of the total nitrogen content and each of the nitrogen bonding configurations by atomic percent with increasing annealing time in ammonia ( $\text{NH}_3$ ) gas. Initially, very little nitrogen content is found until after 4 hours and continues to increase. At 4 and 6 hours of annealing time, the pyridinic nitrogen bonding configuration dominates until it decreases at 8 hours and the pyrrolic configuration overtakes it.	94
<b>7.5</b>	Digital image of the as-prepared N-MWrGO ink within a microcentrifuge tube	96
<b>7.6</b>	SEM images of a <b>(a)</b> MWrGO fiber as viewed down the length of the fiber and a <b>(b)</b> dropcasted thin film from the ink prepared from N-MWrGO. The fiber shows a very porous structure with large voids spread out through the structure. The dropcasted thin film has not retained its fibrous nature, instead forming a thin pockmarked film.	97
<b>7.7</b>	<b>(a)</b> Cyclic voltammograms for MWrGO and MWrGO that had been annealed in $\text{NH}_3$ for 4 hours. Voltammograms are shown for $\text{N}_2$ and $\text{O}_2$ gas saturated 0.5 M $\text{H}_2\text{SO}_4$ electrolyte. No peaks in $\text{N}_2$ gas saturated electrolyte show any increase in current, suggesting that the reaction occurring is the oxygen reduction reaction (ORR) <b>(b)</b> Polarization curves extracted from cyclic voltammograms for MWrGO and samples annealed at increasing annealing time. As annealing time increases, the onset potential shifts further positive, until after 8 hours of annealing; it shifts negative. Measurements were taken at a scan rate of 10 mV/s at a catalyst loading of 0.3 $\text{mg}/\text{cm}^2$	99
<b>7.8</b>	Hydrodynamic measurements using a rotating ring disk electrode (RRDE) on N-MWrGO at different $\text{NH}_3$ annealing time. The current density is measured at the disk while the absolute current measured at the ring is shown. Measurements were taken in $\text{O}_2$ gas saturated 0.5 M $\text{H}_2\text{SO}_4$ electrolyte at a scan rate of 5 mV/s and rotating at 800 rpm. The ring is maintained at a constant potential of 1.4 V vs RHE	102
<b>7.9</b>	Electron number (left y-axis) and percentage of $\text{H}_2\text{O}_2$ production (right y-axis) are calculated from the ratio of the disk current and ring current from the hydrodynamic voltammetry. Values are shown for N-MWrGO at different annealing time.	103
<b>8.1</b>	Raman spectra for CVD graphene and $\text{NH}_3$ annealed graphene (N-graphene). Decreases in intensity of the 2D peak and a slight increase in the D peak can be seen in the N-graphene sample due to defect and disorder being introduced into the graphene sheet.	107
<b>8.2</b>	<b>(a)</b> C1s and <b>(b)</b> N1s spectra obtained from XPS for samples of graphene and N-graphene. The C1s spectra can be deconvoluted into its carbon constituents and oxygen functional groups. There is a clear increase in the concentration of $\text{sp}^3$ hybridized carbon matching well with a large increase in nitrogen content which are likely to introduce disorder and defects into the graphene lattice. The N1s spectra is deconvoluted into the different nitrogen bonding configurations, and the pyridinic configuration was found to dominate.	109

<b>8.3</b>	Optical microscope images of the different steps of the graphene patterning process using a negative electron beam resist. <b>(a)</b> The initial sample after N-graphene is transferred to the pre-patterned chip <b>(b)</b> The electron beam is exposed onto the sample in an array of squares of differing size <b>(c)</b> The sample is exposed to oxygen plasma in order to etch exposed graphene <b>(d)</b> After removal of the negative electron beam resist, the patterned N-graphene squares remain on the substrate	110
<b>8.4</b>	Optical microscope images of the <b>(a)</b> patterned graphene squares which would be the target of an electrochemical microcell fabrication, <b>(b)</b> multiple devices can be fabricated on one chip and <b>(c)</b> an individual microcell device for N-graphene with the graphene sheet outlined in a white square.	112
<b>8.5</b>	A digital photograph of the electrochemical microcell set up used for testing N-graphene for the oxygen reduction reaction (ORR). The three electrode cell is composed of a homemade Ag/AgCl reference electrode, graphite or glassy carbon counter electrode and the probe is electrically connected to a N-graphene device.	113
<b>8.6</b>	Polarization curves of graphene (black) and N-graphene (red) in both N <sub>2</sub> (dashed line) and O <sub>2</sub> gas (solid line) saturated 0.5 M H <sub>2</sub> SO <sub>4</sub> electrolyte. Clear deviations from N <sub>2</sub> gas saturated experiments can be seen in the O <sub>2</sub> gas saturated curve, suggesting that the ORR is taking place. Measurements were performed at a scan rate of 10 mV/s	114
<b>8.7</b>	<b>(a)</b> C1s and <b>(b)</b> N1s spectra obtained from XPS for samples of N-graphene before and after device processing. The C1s spectra shows increased oxygen functional group concentration and sp <sup>3</sup> hybridized carbons suggesting that the sample has become very defective with much of the sp <sup>2</sup> hybridization being destroyed. The N1s spectra shows the complete removal of nitrogen from the sample.	116
<b>8.8</b>	C1s spectra obtained from XPS for <b>(a)</b> graphene and <b>(b)</b> N-graphene along the negative electron beam resist patterning process. The overall decrease in signal at step 3 is attributed to the etching of graphene material. The spectra show minimal damage for graphene, but substantial damage to the graphene lattice in N-graphene due to the increase in sp <sup>3</sup> hybridization.	117
<b>8.9</b>	N1s spectra obtained from XPS for <b>(a)</b> graphene and <b>(b)</b> N-graphene. The spectra for each shows an increase in nitrogen content after step 2 for N-graphene and the presence of nitrogen in step 3 for graphene. This indicates that the ma-N negative electron beam resist contains nitrogen. Once washed away in step 4, nitrogen is no longer present in either sample	119
<b>8.10</b>	Raman spectra of graphene and N-graphene before and after being patterned using ma-N 2403 negative electron beam resist	120
<b>8.11</b>	<b>(a)</b> Optical microscope image of the patterned sample that had undergone a NH <sub>3</sub> annealing treatment. Imperfections and defects can be seen on the gold pads. <b>(b)</b> Evolution of the Raman spectra after patterning and after undergoing a NH <sub>3</sub> annealing treatment. The 2D peak decreases in intensity with a slight increase in the D peak after the annealing treatment.	122

<b>8.12</b>	(a) C1s and (b) N1s spectra obtained from XPS on the graphene sample undergoing NH <sub>3</sub> annealing treatment after patterning. The C1s spectra shows substantial oxygen functional group content. While the N1s spectra does show nitrogen content, a spectrum taken on the same substrate but without any material shows a highly intense nitrogen peak that can be attributed to the formation of silicon nitride.	123
<b>8.13</b>	(a) Typical C1s and N1s spectra for the N-graphene sample after transferring to the pre-patterened chip. (b) Optical microscope images for the completed electrochemical microcell device demonstrating the full coverage of N-graphene throughout the substrate, open window and passivation with PMMA. (c) An individual opened window showing the underlying N-graphene and PMMA edges.	124
<b>8.14</b>	Polarization curves taken on the same device with N <sub>2</sub> and O <sub>2</sub> gas saturated 0.5 M electrolyte. No distinct difference is observed between the two electrolytes, suggesting that no ORR was taking place. Measurements were taken at a scan rate of 10 mV/s.	126
<b>8.15</b>	Optical microscope images of the damage during the electrocatalytic experiment. (a) Electrochemical microcell device with the aim to measure the electrocatalytic properties of the window in the bottom right corner by probing the nearby gold pad. Images (b) before and (c) after the electrochemical experiment of the opened window nearby the probed gold pad. Clear damage and etching can be seen to the N-graphene sheet. Images (d) before and (e) after the electrochemical experiment of the opened window far from the probed gold pad. Even more damage has occurred to the N-graphene sheet in comparison to the nearby window. Undamaged N-graphene can be seen underneath the PMMA layer.	127
<b>8.16</b>	Optical microscope image showing the damage to the PMMA layer due to boiling of the electrolyte. Bubbles and bumps can be seen along the PMMA layer within the damaged region.	129

## **Chapter 1. Introduction**

### **1.1 Motivation**

With the decrease in fossil fuel reserves and increase in total world power consumption, it is clear that we cannot depend on the combustion of fossil fuels for our increasing energy needs.<sup>1,2</sup> In recent years, global energy needs has risen more slowly. However, if the global economy continues to grow at an average 3.4 % per year and population continues as well, by 2040 energy needs will have expanded by 30%.<sup>2</sup> The primary source of this energy comes from the combustion of carbon based fuels, which will not last forever and releases a number of harmful greenhouse gases that result in anthropological climate change.<sup>2,3</sup> Emission of greenhouse gases, such as carbon dioxide, methane and nitrous oxide, have increased by 70% between 1970 and 2004. More recently, in 2011 global carbon emissions are up to 9, 449 million metric tons. Carbon dioxide is the major constituent of global greenhouse gas emission at 65%.<sup>4,5</sup>

Average global temperatures show an average increased rate of warming while extreme highs and lows are becoming more common. Changes in global temperature can disrupt ecosystems and habitats, especially if the changes are observed in a faster manner than plants and animals can adapt.<sup>5</sup> Increased tropical storm activity, higher rates of precipitation, and fluctuating frequency of droughts and river flood events have all been linked to climate change. In addition, changes to ocean temperature and acidity have all been affecting the natural habitats of plant and animal species and disrupting weather cycles. As the sea level rises, the coastline of several countries have changed and flooding along the U.S. coastline has become more frequent.<sup>5,6</sup>

To overcome these issues, an alternative must be found. According to the BP Statistical Review, the power generation due to renewable energy steadily grows every year, reaching 3.2 % of global primary energy consumption and 7.5 % of global power generation in 2016.<sup>7,8</sup> Although renewable energy still composes a modest percentage of global energy generation, it grows as new and more improved technologies are implemented.<sup>7</sup> While significant advances have been made, cost, performance and other challenges prevent consumer commercialization.<sup>9,10</sup> Fuel cells have emerged as a leading clean energy technology and with further improvement may be a viable replacement of fossil fuels.

Fuel cells electrochemically generate electricity using the chemical energy of a fuel, typically hydrogen. When hydrogen is used as the fuel source, fuel cells will generate electricity and the only byproducts are water and heat.<sup>11</sup> Due to the nature of their operation, they can be adapted to diverse use-cases.<sup>12</sup> One example is large power generation for cities replace fossil fuel power plants. Not only would this remove our dependence on a limited resource, it would reduce greenhouse gas emissions.<sup>10,13</sup> Since fuel cells operate in an analogous manner to batteries they can also be used for low power mobile devices like laptop batteries.<sup>10,12,14</sup> However, two large barriers exist preventing commercialization of fuel cell technology. First, hydrogen is currently generated using steam reformation, a fossil fuel burning process. Alternatively, hydrogen can be generated using platinum or other precious metals in electrochemical electrolyzers. Similarly, state of the art fuel cells use platinum as an electrocatalyst to generate electricity. While platinum is efficient for both generating hydrogen and in fuel cell

devices, it is expensive and non-abundant. Significant research efforts are aimed towards the development of cost effective and earth abundant catalysts.

Two dimensional (2D) materials have been shown to be catalytically active for producing hydrogen and for use in fuel cells.<sup>15,16</sup> 2D materials such as MoS<sub>2</sub> have been shown to be active for the hydrogen evolution reaction<sup>15,17,18</sup> and similarly, nitrogen doped graphene (N-graphene) for the oxygen reduction reaction<sup>19,20</sup>. Research in electrochemical catalysts often focuses on increasing surface area or elemental doping in efforts to improve catalytic activity.<sup>21-24</sup> While this approach can lead to better catalytic activity, it doesn't probe the role of charge transfer or provide insight on the true active site of the material. Developing fabrication methods and techniques to examine these properties would allow for a deeper characterization and understanding of these materials as they catalyze these electrochemical reactions.

## 1.2 Objectives of Work

When we consider layered materials in electrocatalytic research, it is typical to investigate the catalyst in ink based form, that is the solid electrocatalyst is dispersed in a solvent. While this allows for simple and consistent testing, it does not allow for a very in-depth investigation of the electrochemical properties. With a layered morphology, it can be difficult to determine how interactions between the layers can affect the electrochemical performance. Simplifying the device structure to a single layer would allow us to remove these interactions and examine the electrocatalytic properties at a more intrinsic level. The primary goal of this thesis is in the development of



electrochemical devices on single layered materials and investigating their catalytic properties.

In this thesis we are proposing the use of electron beam lithography in order to fabricate electrochemical microcells on single layer materials. The scope of this thesis includes developing the techniques to fabricate microcells, performing the electrochemical characterization and gain some insight about the active site in electrocatalytic reactions. Using electron beam lithography, we will selectively open windows on microscale devices of single layer materials. From there will characterize the material using Raman spectroscopy and X-Ray photoelectron spectroscopy (XPS). We will use electrochemical techniques, such as cyclic voltammetry, hydrodynamic voltammetry with a rotating ring-disk electrode, and electrical impedance spectroscopy, to study the electrocatalytic behavior. In parallel, we will also measure the electrical properties of the devices in hopes to correlate with the electrochemical activity. Combining the knowledge gained from the electrochemical and electrical characterization, we hope to elucidate some intrinsic behavior about the active site in MoS<sub>2</sub> and N-graphene electrocatalysis.

### **1.3 Organization of the Thesis**

Chapter 1 of the thesis discusses the motivation, scope and objectives of the project.

Chapters 2 and 3 provide background information for this thesis. Chapter 2 contains an introduction to layered materials and their properties with a focus on MoS<sub>2</sub> and graphene.

Chapter 3 gives an introduction to basic electrochemistry as well as a detailed literature review on the electrocatalytic reactions focused on in this thesis. In addition, previous work on MoS<sub>2</sub> and graphene in reference to electrocatalysis is included. Chapters 4 – 8

comprise the experimental portion of this thesis. Chapter 4 discusses the materials synthesis, experimental methods and characterization techniques used in this project. Chapter 5 covers the optimization of the fabrication process for the electrochemical microcell devices on single layer nanosheets of MoS<sub>2</sub>. Chapter 6 focuses on the electrocatalytic testing of MoS<sub>2</sub> microcells for the hydrogen evolution reaction and analysis of the results. Chapter 7 covers the nitrogen doping of graphene and graphene oxide and the process of fabricating microcell devices on nitrogen doped graphene. Chapter 8 has the electrochemical analysis of the nitrogen doped graphene and graphene oxide. Finally, to complete this thesis, Chapter 9 contains future work and conclusions.

## Chapter 2. Two Dimensional Materials

A new class of materials have emerged and demonstrated that the dimensionality of materials can affect their fundamental properties in novel and interesting ways. Two-

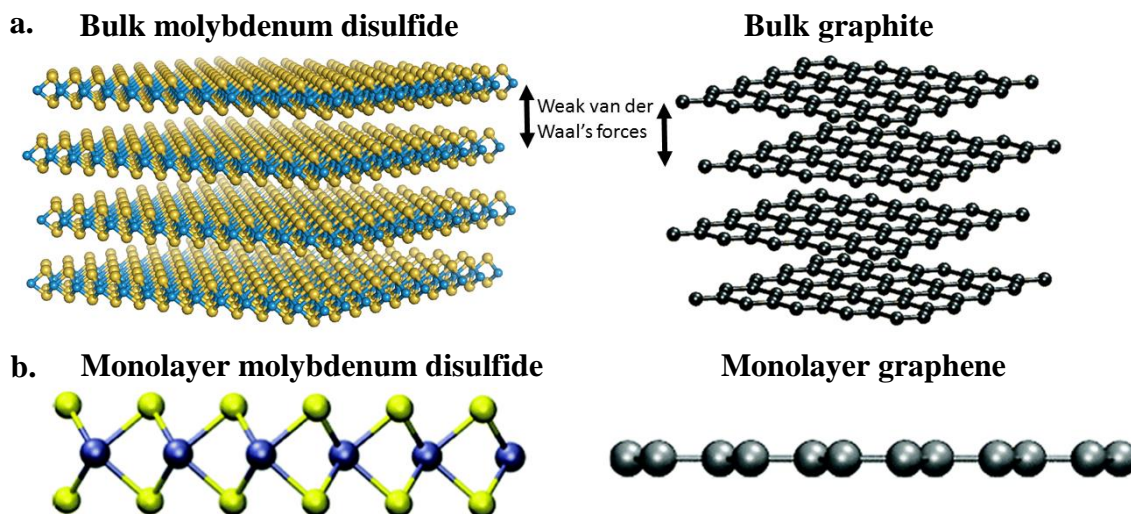


**Figure 2.1:** (a) Bulk layered materials molybdenum sulfide and graphite<sup>26</sup> and corresponding (b) single layer forms of molybdenum sulfide and graphene.<sup>26</sup> Blue, yellow and black spheres represent molybdenum, sulfur and carbon atoms, respectively

dimensional (2D) materials, such as boron nitride, molybdenum disulfide, and graphene, have a layered morphology in which layers or sheets of material are stacked on top of each other forming a three-dimensional structure of 2D overlapping sheets.<sup>25–27</sup> These sheets are connected in the vertical direction by weak intermolecular forces called van der Waal's forces as shown in Figure 2.1a, where we see bulk forms of molybdenum sulfide and graphite.<sup>26,28</sup> By taking advantage of the layered structure, we can exfoliate the bulk materials by breaking the weak van der Waal's forces by mechanical<sup>29</sup> or chemical means.<sup>30</sup> With sequential exfoliation of the layers it is possible to realize a 2D nanosheet of material that is at minimum one atom or unit cell thick. Single layers of molybdenum sulfide and graphene are shown below their bulk forms in Figure 2.1b.<sup>26</sup>

With weak van der Waal's forces in the vertical direction and strong covalent bonds in the lateral direction, it is possible to consider layered materials as single two dimensional sheets or as closer to bulk material with overlapping sheets.<sup>31</sup> While graphene has become the classic example of 2D materials, the field has grown to encompass subclasses such as hexagonal boron nitride<sup>32,33</sup>, transition metal dichalcogenides<sup>25,34</sup>, transition metal oxides<sup>35,36</sup>, topological insulators<sup>37</sup>, silicene<sup>38</sup>, black phosphorous<sup>39</sup> and organic-inorganic hybrid perovskites<sup>40,41</sup>. Each material or class of materials have a different set of interesting properties, especially when in single layer form where quantum confinement effects are possible.<sup>25,42</sup> This allows us to tune the properties of the material to fit various different applications such as electrocatalysis<sup>15,43-45</sup>, transistors<sup>46-48</sup>, photodetectors<sup>49</sup>, supercapacitors<sup>50</sup> and many more.

## 2.1 Graphene & Graphene Oxide

The distinct change in fundamental properties when we consider 2D materials against their bulk forms can be exemplified with graphene. In its bulk form, graphene is graphite with stacks of graphene sheets on top of each other. Graphene is a single sheet of carbon one atom thick in the lateral dimension, in which the carbon atoms are highly saturated and bound in a hexagonal lattice structure with  $sp^2$  orbital hybridization with no dangling bonds.<sup>51,52</sup> Due to its unique structure it exhibits remarkable qualities that has made it the focus of much research in past years. Graphene is a semi-metal with a band gap of zero, making it an excellent conductor of electricity with a sheet resistance  $30 \Omega/\text{sq}$  and electron mobility greater than  $3000 \text{ cm}^2 \text{ V}^{-1} \text{ s}^{-1}$ .<sup>53-55</sup> The relationship between the quality of graphene and cost has been a major barrier to commercialization of graphene. In response to this, different synthesis methods have been developed to reduce costs. As

shown in Figure 2.2<sup>56</sup>, at low cost the graphene quality is also low; meanwhile the highest quality graphene is also the most expensive. This tradeoff between cost and quality must be optimized when considering graphene applications. An alternative to graphene that has

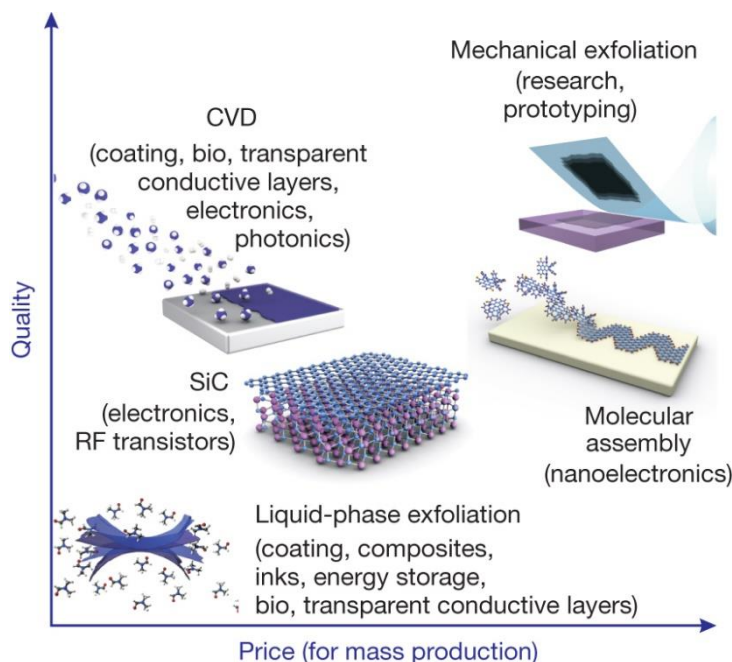


**Figure 2.2:** The different methods for graphene production of varying quality and their corresponding cost. In parentheses, the main applications of each production method are listed.<sup>56</sup>

been developed is graphene oxide. Graphene oxide (GO) is analogous to graphene in that it still contains a sheet of carbon atoms bonded in a hexagonal pattern, however it has several oxygen functional groups formed during the solution based synthesis and exfoliation as shown in Figure 2.3.<sup>57</sup> These groups disrupt the graphene sheet and are attached throughout the GO sheet.<sup>58</sup> These carboxyl<sup>59–61</sup>, carbonyl<sup>59,60,62</sup>, hydroxyl<sup>59,60,62,63</sup>, and epoxide<sup>59,60,62,64,65</sup> functional groups help stabilize the nanosheets in solution<sup>64,66–68</sup> and make them hydrophilic<sup>68–70</sup>. However, they limit the graphene character, causing the atoms in GO to be in a hybrid state with a blend of the more conducting and graphene like  $sp^2$  hybridized atoms and the non-conducting  $sp^3$

hybridized atoms. This lowers the overall conductivity of GO, but can be modulated by reduction chemistry.<sup>71–73</sup> The GO sheets can also be easily suspended in solution so are readily available for several solution based processing such as spin coating<sup>74–76</sup> or vacuum filtration<sup>67,77,78</sup> to make thin films. This is advantageous for commercialization on a wider scale with efforts started for use in 3D printers.<sup>79,80</sup>

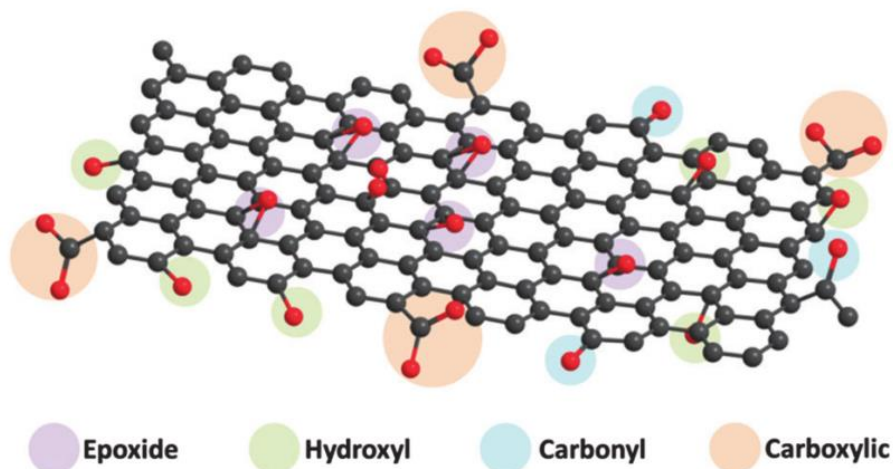


**Figure 2.3:** Nanosheets of graphene oxide (GO) are composed of carbon sheets that have been functionalized by several different functional groups such as epoxide, hydroxyl, carbonyl and carboxylic groups.<sup>57</sup>

### 2.1.1 Reduction of Graphene Oxide

In efforts to remove functional groups we can reduce the GO sheet, making reduced graphene oxide (rGO)<sup>58,74,81–83</sup> which will have higher graphene character and higher conductivity.<sup>77</sup> Carefully tuning the ratio between  $sp^2$  and  $sp^3$  hybridization in a sheet of rGO allows control over whether the rGO is insulating, semiconducting or even graphene-like and semi-metallic.<sup>77,84,85</sup> There are various methods to reducing GO, but the most common methods are by thermal or chemical means.

Thermal reduction uses high temperature annealing in an inert or a reducing atmosphere such as argon or hydrogen in argon, respectively. This drives off oxygen functional

groups and some  $sp^2$  hybridization is restored to the rGO sheet improving the conductivity of rGO thin films up to  $1000 \text{ S m}^{-1}$  after reduction at  $2000^\circ\text{C}$  and even greater for rGO papers.<sup>72,74,85,86</sup> As these oxygen functional groups are reduced from the sheet, some CO and  $\text{CO}_2$  is formed with carbon atoms being released from the rGO lattice, introducing defects and holes within the sheet. In addition, it has been shown that when annealing at high temperature, carbonyl and ether groups are stabilized and challenging to remove. This was demonstrated using molecular dynamics simulations as shown in Figure 2.4a in the initial GO sheet and the thermally annealed rGO sheet in

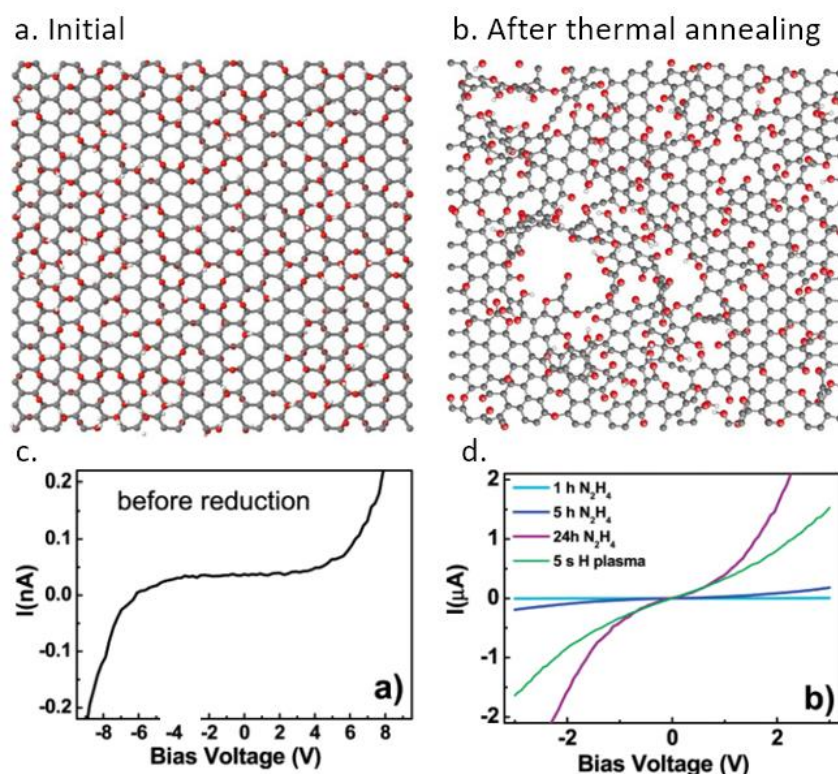


**Figure 2.4:** (a) Initial sheet of GO before any reduction. (b) High temperature annealing can reduce GO, however it also stabilizes some functional groups and creates holes and defects.<sup>87</sup> Electrical characteristics (c) before reduction and (d) after varying amounts of time being exposed to hydrazine and hydrogen plasma<sup>82</sup>

Figure 2.4b.<sup>72,87</sup> Stabilized functional groups and defects make it difficult to fully overcome the non-conducting nature of GO.

Chemical reduction of GO uses chemical reducing agents such as hydrazine monohydrate or sodium borohydride. While the chemical mechanism is not always well known, reduction is typically noted by the production of a black powder precipitating out of the GO solution upon addition and reaction with the reducing agent.<sup>88</sup> Sodium borohydride, a common reducing agent used in synthetic chemistry, readily reduces carbonyl groups.<sup>89</sup> When a thin film is dipped into a solution of sodium borohydride, the conductivity of the resultant rGO film can be improved to  $45 \text{ S m}^{-1}$ .<sup>71</sup> Hydrazine monohydrate, a highly toxic and dangerous antioxidant, is known to reduce carbonyl groups to form hydrazone molecules.<sup>89</sup> Due to this, nitrogen is often observed in the rGO sheet after using hydrazine monohydrate as a reduction treatment. I-V characteristics are shown in Figure 2.4c,d<sup>82</sup> for GO and hydrazine treated GO monolayers with variable time, respectively. In GO monolayers, the conductivity was found to be  $1\text{-}5 \times 10^{-3} \text{ S/cm}$ . After reduction, the rGO showed conductivity values of  $0.05\text{-}2 \text{ S/cm}$ , an increase of three orders of magnitude.<sup>82</sup> The reduction mechanism of hydrazine on GO is not well characterized. The first mechanism proposed was of a direct nucleophilic attack by hydrazine on an epoxide group on the basal plane of a GO sheet. An aminoaziridine intermediate is formed which will further reach to remove a diimide group, forming a double bond on a GO sheet.<sup>90</sup> Further study of the mechanism used solid state nuclear magnetic resonance spectroscopy and X-ray photoelectron spectroscopy to track how  $^{13}\text{C}$  and  $^{15}\text{N}$  isotopes reacted after hydrazine treatment. They found that five-membered rings of pyrazole were formed at the edges of the graphene sheet.<sup>91</sup> Using hydrazine treatment, conductivities greater than  $9000 \text{ S m}^{-1}$  have been reported.<sup>92</sup> Many stronger reducing agents have used



to synthesize rGO, such as hydrohalic acids like HI, HBr, and HCl and stronger hydrides like lithium aluminum hydride.

Nontraditional reduction methods beyond thermal or chemicals means are also possible. After application of 10 - 15 V in an electrochemical cell, GO can be delaminated and reduced to form rGO thin films in a few minutes. During the electrochemical reduction, charge is transferred to the GO sheet and reacts to form hydroxide ions that are released into solution. This method yielded rGO thin films with conductivities reaching  $2.0 \times 10^5 \text{ S m}^{-1}$ .<sup>93</sup> Other alternative techniques use Joule heating<sup>94</sup>, photoreduction<sup>95</sup> and even microorganisms<sup>96</sup> to remove oxygen functional groups from GO sheets.

### 2.1.2 Nitrogen doping of Graphene & Graphene Oxide

Nitrogen doping has been found to modulate the electronic, hardness and chemical properties of graphitic carbon materials.<sup>97–103</sup> In graphene, it is well known to influence the electronic structure of graphene in order to tailor the properties for different applications.<sup>104</sup> While other heteroatoms, such as boron or sulfur<sup>103</sup>, have been used nitrogen is of particular interest due to its effect on the electrocatalytic properties.<sup>102,105</sup> Nitrogen typically undergoes substitutional doping as it incorporates into the graphene

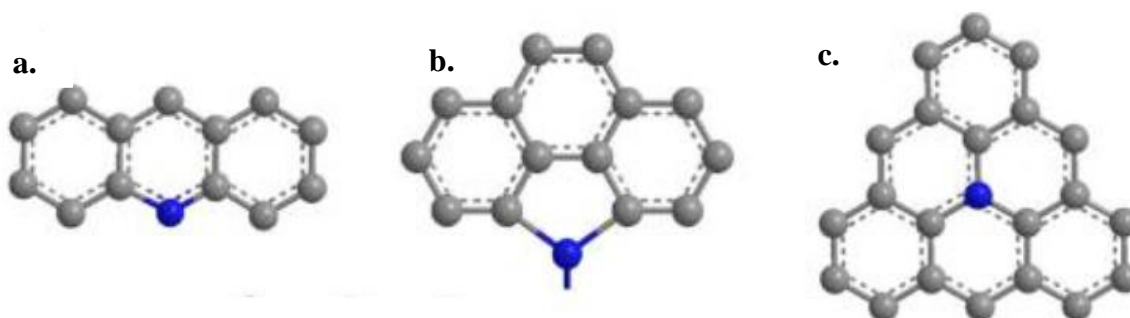


**Figure 2.5:** Nitrogen can incorporate into graphene material in three main bonding configurations: (a) pyridinic, (b) pyrrolic and (c) graphitic.<sup>16</sup>

sheet. It can take the form of a pyridinic, pyrrolic and graphitic nitrogen bonding configuration, as shown in Figure 2.5a,b,c<sup>16</sup> respectively. Pyridinic and pyrrolic nitrogen bonding configurations are generally found at the edge or defect sites, while graphitic configurations occur when nitrogen replaces carbon within the basal plane of graphene.<sup>102,106,107</sup> Nitrogen acts as a donor of electrons when doped into graphene, shifting the typical ambipolar behavior of graphene to n-type, which is useful for applications in field effect transistors as shown in Figure 2.6a.<sup>101,104</sup> Compared to pristine graphene, the nitrogen doped graphene has much higher on/off ratios at positive gate voltages as expected for n-type materials, although it has lower conductivity. When nitrogen doped graphene is grown using pyridine<sup>101</sup> or  $\text{NH}_3$  and  $\text{CH}_4$  as precursors, ripples are formed in the graphene sheets leading to an increase in defects. These defects can act as scattering centers causing a decrease in conductivity and carrier mobility by a few orders of magnitude.<sup>101</sup> Investigations into how the nitrogen doping configuration can play a role in the n-type behavior found that as the concentration pyridinic and pyrrolic nitrogen increases so does the n-type characteristics.<sup>108</sup>

Incorporation of nitrogen into GO, has also been studied as a means to improve the conductivity of GO/rGO. Annealing as-synthesized GO in  $\text{NH}_3$  gas at high temperatures was found to dope the GO with nitrogen and reduce the GO simultaneously. The reduction was found to have more efficient oxygen removal when compared to annealing in  $\text{H}_2$  at the same temperature. Electrical measurements showed a clear increase in conductivity and shift to n-type behavior as shown in the current-gate voltage curves in Figure 2.6b.<sup>102,109</sup> Devices tested in air show p-type behavior due to physisorbed oxygen.

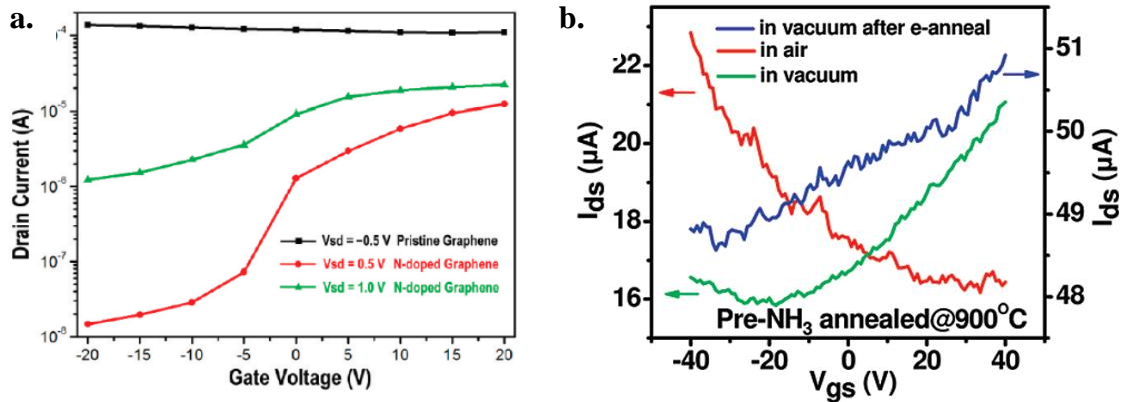


**Figure 2.6:** (a) Transfer characteristics of pristine graphene at a drain-source voltage ( $V_{sd}$ ) of -0.5 V in comparison to nitrogen doped graphene at  $V_{sd}$  of 0.5 V and 1.0 V. N-graphene exhibits clear n-type behavior<sup>104</sup> (b) Current-gate voltage curves of a device containing GO annealed in  $NH_3$  at 900 °C. The was measured in air (red), vacuum (green) and in vacuum after electrical annealing (blue) to remove physisorbed oxygen<sup>109</sup>

To prevent this behavior, the devices were tested in vacuum and electrically annealed and show clear n-type behavior.

## 2.2 Transition Metal Dichalcogenides

Transition metal dichalcogenides (TMDs) are a class of 2D materials with a slightly larger theoretical thickness at  $6.5 \text{ \AA}$ <sup>48</sup> for molybdenum disulfide in comparison to graphene at  $3.35 \text{ \AA}$ <sup>110</sup> but also contain van der Waal's bonds in the vertical direction and can thus be exfoliated into 2D sheets. Instead of a single atomic sheet, TMDs take the form of  $MX_2$  where M is a transition metal from Group IVB, VB or VIB and X is a chalcogen atom such as sulfur, selenium or tellurium. The metal atoms form the center of the molecule with the chalcogen atoms on either side to form the 2D layer as shown in Figure 2.7.<sup>111</sup> Within the family of TMDs, there exist 2D materials with differing electronic properties allowing for use as semiconductors, super conductors, semi-metals, topological insulators.<sup>25,26</sup> By tailoring the properties, we can use TMDs, such as  $MoS_2$ ,  $MoSe_2$ ,  $WS_2$  and  $WSe_2$ , in various applications such as electrocatalysis<sup>112</sup>, field effect

transistors<sup>46</sup>, supercapacitors<sup>113</sup> and batteries.<sup>114</sup>

## 2.3 Molybdenum disulfide (MoS<sub>2</sub>)

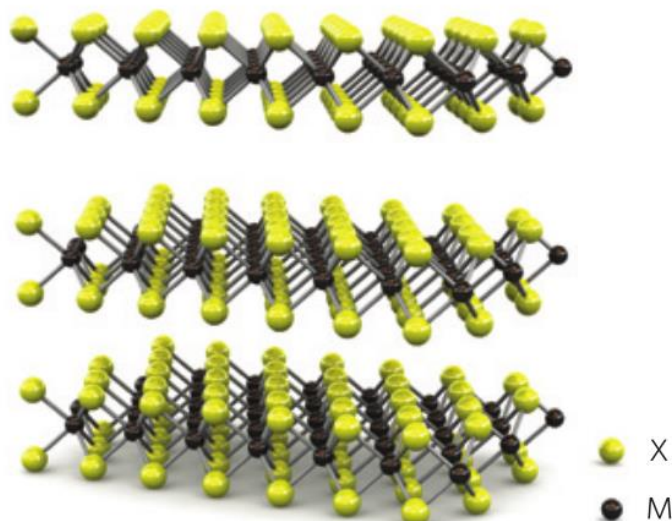


**Figure 2.7:** Representative structure of a transition metal dichalcogenides where M is a transition metal and X is a chalcogen atom.<sup>111</sup>

Aside from graphene, molybdenum disulfide (MoS<sub>2</sub>) is the next most studied 2D material. A member of the TMDs, MoS<sub>2</sub> is of interest due to its unique optoelectronic, electrocatalytic, mechanical and chemical properties; making MoS<sub>2</sub> attractive for specific applications in batteries<sup>115</sup>, photodetectors<sup>116</sup>, photocatalysis<sup>117,118</sup>, field-effect transistors<sup>48,119</sup> and solar cells<sup>120–122</sup>. Structurally, MoS<sub>2</sub> is composed of a row of molybdenum atoms that have been sandwiched by sulfur atoms on the top and bottom. As adjacent layers are stacked on top, no molybdenum atoms are found in between the layers as shown schematically in Figure 2.7<sup>111</sup> where M will be Mo and X will be S. Similar to graphene, distinct differences exist between the bulk and monolayer form of MoS<sub>2</sub>. Bulk MoS<sub>2</sub> has an indirect band gap of 1.29 eV. However, as you remove layers and exfoliate the material to single layer, the band gap transitions to direct. Theoretical energy-k band diagrams of bulk, quadrilayer, bilayer and monolayer MoS<sub>2</sub> are shown in Figure 2.8a-d.<sup>42</sup> The valence and conduction band edges can be seen in blue and red

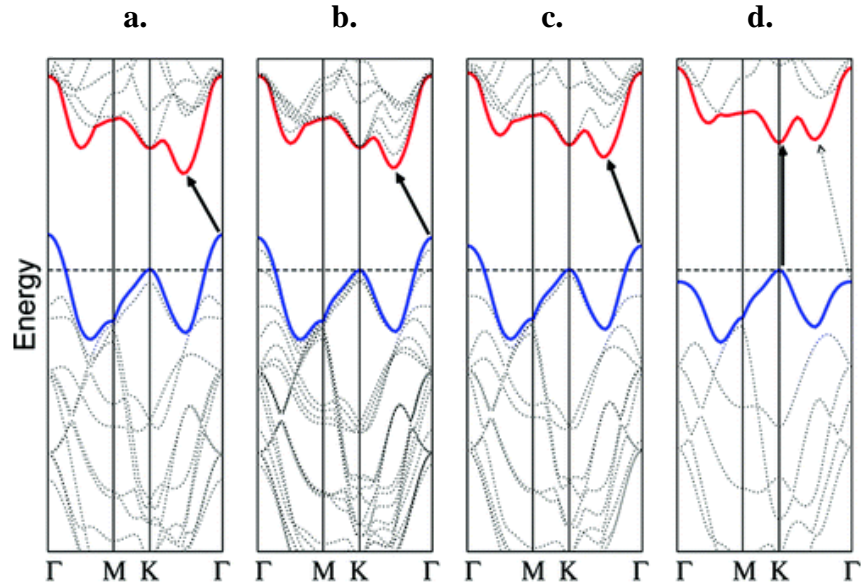


**Figure 2.8:** Theoretically calculated band structures of (a) bulk MoS<sub>2</sub>, (b) quadrilayer MoS<sub>2</sub>, (c) bilayer MoS<sub>2</sub> and (d) monolayer MoS<sub>2</sub>. Solid arrows indicate the lowest energy transition available within the band structure.<sup>42</sup>

respectively, while the dashed horizontal line shows the valence band edge maximum at the K point. As thickness decreases the direct transition energy at the Brillouin zone K point does not change much, while the indirect transition energy at the  $\Gamma$  point increases until it exceeds the direct transition energy in monolayer MoS<sub>2</sub>. This changes the material into a direct band gap semiconductor in monolayer form and is due to quantum confinement effects.<sup>25,42</sup> This transition to a direct band gap can be readily observed by an enhancement in photoluminescence in monolayer samples of MoS<sub>2</sub>.<sup>42,123</sup>

### 2.3.1 Phase Transition in MoS<sub>2</sub>

MoS<sub>2</sub> is naturally stable in the semiconducting 2H phase, but can also exist in two other polymorphs, the 1T or 3R phase. In monolayer sheets of MoS<sub>2</sub>, only the 1T and 2H phases are observed. In each phase, one molybdenum atom is bonded to 6 other sulfur atoms. The 2H phase exhibits ABA stacking with a lateral offset and trigonal prismatic crystal symmetry, with sulfur atoms positioned vertically in line with their counterparts.

The 1T phase has a AbC stacking sequence and octahedral crystal symmetry, meaning one plane of sulfur atoms has been rotated  $60^\circ$  so that if viewing the basal plane all 6

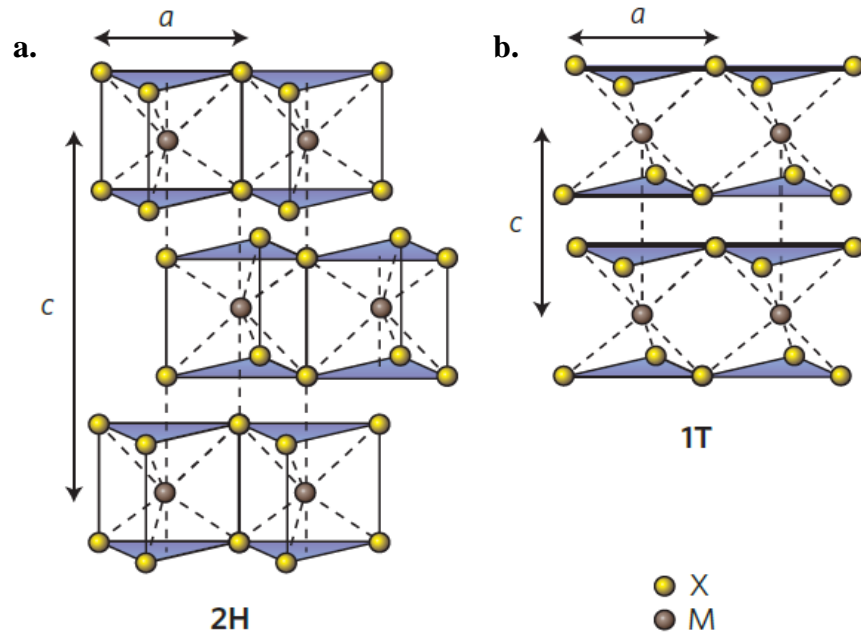


**Figure 2.9:** Crystal structure of (a) 2H and (b) 1T polymorphs for TMDs<sup>111</sup>

sulfur atoms are visible.<sup>111,124</sup> In MoS<sub>2</sub> and other TMDs, the d orbital of the metal plays a key role in the electronic structure. The p orbitals of the chalcogen atoms are found at lower energy, so do not affect the electronic structure as much. In the 2H phase, the d orbital is completely filled resulting into a split into three degenerate states  $d_{z^2}$ ,  $d_{x^2-y^2}$ ,  $xy$  and  $d_{xy,yz}$  and an energy gap is formed between  $d_{z^2}$  and  $d_{x^2-y^2}$  of  $\sim 1$  eV. In contrast to this, the 1T phase has a partially filled d orbital that will degenerate into two states:  $d_{x^2-y^2,z^2}(e_g)$  and  $d_{xy,yz,zx}(t_{2g})$ .<sup>25,27,124</sup> Using alkaline organometallic chemistry, we can convert between the semiconducting 2H phase to the metallic 1T phase. Since the 1T phase is metastable, we can revert back to the 2H phase with mild annealing. In our group we have taken advantage of this phase transition to improve the performance of field effect transistors<sup>47</sup>, electrocatalytic activity<sup>17,44</sup> and as supercapacitors<sup>50</sup>.

## 2.4 Synthesis of Two Dimensional Materials

### 2.4.1 Top-down approach

There are two main approaches to synthesis of 2D materials: top-down and bottom-up. In the top-down approach, synthesis is focused on exfoliation of a bulk material. Typically, high quality monolayers are made using the classic top-down approach of mechanical exfoliation<sup>58,125,126</sup>, which is time consuming with low yield.<sup>127,128</sup> However, it is still one

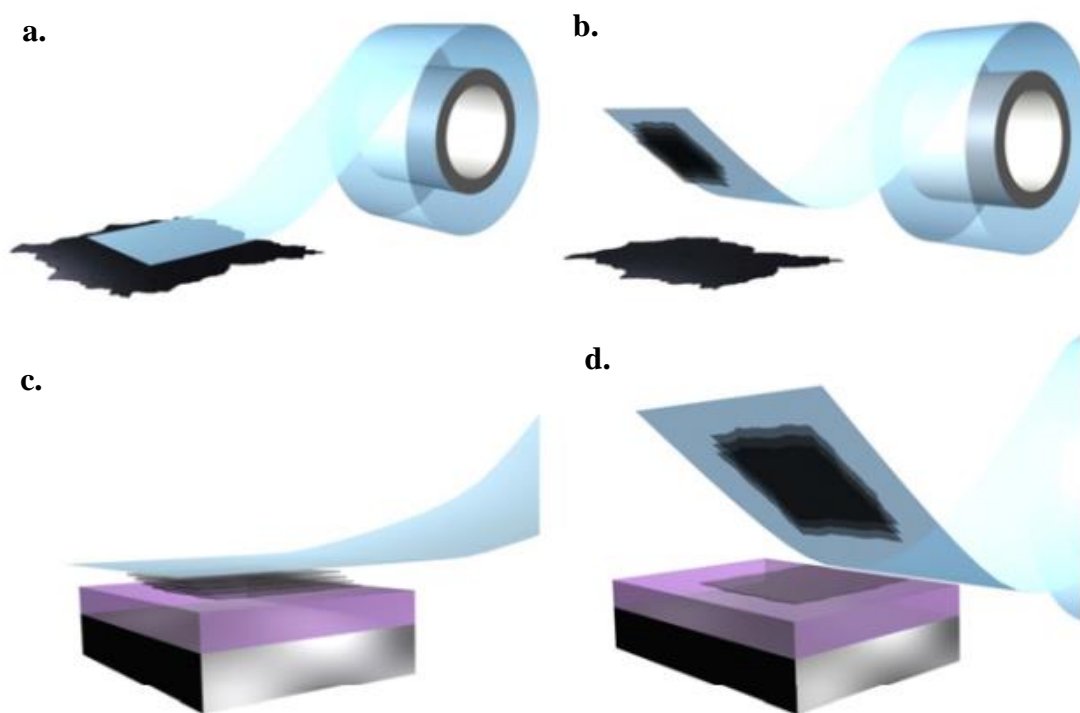


**Figure 2.10:** Mechanical exfoliation of graphite to yield graphene. **(a)** Adhesive tape is applied to a sample of HOPG crystal. **(b)** As the tape is pulled off of the HOPG crystal a few layers are mechanically exfoliated as they stick to the tape. **(c)** The tape with a few layers of graphene is pressed onto a target substrate **(d)** and as the tape is pulled off of the target substrate, the bottom layer remains on the substrate to yield a clean monolayer.<sup>129</sup>

done at scalable quantities.<sup>133</sup> Unfortunately, the sonication can render individual flakes into nanoscale size, making them unsuitable for electronic devices.

As an alternative to using shearing forces, we can also use chemical means to exfoliate layered materials. In the case of graphene, we can oxidize bulk graphite crystals into graphite oxide then exfoliate the dispersion into GO. We can synthesize GO using the Brodie, Staudenmaier method, Hummer's method or the modified versions of each.<sup>26,58,134,135</sup> In our group we use the modified Hummer's method. In the modified Hummer's method, bulk graphite is chemically oxidized in an acidic bath with concentrated sulfuric acid, potassium permanganate and sodium nitrate. Potassium permanganate is added slowly as the black reaction solution turns dark green. Once fully incorporated, the solution is cooled in an ice bath for five days to allow for slow and thorough oxidation of the graphite. As the oxidation completes, the solution becomes more viscous and exhibits a dark brown-purple color. Hydrogen peroxide is then added as a reducing agent in order to oxidize remaining reactants and stop the reaction. Dilute hydrochloric acid is also added to dissolve and reduce any metal contaminants into ions so they can be washed away. Immediately upon addition of these reagents, the solution turns a dull yellow color and effervesces as oxygen gas is formed. The solution is washed and purified by dialysis to remove remaining acid and reagents. At this point, the dispersion is termed graphite oxide and should be dark brown. Upon mild sonication, the graphite oxide is exfoliated into GO.<sup>134</sup> A simple schematic from graphite to the finished GO sheets is shown in Figure 2.11a.<sup>72</sup> The exfoliated nanosheets of GO are dispersed into solution, which allows for several solution based processing such as spin coating<sup>74-76</sup> or vacuum filtration<sup>67,77,78</sup> to make thin films.



In the case of  $\text{MoS}_2$  and other TMDs, we can use organometallic reagents to exfoliate the bulk crystals. The exfoliated nanosheets can be dispersed into liquid as shown in Figure 2.11b.<sup>25</sup> A strong reducing agent such as pyrophoric n-butyllithium is used to intercalate lithium ions into the van der Waal's gap between the layers.<sup>136</sup> Due to the pyrophoric nature of n-butyllithium, extra care is taken to dry all glassware and run the reaction in an inert atmosphere, such as argon. A schlenk line is recommended, but not required. An aliquot of n-butyllithium in hexane is added to  $\text{MoS}_2$  powder in the ratio of 3:1 by mass. The reaction takes place in a round bottom flask connected to a Liebig condenser and is heated into refluxing conditions. As the reaction progresses, the solution becomes a dark black color. During the reduction reaction, lithium ions diffuse through the  $\text{MoS}_2$  crystal and intercalating between the layers. After 48 hours under reflux, the lithium intercalated powder,  $\text{Li}_x\text{MoS}_2$ , is collected and washed with hexane to remove excess butyllithium and other organic byproducts. The lithium intercalated powder is then dispersed in water.

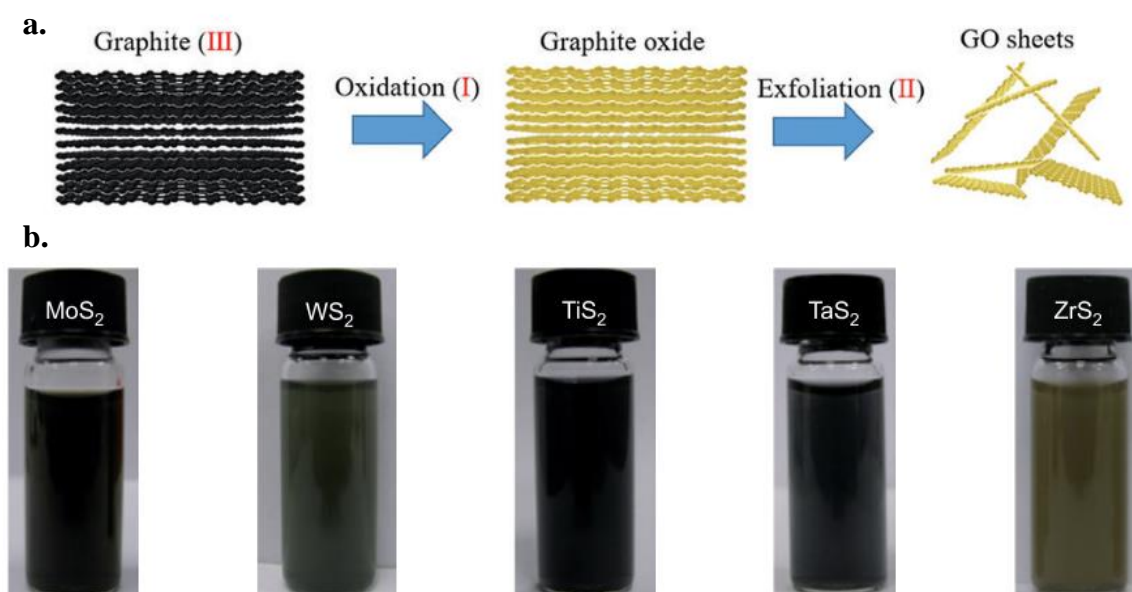


**Figure 2.11:** (a) Schematic of the synthesis of GO showing oxidation and exfoliation to yield GO sheets.<sup>72</sup> (b) Dispersions of transition metal dichalcogenides nanosheets in water synthesized using organometallic chemistry.<sup>25</sup>

The generation of hydrogen gas during this process exfoliates the layers, breaking the weak van der Waals forces. Once dispersed, the solution is washed and centrifuged to obtain MoS<sub>2</sub> nanosheets dispersed into aqueous solution. During the lithium intercalation, there is an electron transfer from the reducing agent, in this case n-butyllithium, that will distort the crystal structure of MoS<sub>2</sub>. This causes the transformation from the trigonal prismatic 2H phase to the octahedral 1T phase.<sup>25,123</sup> Similar to GO, the solution dispersed MoS<sub>2</sub> can be used in standard solution processing techniques.<sup>15,123,137,138</sup>

## 2.4.2 Bottom-up approach

When using the bottom-up approach to 2D material synthesis, the focus is on growing few layer to monolayers directly onto a substrate. The most common bottom-up approach is chemical vapor deposition (CVD). It has been demonstrated as a viable option for growing monolayers of graphene<sup>139,140</sup>, MoS<sub>2</sub><sup>141,142</sup> and other TMDs<sup>143</sup>. Although the lateral dimensions started out small, research has been heavily focused in developing methodologies to grow larger areas. In recent years, large area graphene has been grown using scalable methods.<sup>53,144</sup> In general, CVD synthesis of 2D materials follows the same pattern. In a tube furnace with an inert atmosphere, gaseous precursors are flowed in or solid precursors are vaporized. As the furnace is brought to high temperature, 650 °C – 1000 °C, the vapors present will react to hopefully form the desired product and sublime onto an appropriate substrate.<sup>141,143</sup> In the case of graphene, a polycrystalline nickel catalyst was first used to synthesize graphene using CVD, however the nickel limited the graphene grain size.<sup>139</sup> In order to realize large area graphene by CVD, copper foil was found to be a good catalytic substrate allowing for a self-limiting growth step to avoid multiple layer growth.<sup>140</sup> For TMDs, the transition metal oxide and sulfur are used as

solid precursors. For example, molybdenum trioxide and sulfur are used to grow MoS<sub>2</sub> onto silicon oxide or sapphire substrates. As the furnace is heated to high temperature, the molybdenum trioxide and sulfur will vaporize and react and finally sublime as MoS<sub>2</sub> on the substrate. While the exact mechanism is not well known, recent work has shown that modulating the vapor phase concentration<sup>145</sup> and sublimation of side products can obstruct MoS<sub>2</sub> formation.<sup>146</sup>

## 2.5 Characterization

When studying 2D materials, it is important to carefully characterize the sample using a standard set of techniques. In this work the primary methods of characterization are Raman spectroscopy, X-ray photoelectron spectroscopy, and electrochemical characterization which will be described in Chapter 3. Other techniques used were atomic force microscopy, scanning electron microscopy and scanning transmission electron microscopy (STEM).

### 2.5.1 Raman Spectroscopy in Graphene & Graphene Oxide

Raman spectroscopy uses monochromatic light to induce Raman scattering caused by certain vibrational modes found in Raman active materials.<sup>147,148</sup> In carbon materials, it is an integral tool for characterization. It provides a non-destructive method to quickly study your sample in terms of defects, structure and electronic quality.<sup>149</sup> Figure 2.12a<sup>150</sup> shows the Raman spectra for graphene, GO and other graphene related materials. The signature G band, which is seen in all graphite based samples, can be found at ~1582 cm<sup>-1</sup>. This band is associated with the in plane E<sub>2g</sub> mode, which can be seen in Figure 2.12b<sup>149</sup>. The 2D band is a characteristic of crystalline monolayer graphene and can be

found at  $\sim 2700\text{ cm}^{-1}$ . In high quality graphene, the 2D band will be two to three times higher than the G band and perfectly symmetrical. The shape of the 2D band can also be used to identify monolayer graphene. Using a Lorentz fit to the 2D peak, full-width at half-maximums (FWHMs) of  $\sim 30\text{ cm}^{-1}$  are typically seen for monolayer graphene. When more layers are added, the 2D peak will broaden. The D band corresponds to the

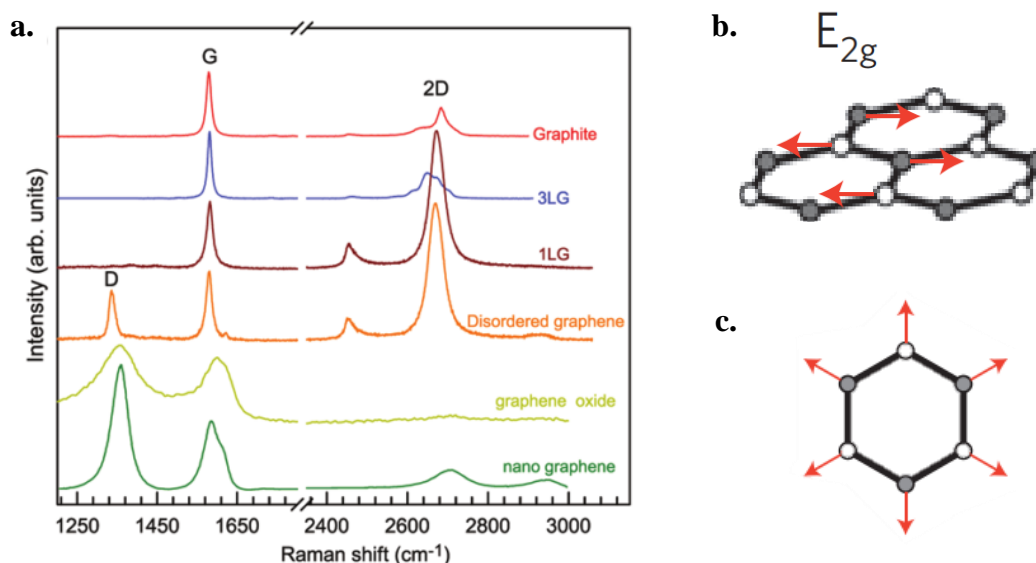


**Figure 2.12:** (a) Typical Raman spectra of graphite, monolayer graphene (1LG), three layer graphene (3LG), disordered graphene, graphene oxide and nanographene.<sup>150</sup> (b) Molecular schematic showing the  $E_{2g}$  vibrational mode in graphene.<sup>149</sup> (c) The breathing mode found in graphene.<sup>149</sup>

breathing mode of a six-carbon ring, as shown in Figure 2.12c<sup>149</sup>, and can be found at  $\sim 1350\text{ cm}^{-1}$ . In pristine monolayer graphene, the D band is not present as it is activated by disorder in the lattice and defects which induce electron scattering. As defects are introduced or created, the intensity of the D band ( $I_D$ ) increases. The 2D band is an overtone of the D band and will be present in defect-free graphene due to resonance scattering.<sup>150,151</sup> In pristine graphene the intensity of the 2D band ( $I_{2D}$ ) will always be greater than the intensity of the G band ( $I_G$ ). As you increase the layers of graphene, the 2D band is quenched until you finally reach the bulk Raman spectra of graphite.<sup>149,150</sup>

Compared to graphene, GO is missing the distinct 2D peak and will exhibit very large and broad D and G bands. This corresponds to a high degree of disorder and high concentration of defects, which is expected due to the harsh conditions resulting from the oxidation taking place during GO synthesis. After reduction, we are looking to restore the high conductivity and  $sp^2$  hybridization. One way to study this is to examine the defects in rGO. By examining the ratio between the intensities of the D and G band and from empirical data, we can calculate the distance between defects,  $L_D$  (1)<sup>149</sup>:

$$L_D^2 (nm)^2 = (1.8 \pm 0.5 \times 10^{-9} \times \lambda^4 \times \left(\frac{I_D}{I_G}\right)^{-1} \quad (2.1)$$

where  $\lambda$  is the wavelength of light used in the Raman laser. When it is relatively large ( $> 10$  nm), we can also estimate the density of defects,  $n_D$  (2)<sup>150,152</sup>:

$$n_D (cm^{-2}) = \frac{(1.8 \pm 0.5) \times 10^{22}}{\lambda^4} \times \left(\frac{I_D}{I_G}\right) \quad (2.2)$$

In addition, we can estimate the size of the crystalline domains,  $L_a$  (3) :

$$L_a(nm) = (2.4 \times 10^{-10} \times \lambda^4 \times \left(\frac{I_D}{I_G}\right)^{-1} \quad (2.3)$$

## 2.5.2 Raman spectroscopy in MoS<sub>2</sub>

Raman spectroscopy is a strong tool for characterizing MoS<sub>2</sub> and other TMDs. It can be used to distinguish between the 2H and 1T phases and determine the thickness of flakes. There are two strong vibrational modes that are Raman active in MoS<sub>2</sub>. These are found at  $384 \text{ cm}^{-1}$  and  $404 \text{ cm}^{-1}$  and correspond to the in plane  $E_{2g}^1$  mode and out of plane  $A_{1g}$  mode. Identification between the 2H and 1T phase can be found using Raman spectroscopy as seen in Figure 2.13a.<sup>123</sup> Spectra for pristine bulk and a mechanically exfoliated monolayer show distinct 2H phase behavior with strong  $E_{2g}^1$  and  $A_{1g}$ . The 1T

phase can be seen in the as-deposited sample where three distinct peaks can be observed that do not appear in the 2H phase at  $\sim 160\text{ cm}^{-1}$ ,  $230\text{ cm}^{-1}$  and  $330\text{ cm}^{-1}$  which correspond to the  $J_1$ ,  $J_2$ , and  $J_3$  vibrational modes. As you anneal the sample to higher and higher temperature these modes are quenched as the metastable 1T phase is finally relaxed into the 2H phase at  $300\text{ }^\circ\text{C}$ .<sup>25,123</sup>

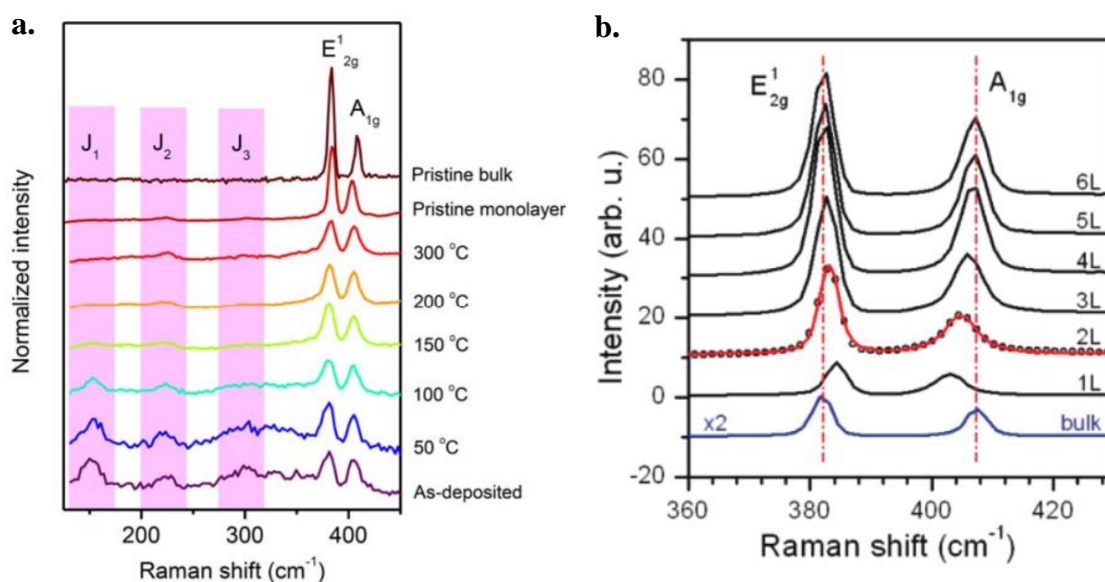


**Figure 2.13:** (a) Evolution of Raman spectra of as-deposited 1T MoS<sub>2</sub> to 2H MoS<sub>2</sub> as annealing temperature increases. Pristine bulk and monolayer MoS<sub>2</sub> are included as a reference. Characteristic peaks for 2H and 1T phase MoS<sub>2</sub> can be seen.<sup>123</sup> (b) Raman spectra for varying layers of MoS<sub>2</sub>. The separation between the two main vibrational modes of MoS<sub>2</sub>,  $E_{2g}^1$  and  $A_{1g}$ , decreases with the number of layers<sup>153</sup>

The separation between the two main vibrational modes,  $E_{2g}^1$  and  $A_{1g}$ , has been shown to correlate to the thickness of the MoS<sub>2</sub> flakes. This can be used to identify the presence of monolayers in mechanically exfoliated samples or samples grown by CVD. As you increase in layers, interlayer coupling begins to affect the intensity of the vibrations for the  $A_{1g}$  mode causing a blue shift to higher wavenumbers. The  $E_{2g}^1$  mode experiences a red shift to lower wave numbers which has been attributed to Coulombic interlayer

interactions. This can be seen in Figure 2.13b where the  $E_{2g}^1$  and  $A_{1g}$  separation increases as the number of layers increases.<sup>153</sup>

In a Raman spectroscopy instrument, we can also perform photoluminescence (PL) spectroscopy. PL spectroscopy uses the same monochromatic light as in Raman spectroscopy, but can probe electronic transitions due to the presence of a band gap.

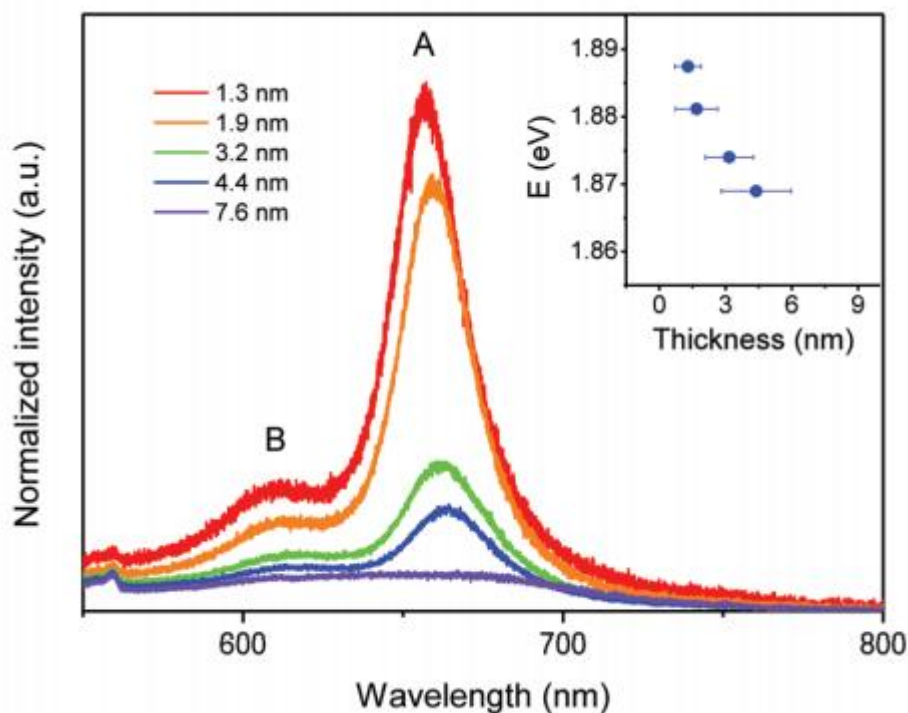


**Figure 2.14:** Increase in PL intensity as the thickness of the MoS<sub>2</sub> layer decreases down to a monolayer<sup>123</sup>

Electrons are excited to the conduction band by the laser across the band gap and eventually will relax back into the valence band. During the relaxation process, photons are emitted with energy near the band gap energy. These photons are collected as the PL signal. This is particularly useful when determining single layer samples of MoS<sub>2</sub>. As successive layers are exfoliated to get thinner and thinner samples, the PL intensity increases as MoS<sub>2</sub> shifts to a direct band gap semiconductor. This can be seen in Figure

2.14 for solution processed thin films of MoS<sub>2</sub>.<sup>123</sup> The strong PL peak is observed at 1.8 – 1.9 eV, corresponding to the band gap of monolayer MoS<sub>2</sub>, which can be seen in the inset of Figure 2.14.

### 2.5.3 X-Ray Photoelectron Spectroscopy (XPS)

X-Ray photoelectron spectroscopy (XPS) is a quantitative technique that can be used to determine the atomic composition as well as the oxidation state of a sample.<sup>147</sup> In graphene and GO, XPS allows us to scan the C1s spectra. It can be used to find the concentration of sp<sup>2</sup> hybridization, concentration of sp<sup>3</sup> hybridization and oxygen functional groups. For graphene it allows you to determine if the sample has been oxidized by ambient conditions as well as confirm that the sample will have sp<sup>2</sup> hybridization. In GO, XPS becomes particularly useful. When working with GO, we often seek to remove oxygen functional groups by reduction and increase sp<sup>2</sup> hybridization. XPS allows us a simple and easy method to quantifying what functional groups are present before and after reduction and what, if any, changes have been made to the concentration of sp<sup>2</sup> hybridized carbon atoms. In Figure 2.15a, the C1s spectra of several samples of rGO synthesized using different chemical reducing agents is shown.<sup>58,154,155</sup> As-synthesized GO, has a high concentration of a diverse set of oxygen functional groups as labeled on Figure 2.15A. We can first examine sp<sup>2</sup> and sp<sup>3</sup> hybridized carbons at 284.5 and 285 eV. These are important for studying how graphene-like the rGO is, as graphene is composed only of sp<sup>2</sup> hybridized carbon. The oxygen functional species, C-OX, C=O and XO-C=O, can be found at ~286.4 eV, ~287.8 eV and 288.9 eV. After reduction, we can determine what concentration of oxygen functional groups have been removed and if there has been restoration of sp<sup>2</sup> hybridization.<sup>58,72</sup> In



addition, XPS can be used to identify the configuration of nitrogen that has been doped into graphene or GO. Figure 2.15b contains a typical XPS N1s spectrum for nitrogen doped graphene (NG). The nitrogen peak can be deconvoluted to identify the nitrogen doping configuration and the peak area used to quantify the concentration. Pyridinic, pyrrolic and graphitic can be found at  $\sim 398.6$  eV,  $\sim 400.5$  eV and  $401.4$  eV, respectively.<sup>107,156</sup>

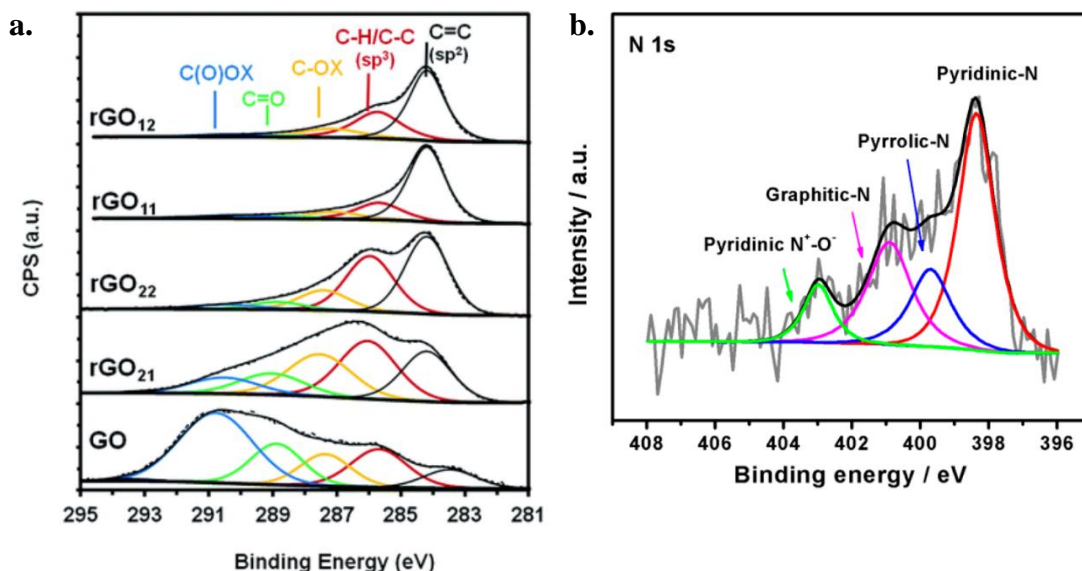


**Figure 2.15:** (a) C1s spectra from XPS for GO and rGO that had undergone different levels of reduction. The main oxygen functional groups for GO are labeled in each of the GO samples.<sup>154</sup> (b) A typical N1s spectra from XPS for nitrogen doped graphene species. The different nitrogen bonding configurations are labeled at their respective binding energy.<sup>156</sup>

XPS can also be used for phase identification in MoS<sub>2</sub>. The phase transformation by organometallic chemistry never has 100% efficiency rate for conversion.<sup>25,123,124</sup> Using XPS, we can differentiate between the phases and calculate the percentage. The Mo 3d spectrum in MoS<sub>2</sub> yields two characteristic peaks as shown in Figure 2.16a.<sup>157</sup> 2H phase MoS<sub>2</sub> will have stronger intensities at higher binding energy with the two peaks at  $\sim 229.5$  eV and 232 eV. Due to the change in crystal structure and increased in surrounding electron density<sup>158</sup>, 1T phase MoS<sub>2</sub> has peaks shifted to lower binding energies by  $\sim 1$  eV

so the two peaks can be found at  $\sim 228.25$  eV and  $231.35$  eV. When the sample is mixed, deconvolution of the doublet peaks allows us to determine the quantity of  $\text{MoS}_2$  in the 1T phase and in the 2H phase. Similar behavior can be seen in the S 2p spectrum in Figure 2.16b, with shifts to lower binding energy for 1T phase  $\text{MoS}_2$ .<sup>25,123,124,158</sup>

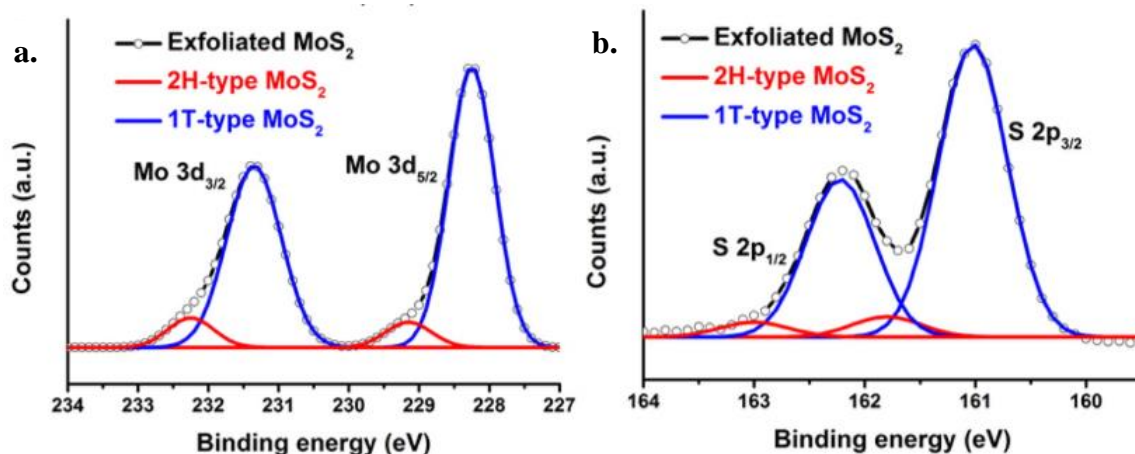
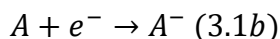
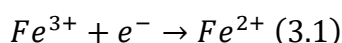


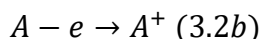
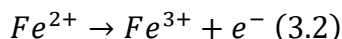
**Figure 2.16:** A typical (a) Mo 3d and (b) S 2p spectra for exfoliated  $\text{MoS}_2$ . The peaks can be deconvoluted in order to determine the concentration of the 1T and 2H phase.<sup>157</sup>

## Chapter 3. Electrochemistry

Electrochemistry is the field of chemistry pertaining to the phenomena occurring between electrical potential and chemical reactions. It can also be thought of as the use of electricity to drive a chemical reaction or harvesting the energy of a chemical reaction to generate electricity. These two ideas are classified into electrolytic cells or applying voltage to start a chemical reaction, and galvanic cells also known as generating electricity with a chemical reaction. This work will be primarily focused on electrolytic cells. In electrochemistry, there is always a transfer of electrons during a reduction or oxidation (redox) reaction. If a chemical species is being oxidized, it is losing or donating an electron; while if it is being reduced, it is gaining or accepting an electron. Reduction and oxidation reactions will typically be complementary to each other.<sup>148,159</sup> A simple reduction reaction is shown in Equation 3.1 where iron ions ( $\text{Fe}^{3+}$ ) are gaining an electron and being reduced to iron ions with a different oxidation state  $\text{Fe}^{2+}$ . A generalized half reaction for reduction is shown in Equation 3.1b.



If we reverse the reaction as shown in Equation 3.2, the  $\text{Fe}^{2+}$  ions are gaining an electron and being reduced to  $\text{Fe}^{3+}$ . Equation 3.2b shows a generalized oxidation half reaction.



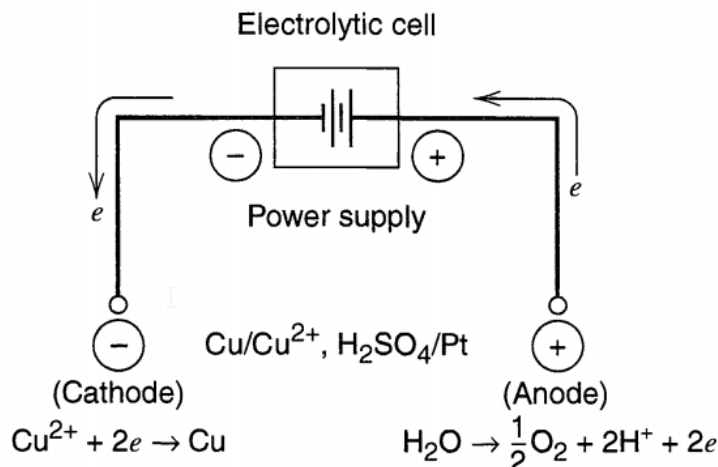


**Figure 3.1:** A classic example of an electrolytic cell. Copper ions are reduced at the cathode to form copper metal while water is oxidized at the anode producing oxygen and hydrogen ions. Electrons are supplied to the cell by an external circuit to drive the reaction.<sup>159</sup>

An electrochemical system is composed of at least two electrodes in a conducting solution termed electrolyte. In an electrolytic cell, the positive electrode is called the anode and will undergo oxidation. In contrast, the negative electrode is termed the cathode and undergoes reduction.<sup>148,159,160</sup> As shown in Figure 3.1<sup>159</sup>, copper ions are reduced to copper metal at the cathode while water is oxidized to produce oxygen and hydrogen ions at the anode. When a voltage is applied between the electrodes, a current will flow between the electrodes via the conducting electrolyte. If electrons are transferred from the electrode to the electrolyte, the resultant current is cathodic current. In the opposite case, electrons transferred from the electrolyte to the electrode, it is anodic current. As electrochemical experiments move forward, the concentration of conducting ions will shift at the surface of the electrode as it becomes polarized. At the interface between the metal and solution, charge is built up similar to a capacitor. This can affect the voltage being applied to the cell, shifting the cell voltage to be different from what is being applied. To circumvent these issues, we use a third reference electrode that is nonpolarizable that has a well-known and steady potential. They also make it

convenient for comparing between different experiment, systems and apparatuses.

Potential is applied against the reference electrode, while current is measured between the electrode of study also called the working electrode and the counter electrode, which is chosen for its lack of interference. These three electrodes together comprise the three

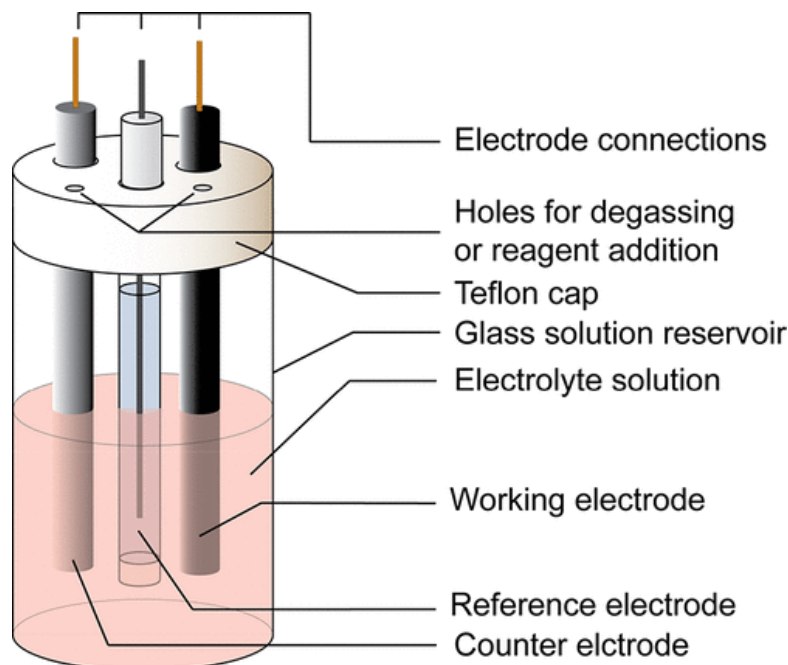


**Figure 3.2 :** A standard three electrode cell will contain a working electrode, reference electrode and counter electrode within a glass enclosure. Holes for gas purging are also found along the top of the cell.<sup>161</sup>

electrode cell as shown in Figure 3.2.<sup>161</sup> The primary reference electrode is called the normal hydrogen electrode (NHE). The standard reduction potential of the NHE is arbitrarily set to 0 V, allowing us to measure the potential of half reduction reactions against the NHE which we term the standard reduction potential,  $E^{\circ}_{\text{red}}$ . If the reverse reaction is measured, the sign of  $E^{\circ}_{\text{red}}$  is negated to reach the standard oxidation potential,  $E^{\circ}_{\text{ox}}$ . Unfortunately, due to electrical resistance, side reactions, and other catalyst deficiencies is it not possible to achieve these potentials.<sup>16,159</sup> Also, the NHE is an ideal device and impossible to construct, real world measurements typically use the reversible

hydrogen electrode (RHE) to approximate it and is used as the main experimental reference point. Typical experimental reference electrodes are the silver-silver chloride (Ag/AgCl) electrode that has a standard reduction potential of 0.197 V vs RHE in saturated potassium chloride or the saturated calomel electrode (SCE) which uses mercury and mercury chloride in saturated KCl that has a standard reduction potential of 0.242 V vs RHE.

### 3.1 Water Electrolysis

Water electrolysis is the electrochemical process of splitting water,  $\text{H}_2\text{O}$ , into its constituents of hydrogen gas,  $\text{H}_2$ , and oxygen gas,  $\text{O}_2$ . The process is more than 200 years old with the first electrolyzer being discovered in 1789 when wires from a friction based electrostatic generator were inserted into a container of water.<sup>162</sup> At standard conditions, the Gibbs free energy of the water splitting reaction is 237 kJ/mol which corresponds to a

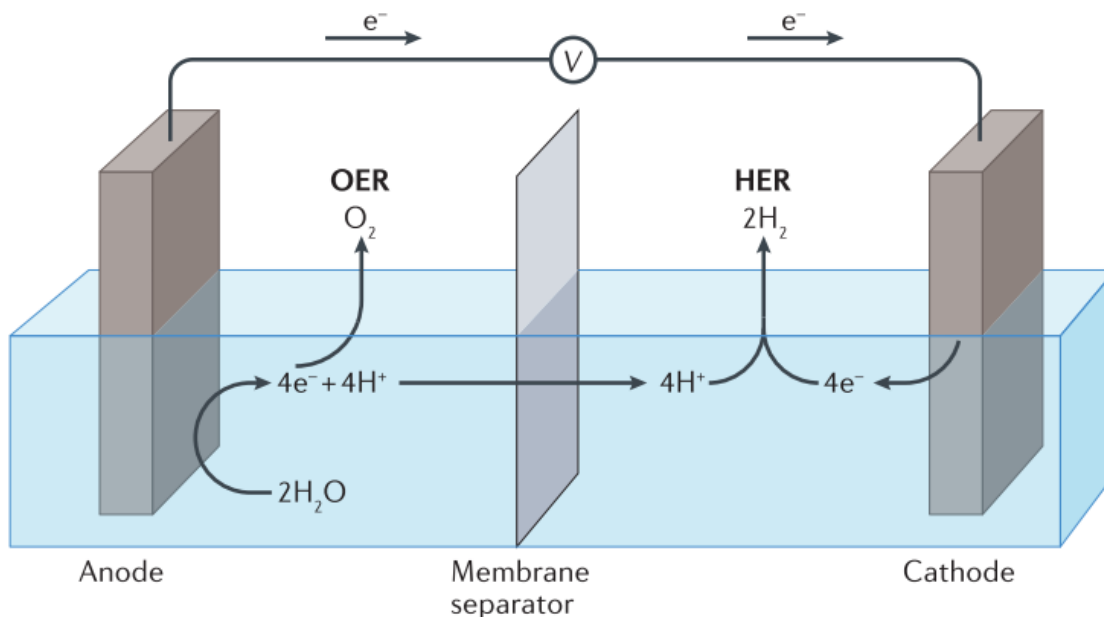


**Figure 3.3:** Electrolyzers will split water into its main components of hydrogen and oxygen. OER occurs at the anode for the production of oxygen gas while HER is at the cathode for the reduction of protons to hydrogen gas. Ideal electrolyzers will use a membrane to facilitate the flow of protons and prevent mixing of the gases.<sup>163</sup>

electrochemical cell voltage of 1.23 V. This is the minimum amount of voltage required to drive the water splitting reaction. The water splitting reaction can be divided into two half reactions. Hydrogen gas is formed as water is reduced at the cathode in the hydrogen evolution reaction (HER) while water is oxidized to release oxygen gas at the anode in the oxygen evolution reaction (OER).<sup>159,160</sup> A schematic of an electrolyzer is shown in Figure 3.3.<sup>163</sup> The half-cell redox reactions for HER and OER in acidic electrolyte are shown in Equations 3.1 and 3.2, respectively.<sup>159,160</sup>



Hydrogen is an energy carrier with nearly three times the gravimetric energy density of gasoline. As mentioned in Chapter 1, it has been proposed to be a replacement for fossil fuels by generating electricity in a fuel or directly drive an internal combustion engine. However, producing hydrogen in a cost-effective, clean and sustainable manner is challenging.<sup>24,160</sup> Efficient hydrogen production can be realized by optimization of water electrolysis with the appropriate electrocatalyst for HER. Platinum has been shown to be the best performing catalyst for the HER, however it is expensive and not abundant. The development of catalysts that are cost effective and have high electrocatalytic activity for HER is imperative to realizing hydrogen fuels as a viable energy source.<sup>105,159,160</sup>

A suitable electrocatalyst is cost-effective and consists of sustainable material, stable and high performance for the HER.<sup>163,164</sup> Using cost-effective materials will facilitate commercialization and sustainable materials suit the goal of reducing harmful emissions. Stability is also required as an electrolyzer is expected to function without failure in what

can be harsh conditions. The performance of an electrocatalyst will strongly depend on the adsorption energy, how it interacts with its reactants, due to the Sabatier principle. Electrocatalysts have been found to be most efficient when it is not too strong or too weak. When the adsorption energy is high, the reaction products will be unable to desorb from the catalyst surface resulting in low performance. Low performance is also observed if the adsorption energy is too low, as the reaction will be difficult to start.<sup>165,166</sup>

### **3.1.1 Molybdenum Disulfide for the Hydrogen Evolution**

#### **Reaction**

MoS<sub>2</sub> is an earth abundant layered material that has been studied as an electrocatalyst for the HER. Early work was performed on bulk MoS<sub>2</sub> and its applications for the HER and it was determined to have poor electrocatalytic activity.<sup>167,168</sup> However in more recent years as the two dimensional nature of MoS<sub>2</sub> has been explored and advances in nanomaterial synthesis, interest has grown in electrocatalytic applications of MoS<sub>2</sub> and other TMDs. Utilizing the layered nature of MoS<sub>2</sub> allowed for exposure of more catalytically active sites, making it a more viable candidate for electrocatalysis. Using density functional theory (DFT) calculations, the free energy of hydrogen adsorption ( $\Delta G_{H^*}$ ) can be estimated. When calculated on the edge of an MoS<sub>2</sub> nanosheet, as opposed to the basal plane, the  $\Delta G_{H^*}$  was found to be decrease after initial hydrogen adsorption and reaches nearly 0 eV. To experimentally confirm their results, the researchers prepared a membrane electrode assembly using platinum and MoS<sub>2</sub> nanoparticles grown graphite.<sup>169</sup> Further DFT calculations were done to study any differences between molybdenum terminated edges and sulfur terminated edges.



Molybdenum edges covered by 50% sulfur was found to be the best combination with a  $\Delta G_{H^*}$  of 0.06 eV, which is much smaller when compared to sulfur edges completely covered by sulfur at a  $\Delta G_{H^*}$  of -0.045 eV. In addition, when imaged using scanning tunneling microscopy (STM) the edges of MoS<sub>2</sub> nanoparticles appear bright, implying that they are metallic, in agreement with DFT calculations.<sup>43</sup>

Confirmation of the edge activity was done in seminal work by Jaramillo et al. In this work, MoS<sub>2</sub> nanoparticles were grown on to clean gold substrates in ultra high vacuum. Post growth sintering allowed for different shapes to expose fractions of edge sites, controlling the ratio between basal plane sites to edge sites. Using scanning tunneling microscopy, they were able to characterize the shape of the MoS<sub>2</sub> at nanoscale and determine the structure and length of the edges after synthesis. Electrochemical testing

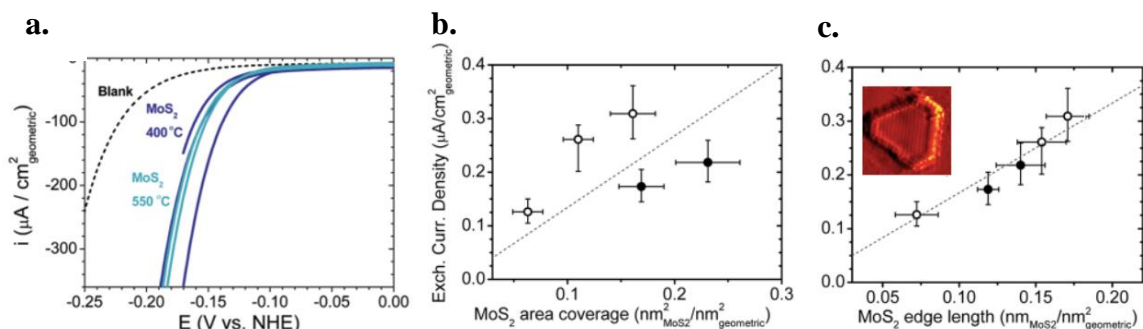


**Figure 3.4:** (a) Polarization curves of MoS<sub>2</sub> samples grown on gold substrates after sintering at 400 °C and 550 °C (b) Evolution of the exchange current density as a function of the MoS<sub>2</sub> area coverage (c) Demonstration of the direct relationship found between the MoS<sub>2</sub> edge length and exchange current density<sup>18</sup>

showed clear activity for the HER as shown in the polarization curves in Figure 3.4a.<sup>18</sup>

Polarization curves demonstrate that the electrochemical reaction has begun by a sudden increase in current while sweeping the potential. The potential at which the reaction turns on is known as the onset potential. Any extra potential or overpotential beyond the standard reduction potential required for the reaction to proceed.<sup>148,159</sup> Next they

examined the relationship between exchange current density, which is used to measure the electrocatalytic activity, and geometric area or edge length of the MoS<sub>2</sub> sample. When plotted against the geometric area in Figure 3.4b, the exchange current density shows no clear relationship. In strong contrast as shown in Figure 3.4c, when plotted against the MoS<sub>2</sub> edge length, they found a linear relationship with exchange current density; implying that this is where the active site and as you increase MoS<sub>2</sub> edge length the electrocatalytic activity increases. Finally, they calculated the turnover frequency (TOF), which for an electrochemical reaction is the number product atoms or molecules being produced per second per active site.<sup>43</sup> The TOF at the edges was found to be 0.02 s<sup>-1</sup> and comparable to Pt (111) at 0.9 s<sup>-1</sup>.<sup>18</sup> With this pioneering work, efforts focused on increasing the concentration of metallic edges to improve performance for the HER. Engineering the surface of MoS<sub>2</sub> to expose more defects has been accomplished using nanostructures and by introducing defects. Using a double gyroid silica template, Kibsgaard et al. were able to synthesize mesoporous nanostructures of MoS<sub>2</sub>. They first electrodeposit Mo metal onto the double gyroid silica template and by varying the deposition time are able to control the thickness of the resultant MoS<sub>2</sub> film. After electrodeposition, the resulting multi-valent MoO<sub>3-x</sub>(OH) undergoes sulfidization in H<sub>2</sub>S gas. Finally, the silica template is etched with HF, resulting in a mesoporous MoS<sub>2</sub> structure that has a high concentration of edge sites with controllable thickness. When comparing with other nanostructures with less exposed edges, the double gyroid nanostructure showed an improvement of a factor of two to four. However, as thickness of the films was increased and more edges exposed, the electrocatalytic performance began to suffer from poor electron transport due to the high resistance between layers of

MoS<sub>2</sub>.<sup>170</sup> Defects can be introduced into MoS<sub>2</sub> electrocatalysts by H<sub>2</sub> annealing and oxygen plasma<sup>171</sup>, argon plasma<sup>172</sup> and electrochemical generation<sup>173</sup>. In each case defects are being created on the basal plane in attempts to expose more edges and an increase in performance for the HER.

In our group, past members have taken a different approach. Due to the identification of the metallic edge sites as being highly active for the HER, we used the phase transformation of TMDs to convert from the 2H to the metallic 1T phase. This was first demonstrated using WS<sub>2</sub> with the strained metallic 1T' phase. The exchange current density was shown to have a linear relationship with the percentage of 1T phase in the catalyst. As the concentration of 1T phase was increased, so did the exchange current density.<sup>44</sup> Similarly, our group was able to synthesize 1T MoS<sub>2</sub> by lithium intercalation and subsequent chemical exfoliation. The polarization curves of different types of MoS<sub>2</sub> are shown in Figure 3.5a.<sup>17</sup> We can first see the clear improvement in current density and onset potential of 1T MoS<sub>2</sub> compared to 2H MoS<sub>2</sub>. In order to determine the effect of

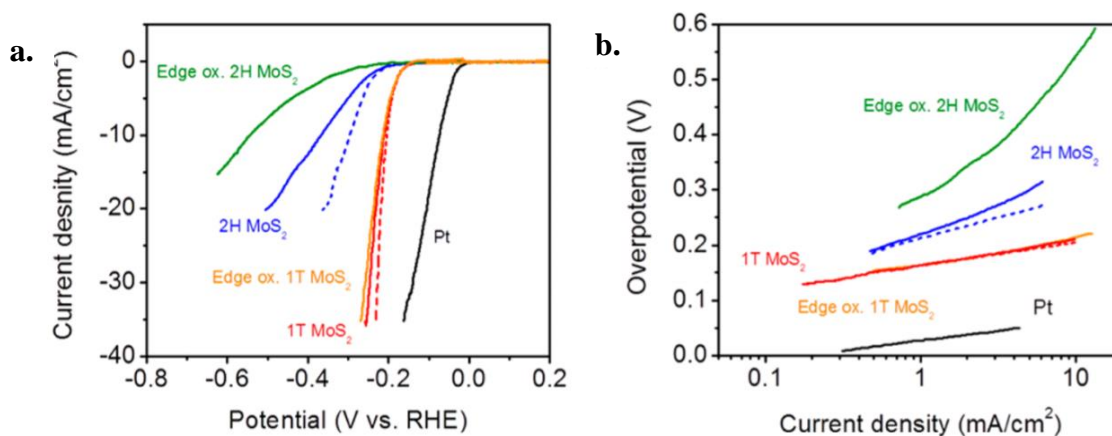


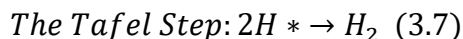
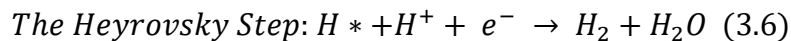
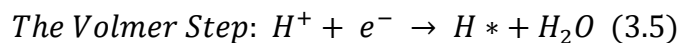
**Figure 3.5 :** (a) Polarization curves of 2H and 1T phase MoS<sub>2</sub> prepared by chemical exfoliation. Edge oxidized counterparts are also shown. (b) Tafel analysis of the corresponding polarization curves for 2H and 1T phase MoS<sub>2</sub> and their edge oxidized counterparts.<sup>17</sup>

edge concentration on the electrocatalytic performance, samples of 2H and 1T MoS<sub>2</sub>

were intentionally partially oxidized at the edges. This was confirmed by TEM as oxidized edges will create distortions in the lattice. From the polarization curves of the edge oxidized variants of 2H and 1T MoS<sub>2</sub>, we can see the substantial decrease in current and negative shift in onset potential for 2H MoS<sub>2</sub>. This implies that the edges in 2H MoS<sub>2</sub> are playing an important role in the electrocatalytic activity. Meanwhile the sample of 1T MoS<sub>2</sub> that has had its edges oxidized, shows very little change, so the edges in 1T MoS<sub>2</sub> are not the active site. Instead the active sites will be located on the basal plane as the entire sheet is metallic due to the phase transformation. Figure 3.5b contains the Tafel analysis extracted from the polarization curves. From the Tafel analysis, we can calculate the Tafel slopes which give some information about the reaction kinetics. The Tafel slope is in units of mV/dec so that it is the amount of overpotential required to increase activity by an order of magnitude. The Tafel slope of 1T MoS<sub>2</sub> was found to be at ~40 mV/dec while 2H MoS<sub>2</sub> is much higher at ~75-85 mV/dec. When compared with their edge oxidized counterparts, 2H MoS<sub>2</sub> shows an increase in Tafel slope while 1T MoS<sub>2</sub> remains unaffected. The improvement of performance for the HER in 1T MoS<sub>2</sub> is attribute to enhanced charge transfer kinetics due to the metallic nature of the 1T phase.<sup>17</sup>

### 3.1.2 Mechanism of the HER on Molybdenum Disulfide

The mechanism of the HER in acidic media can be broken down into three basic steps as shown in equations 3.5, 3.6 and 3.7, which are named the Volmer, Heyrovsky and Tafel steps, respectively.



$H^*$  represents an adsorbed hydrogen at an active site on the surface of the electrode. The HER will always proceed through the Volmer step as a hydrogen ion, or proton, reacts with an electron from the catalyst and is adsorbed onto the surface of the electrode to form  $H^*$ . The catalyst can then proceed through the Heyrovsky step or the Tafel step. In the Heyrovsky step, an adsorbed hydrogen site reacts with an additional proton and electron from the catalyst to form water and hydrogen gas that will desorb. The Tafel step involves the recombination of two hydrogen adsorbed sites and release of hydrogen gas.<sup>174,175</sup> Tafel slope analysis allows for assignment of an electrocatalyst to the Volmer-Heyrovsky or Volmer-Tafel mechanism. In addition, it can also be used to determine the rate limiting step for the reaction.<sup>175,176</sup> Pt is well known to undergo the Volmer-Tafel mechanism due to high adsorbed hydrogen site concentration.<sup>177</sup> In  $MoS_2$ , it has been shown that it follows the Volmer-Heyrovsky mechanism and the desorption of protons has been found to be the rate limiting step of the HER on highly conducting  $MoS_2$ .<sup>15,17,175</sup> Theoretical calculations using the nudged elastic band method suggest that there is a high barrier for the Volmer-Tafel mechanism for TMD materials.<sup>174</sup> If we consider that  $MoS_2$  undergoes the Volmer-Heyrovsky mechanism (Equation 3.5 and 3.6), we can see that each reaction step is highly dependent on charge transfer from the substrate to the catalyst and finally to an active site. While the Volmer step requires only a proton and a single electron to react, the Heyrovsky step requires a proton to meet with an adsorbed site and an electron to diffuse to the adsorbed site, or vice versa, to proceed. By optimizing charge injection into the electrode we may be able to enhance the catalytic performance of  $MoS_2$  electrocatalysts for the HER.

### 3.2 Fuel Cells and the Oxygen Reduction Reaction

Fuel cells are a type of electrochemical device that utilize electrochemical reactions to

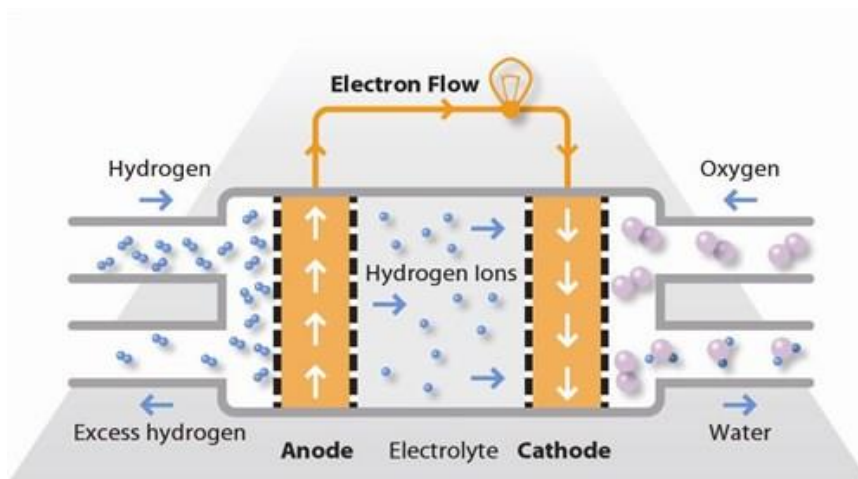
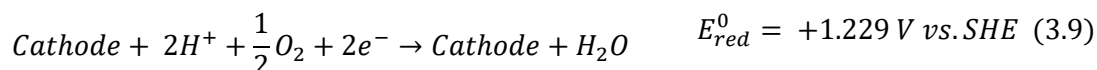


**Figure 3.6:** Schematic operation of a hydrogen-oxygen fuel cell<sup>178</sup>

produce electricity without the use of fossil fuels and subsequent air pollution. Fuel cells are galvanic electrochemical cells and operate in a similar manner to a typical battery. In an alkaline battery, we use a metal that can be oxidized at the negative terminal, also called the anode, with the donated electrons being used against a load to do work. At the positive terminal, also called the cathode, electrons from the circuit are absorbed to reduce the cathode material. Electrons pass between the two terminals via a liquid electrolyte. Similarly, a fuel cell uses some fuel and corresponding oxidant are consumed in an electrochemical reaction that has a net result of electrons that can be harvested in a circuit to do useful work.<sup>159</sup> The most typical fuel cell involves using hydrogen as it's fuel and oxygen for its oxidant. Gaseous hydrogen is provided to the anode electrode while gaseous oxygen is delivered to the cathode electrode as can be seen in Figure 3.6.<sup>178</sup> Hydrogen and oxygen gas react at electrocatalysts on the anode and cathode,

respectively. The basic electrochemical reactions at the anode and cathode are shown in equations 3.8 and 3.9.



Hydrogen is oxidized at the anode and is known as the hydrogen oxidation reaction (HOR) while oxygen is reduced at the cathode in the oxygen reduction reaction (ORR).

The electrons generated by the oxidation of hydrogen in equation 3.8 are extracted against the load, which is represented by the lightbulb in Figure 3.6. The hydrogen ions formed in equation 3.8 are transported to the cathode by a liquid electrolyte with a sufficient ionic concentration; this is typically a strongly acidic solution such as sulfuric acid. To complete the circuit, oxygen reacts with the hydrogen ions at the cathode and is reduced using electrons received from the substrate as shown in equation 3.9.<sup>16,159</sup>

Although the hydrogen-oxygen fuel cell was demonstrated in 1839, there are many challenges that have prevented commercialization of this technology.<sup>159</sup> A major barrier is the cost of state of the art electrodes. Current fuel cells use expensive and noble metals such as platinum, driving up the overall cost of the device. The development of abundant and cost-effective high performing catalysts for each electrode reaction is crucial to making fuel cells a viable energy alternative.<sup>14,16,176</sup>

The ORR can occur by two different pathways: a two-step two-electron process that involves an intermediate reaction to take place; and the more efficient four-electron process that directly reduces oxygen. Designing a catalyst to be selective for the four-electron process is desired. The reduction and oxidation reactions taking place in an

electrochemical system will vary according to the pH of the electrolyte.<sup>159</sup> In the case of the ORR, it is beneficial to have catalysts that function well in acidic pH because mainstream commercial devices use acidic media such as in polymer electrolyte membrane fuel cells (PEMFCs). PEMFCs are state of the art fuel cells that are the current leading technology for commercialization. The PEMFC is based on a hydrogen and oxygen system that has applications in transport, stationary fuel cell power generators and portable devices. The technology is attractive due to its use of a polymer membrane and its mild operating temperature range from 50°C – 100°C. The polymer electrolyte membrane used in PEMFCs helps make the device compact and safe to operate. The membrane will only conduct hydrogen ions, or protons, and prevents electrons from flowing through. It will also not allow gases at the anode and cathode to crossover.<sup>159,179</sup> Currently PEMFCs use finely dispersed platinum on carbon composite electrodes as their catalysts. Due to the high cost of platinum, these catalysts prevent commercialization and global adoption of the technology as an energy source. Reducing or completely eliminating the use of platinum in these catalysts is an imperative step in moving beyond fossil fuel use.<sup>16,180</sup>

### **3.2.1 Graphene catalysts for the Oxygen Reduction Reaction**

An appropriate electrocatalyst for the ORR that has high performance but is also cost-effective and abundant has not been found. Current leading catalysts use platinum which is expensive, thus raising costs considerably and can prevent scalability of fuel cell technology, and is susceptible to catalyst poisoning due to carbon monoxide and methanol adsorption onto the electrode. Carbon based catalysts have been recently shown



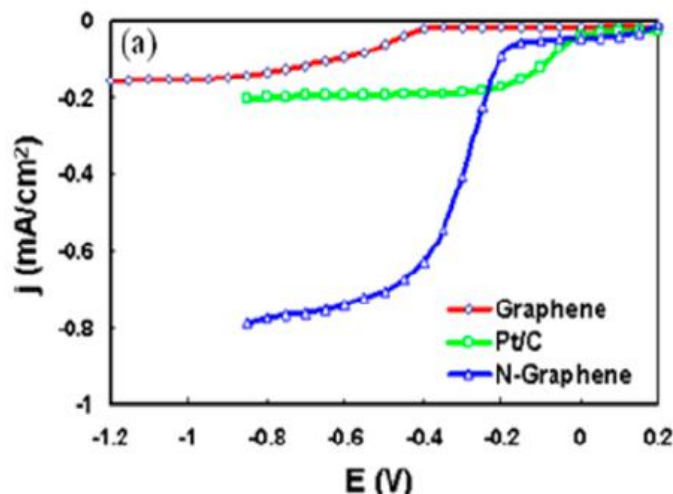


**Figure 3.7:** Rotating Ring Disk Electrode measurements for the ORR in air-saturated 0.1 M KOH of graphene, Pt/C and N-Graphene<sup>20</sup>

to be viable replacements for platinum as an electrocatalyst for the ORR.<sup>181</sup> They have been shown to have high performance when doped with heteroatoms such as nitrogen and have demonstrated long term stability in acidic conditions. Gong et al. first demonstrated that vertically aligned nitrogen-containing carbon nanotubes (VA-NCNTs) could act as ORR electrocatalysts without any kind of metal co-catalyst.<sup>182</sup> The authors showed the catalyst was selective for the four electron ORR process and was free from carbon monoxide electrode poisoning. Long-term operation stability was also observed as little degradation was shown in the current signal after 100,000 cycles.<sup>16, 182</sup> Using graphene grown by CVD and subsequent doping with nitrogen, Qu et al. showed improved performance between nitrogen doping and pristine graphene and has higher current than a platinum on carbon electrode.<sup>20</sup> The current density-voltage curves can be seen in Figure 3.7.<sup>20</sup> By minimizing the onset potential, it is possible to reduce the amount of efficiency loss within the fuel cell. Here we observe that platinum on carbon (Pt/C) has the most positive onset potential at  $\sim -0.1$  V vs Ag/AgCl with a saturated current density of  $-0.2$  mA/cm<sup>2</sup>. Pristine graphene shows two onset potentials at  $-0.45$  V vs Ag/AgCl and at  $-0.7$

V vs Ag/AgCl, indicating it follows the less efficient two-step reduction process mentioned previously. The current here saturates at less than  $-0.2 \text{ mA/cm}^2$ . In contrast to both Pt/C and pristine graphene, the nitrogen doped graphene (N-Graphene) has higher saturated current density of  $-0.8 \text{ V vs Ag/AgCl}$ . The onset potential is not as low as Pt/C at  $\sim -0.2 \text{ V vs Ag/AgCl}$ , but is still better than pristine graphene and exhibits only one onset potential, implying that it is following the more efficient one-step reduction process. The researchers further show that the nitrogen doped graphene is not affected by poisoning due to methanol and insensitive to carbon monoxide, while the Pt/C electrode has an instant reaction when the solution is contaminated.<sup>20</sup> Nitrogen doped graphene can also be prepared from graphene oxide. By thermally treating GO with melamine at high temperature, Sheng et al were able to prepare nitrogen doped graphene with nitrogen contents up to 10.1%.<sup>183</sup> Improvement is again shown when nitrogen is introduced into the graphene sheet.

Several have reported improvement for the ORR in nitrogen doped graphene electrodes using different doping methods such as pyrolysis of GO with urea<sup>184</sup>, compositing GO with nitrogen containing polymers such as polyaniline or polypyrrole<sup>185</sup>, edge-selective functionalization of graphene using 4-aminobenzoic acid<sup>186</sup> and many more. It is clear that with incorporation of nitrogen into the graphene sheet is important when considering graphene as an electrocatalyst for the ORR. However, only more recently has there been significant work to show that these materials still perform highly for the ORR under acidic conditions due to the viability of PEMFCs. Due to their less competitive ORR activity in acidic media, the catalytic performance needs to be improved before practical applications can be realized.

### 3.2.2 Mechanism of the Oxygen Reduction Reaction on Nitrogen doped Graphene

High concentrations of nitrogen dopants in carbon materials have lead to improved performance for the ORR<sup>20,103,106,187</sup>. As mentioned previously, nitrogen can dope into carbon lattices in a few different bonding configurations as shown in Figure 3.8 with the associated XPS binding energy. Pyridinic N, pyrrolic N and graphitic N can be found at ~398.6 eV, 400.5 eV and 401.4 eV, respectively. In particular, pyridinic N was found to

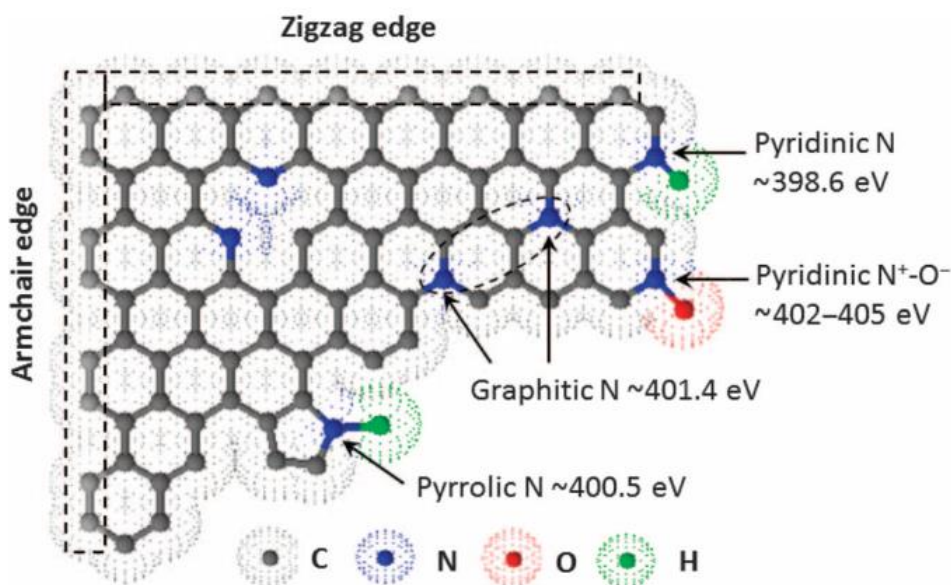


**Figure 3.8:** The common nitrogen dopant configurations in graphitic carbons and their corresponding XPS energies used for identification.<sup>106</sup>

improve catalytic performance for the ORR in carbon nanofibers<sup>188</sup> and carbon nanotubes<sup>189-191</sup> in basic media. In contrast, others have shown that graphitic N species are important for the ORR in graphitic arrays in basic media.<sup>192</sup> This has led to some controversy concerning what role nitrogen plays in carbon based catalysts for the ORR, especially in acidic media.<sup>106</sup> Recently, researchers have fabricated model HOPG

catalysts with high concentrations of either pyridinic N or graphitic N species. By correlating the ORR performance and the nitrogen dopant configuration, they found that pyridinic N is the active site for the ORR in nitrogen doped carbon materials.<sup>19</sup>

In graphene and graphene oxide based catalysts, nitrogen doping has also shown to improve the ORR catalytic performance in basic media.<sup>20</sup> By selectively doping the graphene<sup>193</sup> and graphene oxide samples<sup>185</sup>, the researchers found that the results from other carbon based catalysts for the ORR could be compared to graphene catalysts. Pyridinic N species were found to play a more important role for the ORR than other nitrogen dopant configurations; also showing that the samples composed primarily of graphitic N reduce oxygen using the less efficient two-step two-electron process.<sup>193</sup> Still there exist contrasting reports in graphene where they found graphitic N species to be the active site for ORR.<sup>20,194,195</sup> At the same time, in a graphene oxide based catalyst, Lai et al.<sup>185</sup> found graphitic N species to affect the limiting current density while pyridinic N species are involved in improvement of the onset potential.<sup>185</sup>

To understand the mechanism for the ORR in nitrogen doped graphene, researchers use DFT calculations to model the ORR in an acidic environment. Zhang and Xia<sup>196</sup> simulated the electron transformation process and found that on nitrogen doped graphene, the ORR undergoes the four-electron pathway while pure graphene does not. From their calculations, the system energy decreases with each reaction step, implying that the four-electron reaction can take place spontaneously. The active sites for the ORR will depend on the spin density distribution and atomic charge distribution; with addition of nitrogen into the graphene lattice there is an induced charge and / or spin redistribution that can enhance the ORR performance.<sup>196</sup> The same researchers revisited the mechanism and used

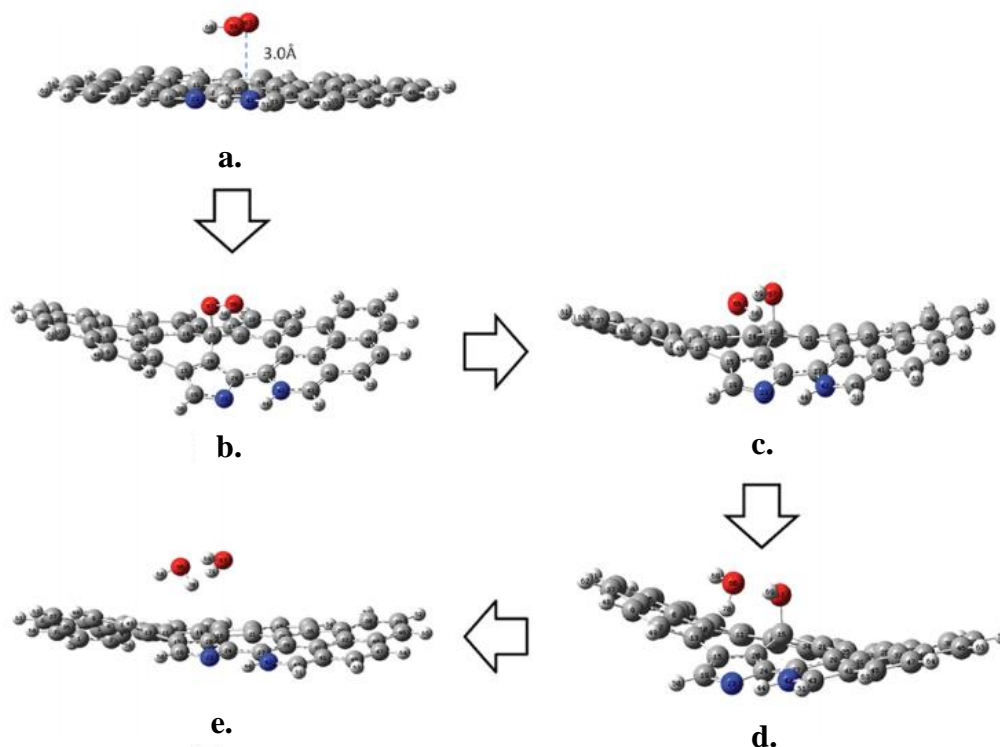


**Figure 3.9:** Simulated structure of the 4 electron transfers during the ORR on nitrogen doped graphene. **(a)** Initialized position of the OOH above the nitrogen doped graphene. **(b)** Adsorption of the OOH **(c)** The O-O is broken and hydroxide molecules are formed **(d)** A water molecule is generated by interaction with  $H^+$  with one hydroxide molecule. **(e)** The final water molecule is generated. Gray, blue, red and small white spheres represent carbon, nitrogen, oxygen, and hydrogen atoms, respectively.<sup>197</sup>

B3LYP hybrid DFT through Gaussian 03.<sup>197</sup> Here, they studied how the ORR activity is related to the material microstructure, dopant concentration and Stone-Wales dislocation defects. Stone-Wales dislocation defects are  $90^\circ$  rotations of two  $\pi$ -bonded carbon atoms which results in the conversion of four neighboring six-membered rings to two five-membered rings and two seven-membered rings. They are a topological defect found in  $sp^2$ -hybridized carbon materials and have been predicted to have an affect on electronic properties.<sup>197,198</sup> Schematically shown in Figure 3.9, the researchers model the optimal electron transformation in each step of the ORR. They first initialize the position of the adsorbing molecule above the nitrogen doped graphene in Figure 6a. The first electron transfer has two possible pathways: the adsorption of an intermediate molecule such as

OOH<sup>+</sup> (Figure 6b) or direct adsorption of O<sub>2</sub>. By positioning the intermediary molecules far away, they found that at far distances of ~3 Å the intermediate can still be adsorbed onto the graphene. Once adsorbed, the graphene nanosheet warps into the “saddle shape” as the carbon atom attached to the oxygen group comes out of the nanosheet and forms a tetrahedral structure. In direct O<sub>2</sub> adsorption, the O<sub>2</sub> molecule is unable to adsorb on to the nanosheet, even when put in bonding formation range. However, on a negatively charged graphene sheet, adsorption is possible, implying the nanosheet surface charge supports O<sub>2</sub> adsorption. Once the O<sub>2</sub> molecule is adsorbed a nearby H<sup>+</sup> can interact to form OOH. Still the energy for OOH<sup>+</sup> is an order of magnitude higher, indicating it is a more favorable reaction. As shown in Figure 6c, the O-O bond is then broken to form a hydroxide molecule in the second electron transfer. With the two hydroxide molecule, one attached and the other dissociated from the graphene plane, nearby H atoms in the reaction system will form water in the third and fourth electron transfers as shown in Figure 6d,e. As the water molecule desorb from the nanosheet, the graphene shifts back to its original shape.<sup>196,197</sup>

The mechanism can be summarized into the following equations in reaction order where an asterisk represent the chemisorption site.<sup>197</sup>

Reaction Order	Chemical Reaction <sup>197</sup>
(Electron Transfer)	
1	$O_2 + H^+ + e^- \rightarrow *OOH$ (3.9)
2	$*OOH + H^+ + e^- \rightarrow *OH + OH$ (3.10)
3	$OH + H^+ + e^- \rightarrow H_2O$ (3.11)
4	$*OH + H^+ + e^- \rightarrow H_2O$ (3.12)
Overall	$O_2 + 4H^+ + 4e^- \rightarrow H_2O$ (3.13)

Within this simulation, Zheng et al. investigate the effect nitrogen dopants have on the electron transformations. They found that large doping cluster sizes of nitrogen atoms greater than 2 will reduce the number of catalytic active sites per nitrogen atom.<sup>197</sup> Other models claim that clusters with three or four nitrogen atoms are more important than isolated nitrogen atoms and will be more efficient catalytic sites.<sup>199</sup> Taking into account the different nitrogen configurations, other models calculate the energy barrier for oxygen dissociation decrease with all types of nitrogen species, although graphitic N species are more important than pyridine N species.<sup>200</sup>

However, many of the studies mentioned above do not take into account the effect of metal contaminants and impurities.<sup>192,201,202</sup> While the authors claim that their catalysts are metal free, it is not always made clear if the catalysts are rigorously controlled to prevent any metal contaminants from being introduced.<sup>202</sup> Indeed, many studies use metal directly on their sample for patterning<sup>19</sup>, transfer to different substrates<sup>20</sup>, or during their synthesis<sup>185</sup>. Discrete elemental compositions of the final catalyst are often not given as evidence for their catalyst to be metal-free. The various metal impurities within the

catalyst can create the active site for the ORR and may be responsible for the uncertainty behind nitrogen doping configurations and their relationship with catalytic performance for the ORR. Wang et al.<sup>201</sup> fabricate electrocatalysts using the Hummers method to prepare their catalysts. They use inductively coupled plasma-mass spectrometry (ICP-MS) to determine the elemental composition of graphene oxide based electrocatalysts. Up to 1000 ppm of certain metals was found to exist within the catalysts and can have significant effects on the catalytic performance. Manganese oxide, which was found in the starting graphite material and in the graphene electrocatalysts was observed to effect their ORR onset potential greatly.<sup>201</sup>

With proper rigorous control of elemental contamination and with well defined nitrogen doping of graphene materials, it is possible to provide insight into the role nitrogen plays in forming active sites on graphene based catalysts.



## Chapter 4. Experimental Methods

### 4.1 Synthesis

In Section 2.4, we discussed the different synthesis methods for 2D materials in a qualitative manner. This thesis involves the use of GO synthesized by chemical exfoliation and graphene and MoS<sub>2</sub> grown by CVD; so a more in-depth description follows.

In our research group, we synthesize GO by the modified hummer's method originally prepared by Hirata et al.<sup>135</sup> Sulfuric acid (H<sub>2</sub>SO<sub>4</sub>), sodium nitrate (NaNO<sub>3</sub>), potassium permanganate (KMnO<sub>4</sub>), hydrogen peroxide (H<sub>2</sub>O<sub>2</sub>), hydrochloric acid (HCl) were purchased from Sigma Aldrich and used as received. First, a 600 mL – 700 mL beaker is placed within an ice bath and inside of a fume hood. Solid precursors are added to the beaker, which is composed of 2.5 g of natural graphite and 1.5 g of NaNO<sub>3</sub>, along with a magnetic stir bar of appropriate size. Finally, 68 mL of 95 % - 98 % H<sub>2</sub>SO<sub>4</sub> is added to the beaker, forming the reaction solution. The oxidation of graphite begins when 9.0 g of KMnO<sub>4</sub> is added slowly, over the course of about 1 hour, changing the color of the reaction solution to a dark green. Additional ice is added if necessary. If a dark green color is not achieved, the synthesis is not continued. After 2 hours in ice, the reaction solution becomes highly viscous, and is covered and set aside for 5 days. At this point, the reaction solution becomes gel-like. 200 mL of deionized water and 0.56 mL of 95 % - 98 % H<sub>2</sub>SO<sub>4</sub> are then added slowly forming a light purple solution. After stirring for 3 hours, the solution becomes dark brown and 6 mL of H<sub>2</sub>O<sub>2</sub> and 0.6 mL of concentrated HCl are added. Immediately as the H<sub>2</sub>O<sub>2</sub> is added, the dark brown solution becomes a

light yellow-brown and oxygen effervesces as the solution is stirred for 2 hours. The resultant graphite oxide is then washed and purified using centrifugation and dialysis. An initial step of centrifugation at 3000 rpm for 10 minutes is performed three times to remove the majority of any residual acids. The remaining graphite oxide is added to dialysis membranes and left in deionized water for at least two days, with the water being changed every hour. The purified graphite oxide can be added to deionized water and sonicated to form GO suspensions.

Single layer sheets of graphene were grown by CVD in a tube furnace with a quartz tube and stainless steel piping to control the environment. Methane ( $\text{CH}_4$ ), argon (Ar) and hydrogen ( $\text{H}_2$ ) gas were purchased from Airgas. 99.9 % copper foil was purchased from Alfa Aesar. Ammonium persulfate  $(\text{NH}_4)_2\text{S}_2\text{O}_8$  was purchased from Sigma-Aldrich and used as received. An image of a typical furnace is shown in Figure 4.1a along with an exaggerated scheme of the setup. We use  $\text{CH}_4$  gas as a precursor and copper foil as a substrate. Initially, copper foils are cleaned by electropolishing, to remove any oxide layer from exposure to air. The quartz tube is connected to argon and hydrogen, at 90% and 10% respectively, which is used as the carrier gas at the inlet. At the outlet we connect a vacuum pump which pumps continuously during growth. Before introduction of  $\text{CH}_4$ , the pressure is 160 mTorr and can go up to 300 mTorr during the growth. Initially, to remove air and moisture the flow rate is set to 100 standard cubic centimeters per minutes (sccm) for the carrier gas and heated to 100 °C for 15 minute. During growth, the carrier gas is set to 20 sccm while methane gas is flowed in at 10 sccm. The tube furnace is ramped to 1020 C in 40min and maintained there for 30 minutes. The furnace is then allowed to cool to room temperature and the graphene on copper samples

are removed from the furnace. Growth of graphene is confirmed by scanning electron microscopy. The graphene can then be transferred to arbitrary substrates using a poly(methyl methacrylate) (PMMA) – based method. A6 PMMA was purchased from Microchem. We first spincoat PMMA directly on top of the graphene on copper sample and cured on a hot plate at 150 C for two minutes. The copper is then etched away using 0.15 M  $(\text{NH}_4)_2\text{S}_2\text{O}_8$ . Once the copper has been etched, the PMMA and graphene float is transferred to deionized water to wash away any residual etchant. The PMMA and graphene float can then be transferred on to any substrate, typically a silicon wafer that has been capped with 300 nm of  $\text{SiO}_2$  ( $\text{SiO}_2/\text{Si}$ ). The PMMA is then washed away with acetone, leaving the graphene on top of the target substrate. On  $\text{SiO}_2/\text{Si}$  substrates, graphene can be identified by the change in color contrast as seen in Figure 4.1b. Large area graphene can be grown using this method with lateral dimensions nearing 1 cm.

Similarly, samples of single layer  $\text{MoS}_2$  were grown by CVD in a tube furnace. Molybdenum trioxide ( $\text{MoO}_3$ ), sulfur (S), n-butyllithium (1.6 M in hexane) were purchased from Sigma Aldrich. Si wafers covered with a 300 nm oxide layer were purchased from Nova Electronic Materials. Argon (Ar) gas was purchased from Airgas. Solid precursors consisted of 50 mg of  $\text{MoO}_3$  and 250 mg of S were placed in two alumina boats.  $\text{MoO}_3$  was placed in the center of the furnace while S is placed upstream. The substrates used were  $\text{SiO}_2/\text{Si}$  wafers. Once cleaned and cut to size, they were placed face-up on top of the alumina boat containing  $\text{MoO}_3$ . Argon gas was flowed through the tube at 200 sccm in order to evacuate air. The furnace was heated to 200 C for 15 minutes

to remove any residual moisture in tube or in the solid precursors. To perform the growth,

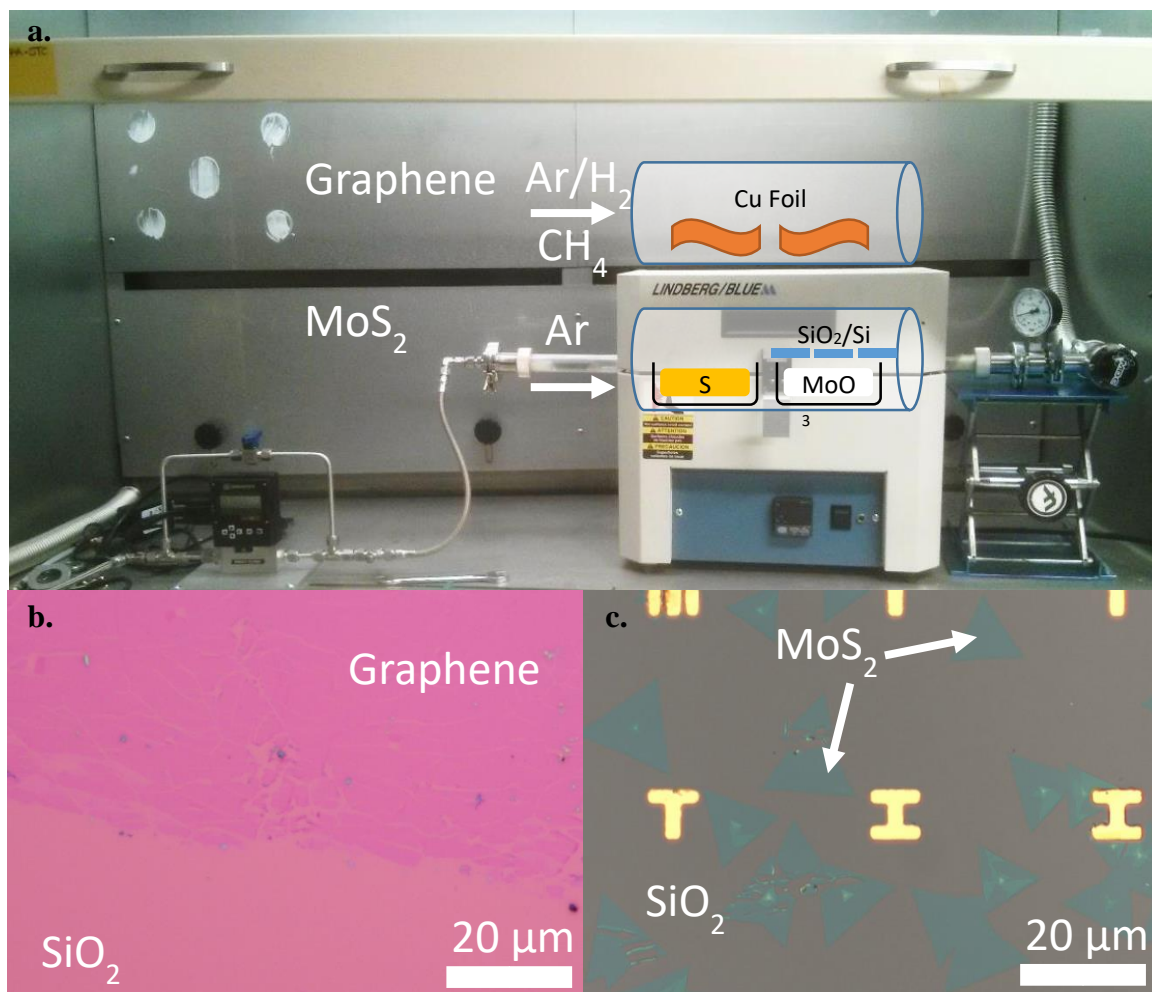


**Figure 4.1:** (a) A digital image of a tube furnace with gas line connections. In order to demonstrate the apparatus, a schematic of CVD growth is superimposed. Graphene is shown above MoS<sub>2</sub> growth. (b) An example of the graphene after it has been transferred from the copper foil growth substrate to SiO<sub>2</sub>/Si substrate. (c) Triangular MoS<sub>2</sub> samples after transferring from the SiO<sub>2</sub>/Si growth substrate to higher quality SiO<sub>2</sub>/Si substrates for device fabrication

the furnace was heated to 750 C under a 90 sccm argon flow. After 45 minutes, the furnace was cooled down to room temperature and the samples are removed from the furnace. Confirmation of MoS<sub>2</sub> growth is done by optical microscopy in which triangular sheets of MoS<sub>2</sub> crystals can be found, with a lateral dimension of 5 μm to 30 μm. These triangular flakes can then be transferred to arbitrary substrates using the PMMA transfer

method. First, PMMA is spincoated atop the  $\text{SiO}_2/\text{Si}$  substrates and cured on a hot plate at 150 C for two minutes. The PMMA coated sample is then floated on top of a 1.5 M KOH solution and placed into a box oven at 70 C. Over time, the 1.5 M KOH solution etches the  $\text{SiO}_2$  layer to release the PMMA and  $\text{MoS}_2$  sample floating at the surface of the liquid. This float can be transferred on to any substrate, for electronic applications, high quality thermal oxide  $\text{SiO}_2/\text{Si}$  substrates are used. Once transferred, the PMMA is washed away with acetone, leaving the  $\text{MoS}_2$  triangles. Finally, the sample is annealed at 300 for 1 hour in argon and hydrogen flow to remove residual PMMA. As in graphene,  $\text{MoS}_2$  triangular flakes can be identified on  $\text{SiO}_2/\text{Si}$  substrates as shown in Figure 4.1c.

## 4.2 Electrochemical Characterization

In Section 3.1.2 and Section 3.2.2, some electrochemical characterization is discussed in reference to the literature. A more detailed discussion follows that is focused on the experiments and calculations performed during this thesis work. The main technique used to characterize the electrocatalysts we prepared is cyclic voltammetry (CV). It is a powerful technique that allows for the investigation of reduction and oxidation processes occurring at an electrocatalyst. In CV, a potential is applied and a triangular waveform is applied in order to sweep the potential to a second point. To complete the cycle, the potential sweeps back to the initial point. During this cycle, the current between the working electrode and counter electrode is measured forming a voltammogram. A typical

voltammogram is shown in Figure 4.2a<sup>161</sup> for an ideal reversible reaction. Each of these peaks represents either an oxidation or reduction reaction has begun to occur at the

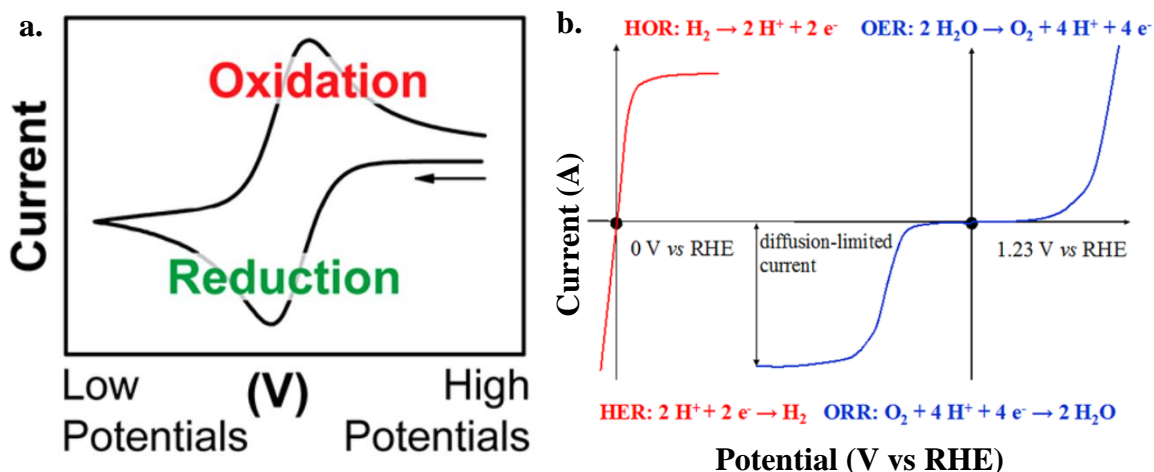


**Figure 4.2:** (a) A typical cyclic voltammogram for an ideal reversible reaction demonstrating the regions where oxidation and reduction occur.<sup>161</sup> (b) Polarization curves that have been extracted from ideal catalysts for the water splitting reactions (OER and HER) and the fuel cell reactions (HOR and ORR).<sup>105</sup>

working electrode.<sup>148,159</sup> From a CV, we can extract what is called a polarization curve.

Polarization curves are the standard in electrocatalysis and a simple method to determine performance for the electrocatalytic reaction in question. Ideal polarization curves for perfect catalysts are shown in Figure 4.2b<sup>105</sup> for the water splitting reactions, HER and OER, and the fuel cell reactions, ORR and HOR. If we examine the polarization curve for HER, we see that the current begins to increase at 0 V vs RHE, indicating the reduction reaction has begun to take place. As described above, the voltage at which this takes place for any electrochemical reaction is termed the onset potential. Most electrocatalysts will require potentials more negative than 0 V vs RHE to start the reaction and even more to generate reasonable current; benchmarks are often taken at 10 mA/cm<sup>2</sup>. This necessary potential is extra energy that needs to be supplied to the system in order to start the reaction and we call this the overpotential.<sup>148,159</sup> High performing catalysts will minimize

overpotential and have onset potentials as close as possible to the standard potential for the corresponding reaction. The onset potentials for ORR and OER are shown far from their standard potential of 1.23 V vs RHE due to the sluggish kinetics of their multi-electron transfer processes.<sup>105</sup> From the polarization curves, we can extract the Tafel slope by plotting the logarithm of current against the overpotential. Using the Tafel equation as shown below:

$$\eta = b \log \left( \frac{i}{i_0} \right) \quad (4.1)$$

where  $\eta$  is the overpotential (V),  $b$  is the Tafel slope (V/decade),  $i$  is the current density generated by the catalyst ( $\text{A}/\text{m}^2$ ) and  $i_0$  is the exchange current density ( $\text{A}/\text{m}^2$ ).<sup>159</sup> The Tafel slope can be thought of as the energy required as input for the system to increase activity by an order of magnitude. This analysis also yields the exchange current density which is related to the rate of oxidation ( $r_{\text{oxid}}$ ) and reduction ( $r_{\text{red}}$ ) as follows:

$$r_{\text{oxid}} = r_{\text{red}} = \frac{i_0}{nF} \quad (4.2)$$

where  $n$  is the number of electrons taking place in the reaction and  $F$  is Faraday's constant.<sup>159</sup>

When studying electrochemical reaction, it's possible mass transfer can be an issue. In the case of HER, the electrocatalyst can produce hydrogen bubbles at a high enough rate that it will passivate electrode surface and disrupt the CV. When studying the ORR, mass transfer becomes even more important as supplying reactant,  $\text{O}_2$  gas, can be difficult in static conditions.<sup>105,159</sup> Hydrodynamic methods allow for convective mass transport of the

reactants and products and typically involve rotation of the electrode. In order to rotate the electrode, we use a rotating ring disk electrode (RRDE) as shown in Figure 4.3a.<sup>147</sup> The standard glassy carbon disk is shown in the center while a platinum ring is on the outside. The RRDE allows for fresh reactant to flow to the electrode surface at a constant rate removing mass transport effects and we can use the platinum ring in collection experiments. As mentioned above, it is important to determine which pathway your ORR catalyst is undergoing, the two-electron pathway or four-electron pathway. Since the undesired two-electron pathway produces an  $\text{H}_2\text{O}_2$  intermediate, we can apply a constant potential to the outer platinum ring in collection experiments while running a typical hydrodynamic CV at the disk. By comparing the current at the disk and at the ring, we

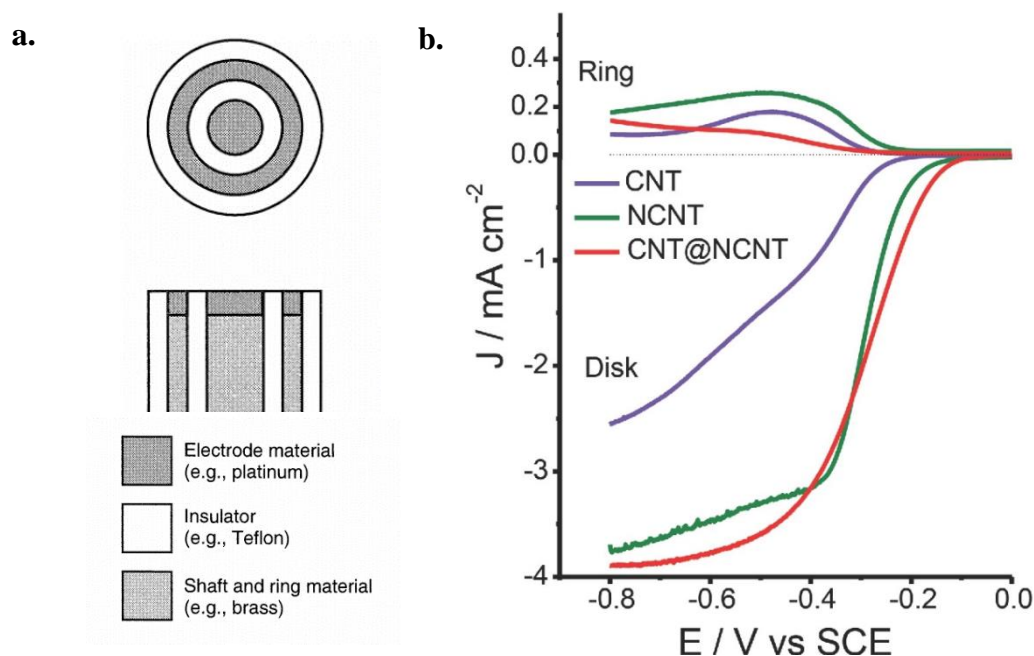


**Figure 4.3:** (a) A rotating ring disk electrode (RRDE) is composed of a disk electrode in the center with a concentric ring electrode. The two electrodes are separated by an insulating material and are both can be contacted independently.<sup>147</sup> (b) Polarization curves that can be extracted from data measured using an RRDE setup. Current density measured at the disk can be differentiated from current measured at the ring as shown.<sup>107</sup>



can calculate the percentage of  $H_2O_2$ , % $H_2O_2$ , being produced as well as the number of electrons being used in the reaction,  $n$ , using the following formulas:

$$\%H_2O_2 = 200 \cdot \frac{I_R}{N_C \cdot I_D + I_R} \quad (4.3)$$

$$n = 4 \cdot \frac{I_D}{I_D + \frac{I_R}{N_C}} \quad (4.4)$$

where  $I_R$  is the current at the ring,  $I_D$  is the current at the disk and  $N_c$  is the collection efficiency of the RRDE which has been calculated to be 0.40. A typical polarization curve from an RRDE is shown in Figure 4.3b using carbon nanotubes (CNT) and nitrogen doped carbon nanotubes (NCNT) as the electrocatalyst. The ring current will increase as the ORR proceeds due to production of  $H_2O_2$ . High performing catalysts for the ORR will minimize this current.<sup>16</sup>

Electrochemical impedance spectroscopy (EIS) is a powerful technique that yields insight into the capacitive and resistive nature of your electrochemical system and electrocatalyst. EIS allows you to probe an electrochemical system by applying a small alternating current (AC) perturbation over a range of frequencies.<sup>159</sup> The impedance ( $Z$ ) in an electrochemical system is defined by:

$$Z(\omega) = \frac{V(\omega)}{I(\omega)} = \frac{V \sin(\omega t)}{I \sin(\omega t + \Phi)}; \quad \omega = 2\pi f \quad (4.5)$$

where  $\omega$  is the angular frequency,  $V$  is the voltage at a time  $t$ ,  $I$  is the resultant current at time  $t$  and  $\Phi$  is the phase shift. This relationship is analogous to Ohm's Law and can be further simplified to

$$Z(\omega) = Z(\omega)(\cos(\Phi) - j\sin(\Phi)) = Z(\omega)e^{-j\Phi} = Z'(\omega) + jZ''(\omega) \quad (4.6)$$

where  $j$  is constant of  $\sqrt{-1}$ ,  $Z'(\omega)$  is the real component of the impedance and  $Z''(\omega)$  is the imaginary component. In a typical EIS experiment, we apply a constant voltage with a small AC fluctuating voltage of 10 mV at a certain frequency and the resulting current is measured. Using this data, the real and imaginary impedance are calculated. As the

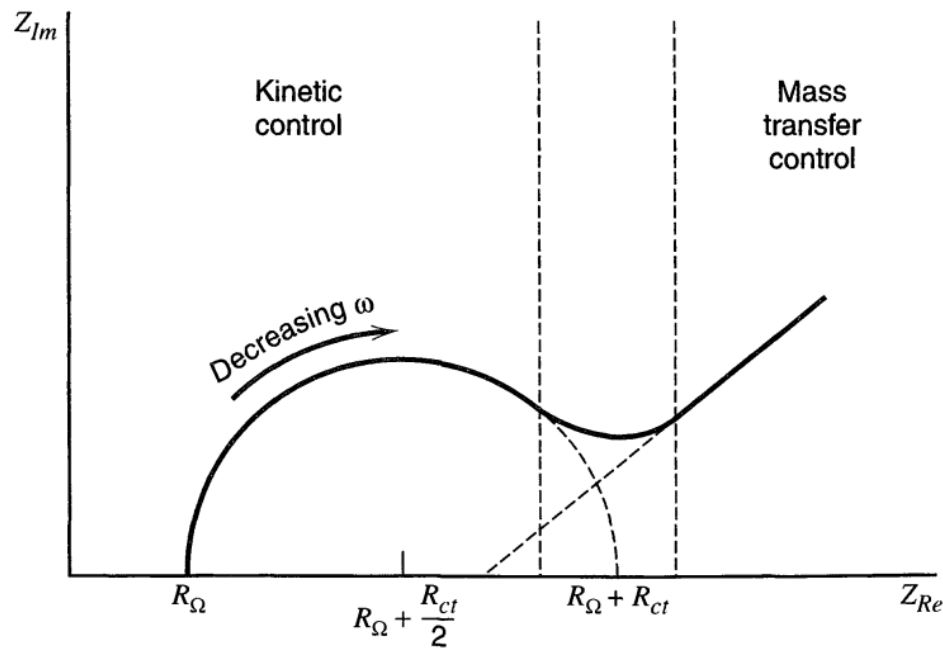


**Figure 4.4:** A typical Nyquist plot showing the impedance for an electrochemical system. Regions where the kinetics of the reaction or the mass transfer in the electrochemical system control the impedance are shown at high and low frequencies, respectively<sup>159</sup>

experiment proceeds forward, the frequency is varied from high to low frequency. The resulting real and imaginary impedance data can be shown in a Nyquist plot as in Figure 4.4.<sup>159</sup> Two distinct regions are labelled, where at high frequencies the kinetics of the reaction control the system and at low frequencies where mass transfer to the catalyst become more important. From a Nyquist plot, we can obtain two key characteristics of our electrochemical system the series resistance,  $R_\Omega$ , and the charge transfer resistance,

$R_{ct}$ . The series resistance arises from resistance in the potentiostat, wires and other connections to the electrochemical cell. The charge transfer resistance corresponds to the electron transfer from the catalyst to the electrolyte.<sup>159</sup> The series resistance allows for  $iR$  correction in polarization curves, and the charge transfer resistance is a key feature in optimizing electrocatalysts.<sup>203,204</sup>

### 4.3 Electron Beam Lithography & Device Fabrication

Lithography is used in the semiconductor and electronics industry to fabricate state of the art integrated circuits for modern computers. Typically, optical lithography is used to build these electronic devices due to its high throughput and uniformity.<sup>205,206</sup> However,

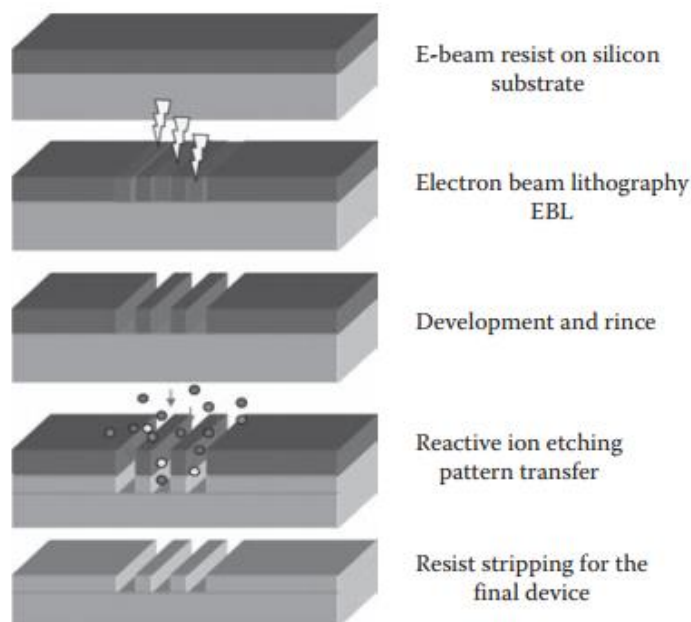


**Figure 4.5:** A standard workflow used in electron beam lithography for transferring a pattern written by the electron beam to the substrate. In this case the pattern is written and the underlying substrate is etched. When the resist is removed or washed away, the etched pattern remains on the substrate.<sup>205</sup>

for more flexible applications with custom contact designs, many turn to electron beam lithography. With this technique, we can deposit metal contacts on a sub-micrometer scale with discrete control. This allows us to make field effect transistors and other

electronic devices on samples that are on the microscale size with channel lengths under 1  $\mu\text{m}$ , such as on  $\text{MoS}_2$ <sup>47</sup> and graphene.<sup>207</sup> Patterns can be made to fit various random arrangements of material allowing a high degree of freedom with the positioning of the resultant device. Typical electron beam lithography uses an electron beam resist that is susceptible to electron irradiation, making it soluble to a corresponding developer. This allows for clearing of the resist in specific areas to allow for transfer of the irradiated pattern to the underlying substrate or deposition of metal to electronically contact the sample. A standard workflow is shown in Figure 4.5.<sup>205</sup> In our group, a typical electron beam lithography procedure uses PMMA as the electron beam resist. First, monomer methyl methacrylate (MMA) is spincoated at 4000 rpm and baked @ 120 °C for 2 minutes. Next, PMMA is spincoated as a top layer at 4000 rpm and baked at 180 °C for 4 minutes. This bilayer system is used to aid in lift off as the MMA layer has higher solubility in acetone and the PMMA layer will have more accurate patterning after electron beam irradiation. The samples are then placed into the electron beam lithography system, and a pattern designed using computer assisted design (CAD) is transferred to the sample by electron beam irradiation. The current used can vary from 100 pA to 10 nA, while the dosage is kept constant at 450  $\mu\text{C}/\text{cm}^2$ . After exposure, the sample is developed in a cold solution of isopropyl alcohol (IPA) and water in the ratio of 3:1 for 90 seconds and then rinsed in IPA for 60 seconds. We confirm that the microchannels have been opened without any thinning of the PMMA outside of our design by optical microscopy, which would be denoted by a discoloration of the PMMA. To complete the device, metal is evaporated by electron beam evaporation. Initially 5 nm of titanium is deposited at 0.2

nm/second as an adhesion layer to the 50 nm of gold that is deposited at 0.2 nm/second. The polymer layer is then dissolved away in acetone to remove the metal not meant for

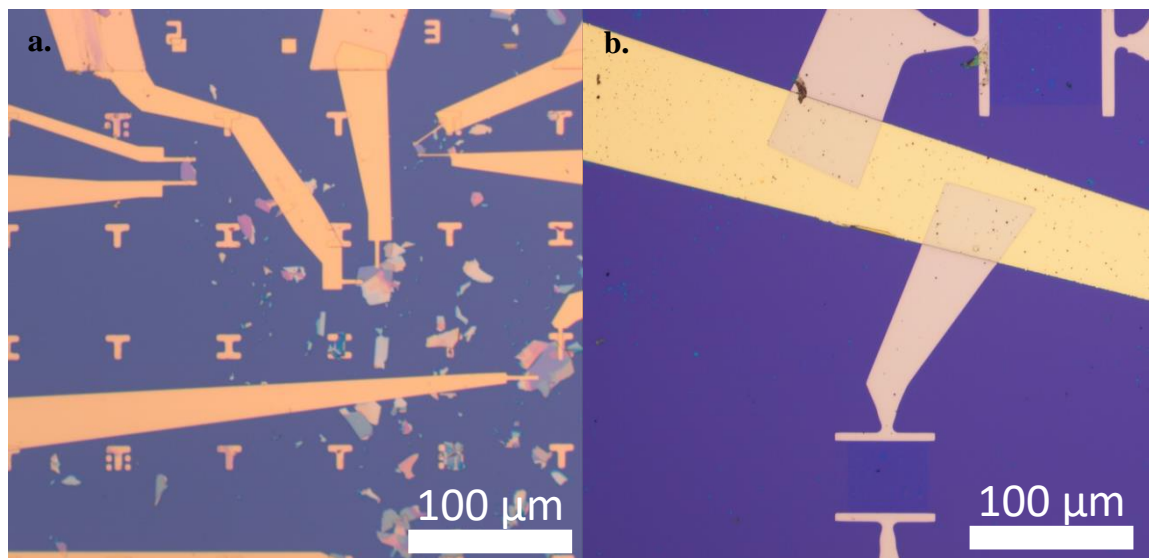


**Figure 4.6:** Completed electronic devices on (a) mechanically exfoliated MoS<sub>2</sub> and (b) CVD grown graphene. Two contacts are deposited in order to electrically probe the materials.

our devices. Once the lift off is complete, the devices are cleaned in IPA. Typical completed devices of MoS<sub>2</sub> and graphene are shown in Figure 4.6a,b, respectively.

## Chapter 5. Electrochemical Microcells on 2D MoS<sub>2</sub> nanosheets

In our group we have previously demonstrated the use of electron beam lithography to fabricate field effect transistors on mechanically exfoliated MoS<sub>2</sub> samples<sup>47</sup> and MoS<sub>2</sub> grown by CVD.<sup>119</sup> In this work, the researchers sought to reduce the contact resistance at the gold metal contacts, which are typically deposited during standard device fabrication. They achieved this by utilizing the phase conversion of 2H MoS<sub>2</sub> to the metallic 1T phase. This was done by first opening microchannels on the MoS<sub>2</sub> flake where a metal contact would go in a normal fabrication process. However, the exposed MoS<sub>2</sub> is first exposed to 1.6 M n-butyllithium in hexane for two days within an argon filled glove box. This will locally transform the phase of MoS<sub>2</sub> to the metallic 1T phase. Once metal is deposited directly on top of the 1T phase MoS<sub>2</sub>, a low resistance contact is formed but the channel of the transistor remains semiconducting. An improvement of nearly 300% is observed in on currents in the mechanically exfoliated MoS<sub>2</sub> devices with 1T phase contacts.

Inspired by this work, we sought to use electron beam lithography to fabricate devices to allow electrochemical testing of individual MoS<sub>2</sub> flakes for the HER and in parallel investigate the effect of decreasing the contact resistance on performance for the HER.

## 5.1 Physical Characterization of 2D MoS<sub>2</sub>

We grow the 2D MoS<sub>2</sub> samples by CVD, as described above. Before fabricating the devices, we examined the as grown material. We first used Raman spectroscopy to determine that the sheets are single layer as shown in Figure 5.1a. Raman spectra were obtained using a Renishaw 1000 system operating at 514 nm (2.41 eV). The CVD grown MoS<sub>2</sub> samples yield E<sub>2g</sub> and A<sub>1g</sub> vibrational modes at ~384 cm<sup>-1</sup> and ~403 cm<sup>-1</sup> respectively. The difference between the two peaks is less than 20 cm<sup>-1</sup>, implying that

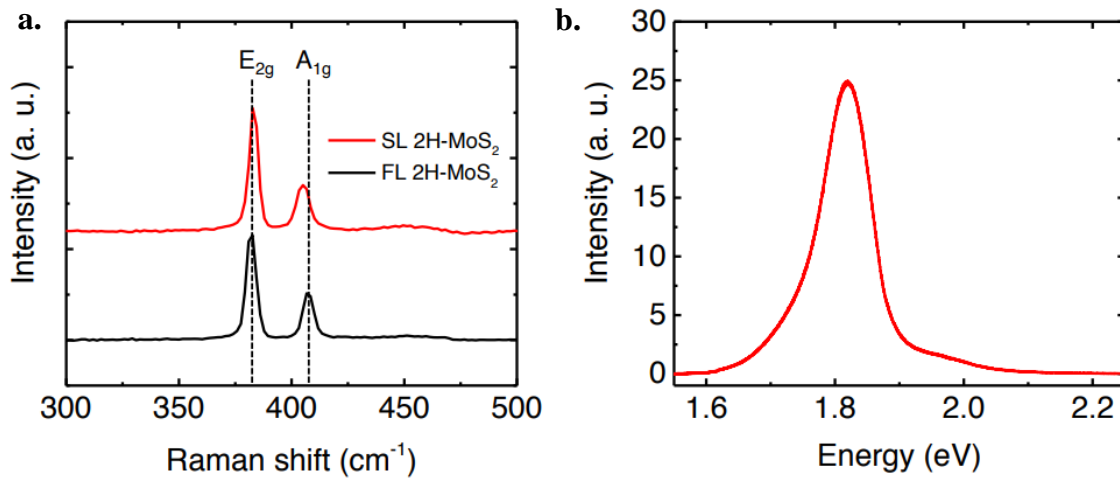


**Figure 5.1:** (a) Raman spectra for the samples of our CVD grown MoS<sub>2</sub> demonstrate that they are single layer. A few layer spectra is also included for reference. (b) A PL spectrum for our CVD MoS<sub>2</sub> shows a high intensity, indicating that our single layer MoS<sub>2</sub> exhibits a direct band gap.<sup>208</sup>

these samples are in the single-layer regime. Using photoluminescence (PL) spectroscopy, we observed an intense signal with a peak at ~1.8 eV in the CVD samples implying the sample is single layer as shown in Figure 5.1b.

In order to check for impurities from the CVD synthesis, we performed XPS after growth. XPS measurements were performed with a Thermo Scientific K-Alpha spectrometer. All spectra were taken using an Al K $\alpha$  microfocused monochromatized

source (1486.7 eV), a spot size of 400  $\mu\text{m}$  and a 15 eV pass energy. The XPS signals for the Mo 3d scan are shown in Figure 5.2a, while scans for S 2p are shown in Figure 5.2b. The Mo 3d scan peaks at  $\sim 229.5$  eV and  $\sim 232.6$  eV can be attributed to Mo  $3d_{5/2}$  and Mo  $3d_{3/2}$  corresponding to  $\text{Mo}^{4+}$  in 2H phase  $\text{MoS}_2$ . The absence of peaks corresponding to  $\text{Mo}^{6+}$ , which are expected at  $\sim 232.4$  eV and 235.5 eV, implies that the samples are oxide free as would be found in  $\text{MoO}_3$  or  $\text{SO}_x$ . The doublet found in the S 2p scan can be deconvoluted to two peaks at  $\sim 162.5$  eV and  $\sim 163.7$  eV which are attributed to S  $2p_{3/2}$  and S  $2p_{1/2}$  and correspond to  $\text{S}^{2-}$ .

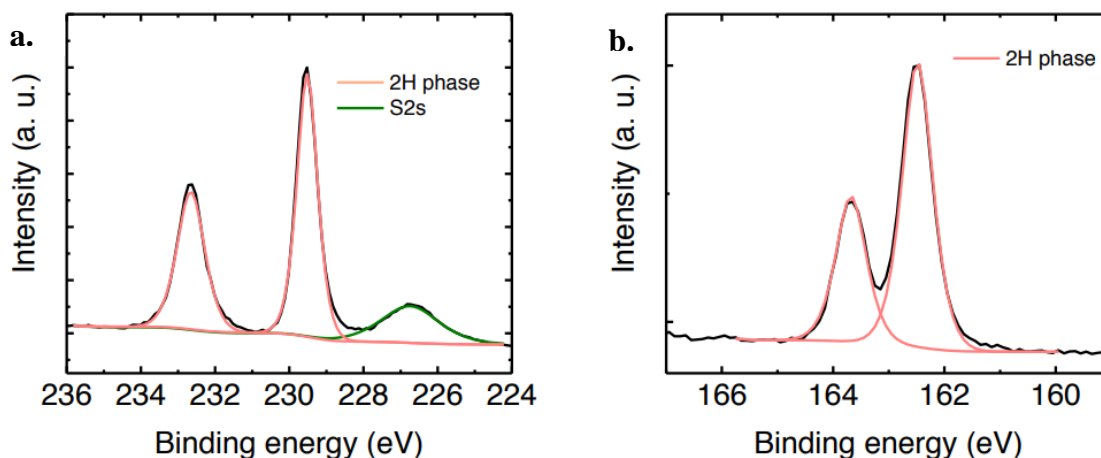


**Figure 5.2:** XPS spectra for the (a) Mo 3d and (b) S 2p demonstrate that our  $\text{MoS}_2$  samples are free of impurities such as oxides and are in the 2H phase.<sup>208</sup>

We next studied the single-layer  $\text{MoS}_2$  nanosheets by scanning electron microscopy (SEM). SEM images were taken using a Zeiss Sigma Field Emission SEM with an Oxford INCA PentaFETx3 EDS system (model 8100). In Figure 5.3a, we found that the color contrast across all the flakes was uniform, implying that they are all of a consistent thickness. When studied at high magnification as shown in Figure 5.3b, the edges of the  $\text{MoS}_2$  flakes are straight without hexagonal or dendritic structure. We can consider the



edge length of an individual triangular flake to be approximately the same as the geometric perimeter.

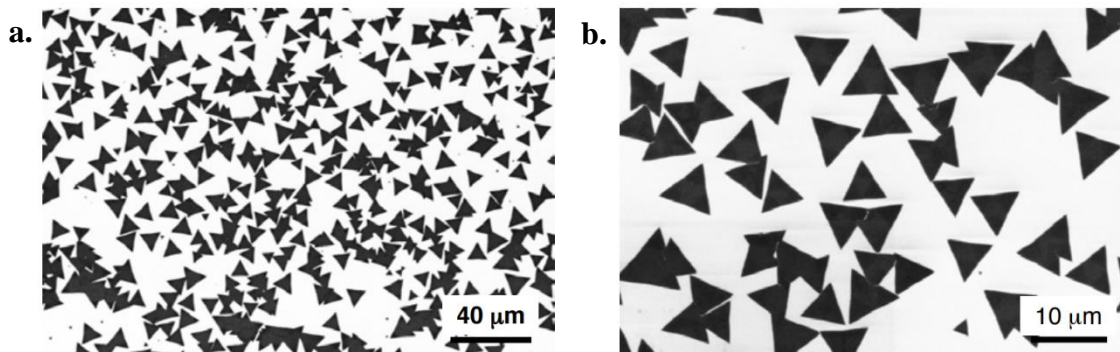


**Figure 5.3:** (a) Large-area SEM images of our as grown CVD MoS<sub>2</sub> samples. (b) Higher magnification SEM images shows individual nanosheets with sharp edges.<sup>208</sup>

Atomic force microscopy (AFM) was also used to confirm that the MoS<sub>2</sub> nanosheets grown by CVD were single layer. A typical topography AFM image is shown in Figure 5.4, where we can see a single layer MoS<sub>2</sub> triangular flake. A line scan is shown in white across the flake which corresponds to the superimposed height profile. The profile shows that the nanosheet is consistent and has a thickness of ~0.9 nm. The AFM image also agrees with the SEM images, showing that the edges of the MoS<sub>2</sub> flakes are straight. AFM images were obtained in Digital Instruments Nanoscope IV in tapping mode with cantilevers with spring constant of 40 N/m and tip curvature < 10 nm and a frequency of 325 kHz.<sup>208</sup>

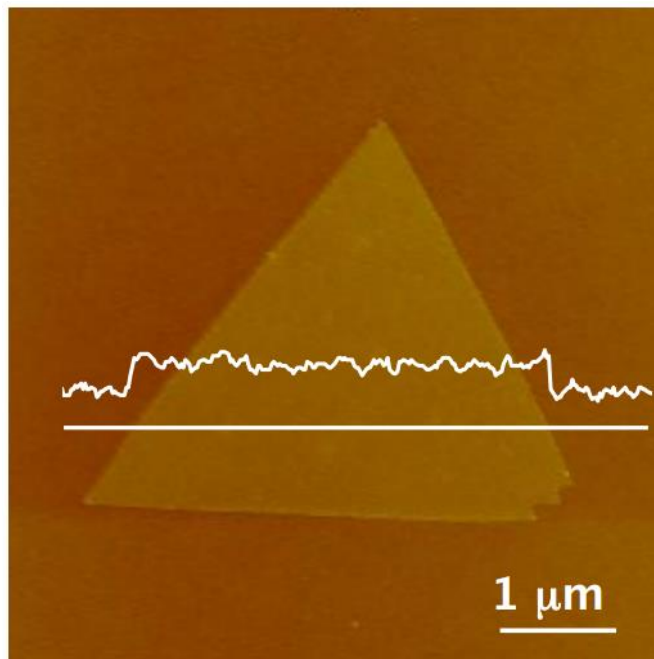


**Figure 5.4:** AFM image of a CVD grown MoS<sub>2</sub> nanosheet<sup>208</sup>

## 5.2 Devices with 1T Phase Contacts

A typical device on MoS<sub>2</sub> nanosheets is fabricated using gold contacts while the entire device is supported on a SiO<sub>2</sub> on Si substrate. This is suitable for electrocatalytic testing, as the SiO<sub>2</sub> is not conducting and we will have charge injection directly from the gold contact to the catalyst material, MoS<sub>2</sub>. Similar to our group's previous work we used electron beam lithography to selectively expose the MoS<sub>2</sub> area designated for metal contact to 1.6 M n-butyllithium (BuLi) in hexane and convert it to the metallic 1T phase. By varying the time the sample was exposed to the reducing agent, we could partially convert the MoS<sub>2</sub> area to the 1T phase, but maintain the 2H phase in the rest of the monolayer sheet. A scheme for this process is shown in Figure 5.5. We first spincoated PMMA on top of 2H MoS<sub>2</sub> (Figure 5.5a,b) then using electron beam lithography we open

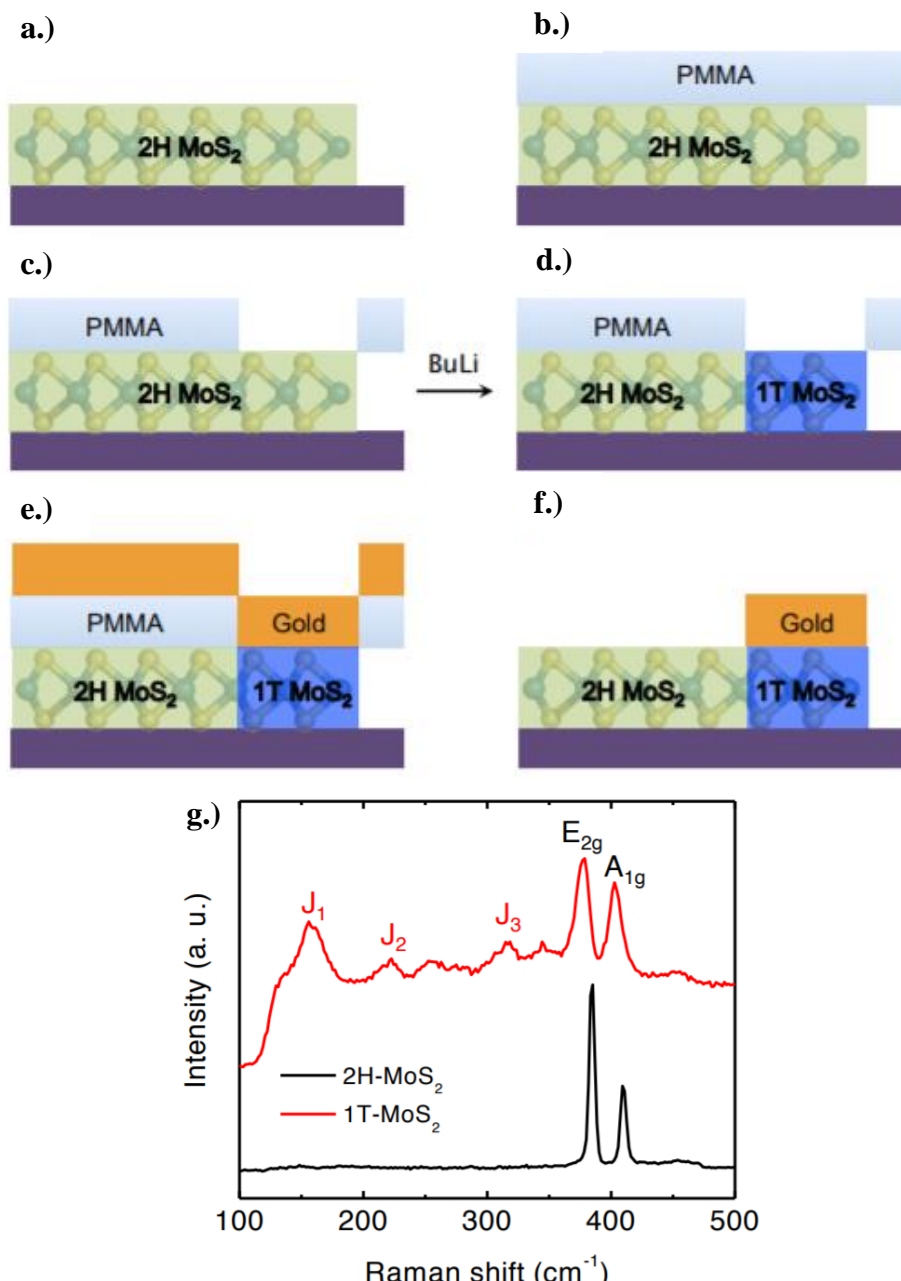


**Figure 5.5:** Successive steps for the fabrication of MoS<sub>2</sub> electrochemical microcells with 1T contacts and 2H basal planes. Initially, (a) pristine MoS<sub>2</sub> is coated with PMMA (b). When exposed to the electron beam, some PMMA (c) is removed. Upon exposure to n-butyllithium (d) we can convert to the 1T phase. (e) Gold is evaporated to coat the entire sample and after lift off (f) an electrical contact to the 1T phase region of the MoS<sub>2</sub> remains. (g) Raman spectra of the 1T phase region and 2H phase region of our MoS<sub>2</sub> samples confirm the phase transition<sup>208</sup>

microchannels on the MoS<sub>2</sub> (Figure 5.5c). These microchannels are exposed to n-butyllithium to convert to the 1T phase (Figure 5.5d). At this point, we can confirm a successful phase transition by Raman spectroscopy as shown in Figure 5.5g, where the

distinctive J<sub>1</sub>, J<sub>2</sub>, and J<sub>3</sub> peaks for 1T phase MoS<sub>2</sub> can be seen. Gold contacts are then deposited with subsequent lift-off to yield a device with 1T contacts. Alternatively, we could convert the entire sheet to the 1T phase, yielding devices with the lowest contact resistance. In this case, we first expose the entire sheet to n-butyllithium to convert to the 1T phase, then using standard lithography techniques we put down contacts to complete the device. This method allows for us to modulate the completed devices to have low or high contact resistance. By measuring the resistance of our devices, we can calculate the contact resistance using the following:

$$R = 2R_C + R_{MoS_2} \cdot \frac{L}{W} \quad (5.1)$$

where R is the resistance from the device, R<sub>c</sub> is the contact resistance, and R<sub>MoS<sub>2</sub></sub> is the sheet resistance of 2H phase MoS<sub>2</sub> and 1T phase MoS<sub>2</sub>. W and L correspond to the width of the contacts and the length or distance between the contacts respectively.<sup>208</sup>

### 5.3 Devices for Electrochemical Microcells with 2D MoS<sub>2</sub>

In order to electrochemically test individual monolayers of MoS<sub>2</sub>, we took the process one step further to fabricate electrochemical microcells using electron beam lithography. In addition to selectively opening microchannels for the metal contacts, we would open windows directly on top of the sample of interest. This defines the working electrode of our electrochemical microcell, which we expose to electrolyte. There are several steps of lithography in order to achieve a well-designed and functioning electrochemical microcell device. Figure 5.6 contains an optical image breakdown of the lithography steps required to fabricate these devices. Figure 5.6a,c,e,g show the same device at 10x

magnification while Figure 5.6b,d,f,h show a specific area on the substrate at 50x magnification. We use pre-patterned silicon substrates that have been capped with a 300 nm SiO<sub>2</sub> layer. The substrates are patterned using a conventional photolithography process using ultraviolet exposure. They consist of 16 gold contact pads that surround a 450  $\mu$ m by 450  $\mu$ m working area. Within the working area, an array of gold characters are also put down by photolithography. First, CVD MoS<sub>2</sub> is transferred onto the pre-patterned substrates using the PMMA transfer method. (Figure 5.6a,b). During this step, the MoS<sub>2</sub> triangular flakes are identified along with their position in reference to the gold characters on the pre-patterned chip. These are crucial for designing an accurate pattern for your metal contacts. Initially electron beam lithography is used to deposit metal contacts to electrically contact the nanosheet. The PMMA resist, is spincoated on top of the entire sample and cured at 180°C. A lithography pattern is designed to open channels from the large gold pads outside of the working area to an identified sample. Once the instrument is aligned with the CAD pattern and reference images, the pattern is written by the instrument upon exposure of the electron beam. The samples are developed in cold IPA and water for 90 seconds then rinsed in IPA for 60 seconds. After development, the microchannels are cleared of polymer and the result is microchannels without resist as shown in Figure 5.6c,d. Metal is then deposited using electron beam evaporation. The gold fills in the microchannels while the gold on top of PMMA is removed during lift off. The lift off process involves the dissolution of PMMA by acetone, resulting in metal not contacted to the substrate to be removed. Samples are then rinsed with IPA and dried gently with nitrogen. The devices are then as shown in Figure 5.6e,f. The sample is again covered with PMMA and cured using the same conditions.<sup>208</sup>

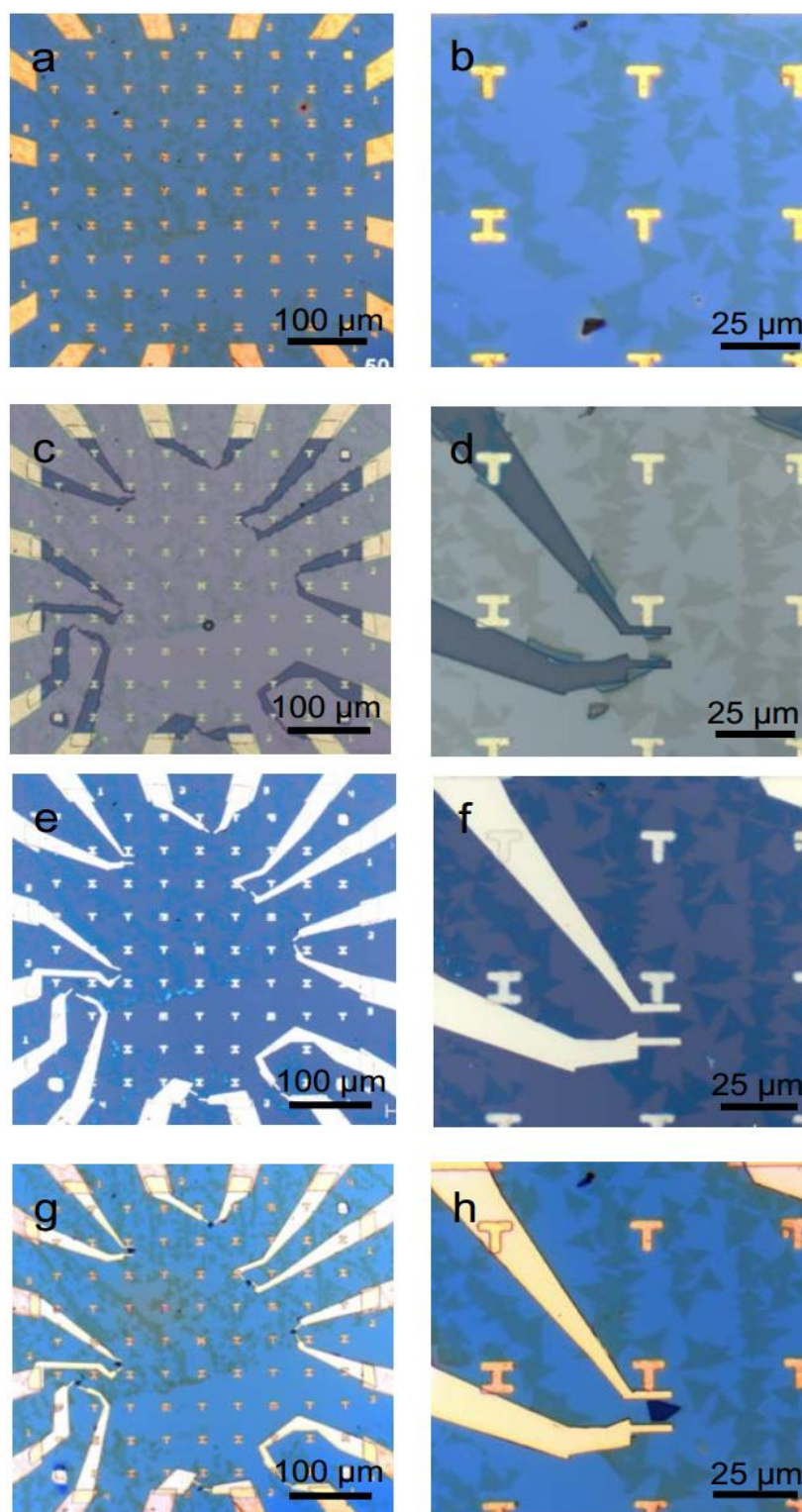


**Figure 5.6:** Optical pictures showing the different steps of the microcell fabrication. **(a and b)** The MoS<sub>2</sub> nanosheets are transferred on the 300 nm SiO<sub>2</sub>/Si wafer and covered with PMMA. **(c and d)** Electrode patterns are open on the PMMA layer. **(e and f)** The gold electrodes are then fabricated to contact selected individual nanosheets. Each MoS<sub>2</sub> nanosheet is contacted by 2 electrodes. **(g and h)** The microcell is covered with PMMA (passivation layer) and windows are opened via e-beam lithography to expose solely the MoS<sub>2</sub> nanosheets.<sup>208</sup>

We do another step of lithography and design the pattern with the goal to open small discrete areas or windows inside of each device. Special care is taken to not expose any gold and ensure only the MoS<sub>2</sub> catalyst is in the final working electrode. During this step, we are able to design various shapes and patterns into the working electrode with high resolution giving us a high degree of control over the final electrocatalyst area. The final devices with windows opened are shown in Figure 5.6g,h.<sup>208</sup> All areas except for the working electrode area are covered in PMMA to prevent contact with the electrolyte.<sup>208</sup>

## 5.4 Microcell Electrochemical Measurements

With the working electrode defined within our MoS<sub>2</sub> monolayer, we needed to complete the three electrode cell. Working electrode sizes that were used in this work were between 10 to 80  $\mu\text{m}$ . Standard three electrode cells would be inefficient at this scale and it limits the amount of electrolyte we can use; thus limiting the size of our counter and reference electrodes. To overcome this, we made a homemade Ag/AgCl reference microelectrode by dipping a Ag wire into 1.0 M HCl to form a thin coating of AgCl. Using a glass micropipette tip as the casing and 3 M KCl as the internal electrolyte, the Ag/AgCl wire is inserted into the tip and the reference microelectrode is sealed with parafilm. We calibrated the homemade reference electrode against a RHE calibrated saturated calomel electrode. To complete the three electrode cell we used a glassy carbon needle as the counter electrode. A digital photograph of the three electrode microcell setup is shown in Figure 5.7a with a corresponding schematic of the electrochemical testing of an individual MoS<sub>2</sub> triangular flake in Figure 5.7b. For this work, the



electrochemical measurements were performed using a Multistat 1480 potentiostat from Solartron Group in a 0.5 M  $\text{H}_2\text{SO}_4$  electrolyte solution. The CV measurements were performed by sweeping from 0 to -0.7 V vs Ag/AgCl at a scan rate of  $5 \text{ mV s}^{-1}$ . The absolute current measured was in the range of  $10^{-9} - 10^{-6} \text{ A}$ . The current density was calculated by normalizing the current to the total surface of  $\text{MoS}_2$  exposed to the electrolyte solution. We also performed electrochemical impedance spectroscopy using an SI-1260 Impedance/Gain Phase analyser from Solartron Group. Impedance

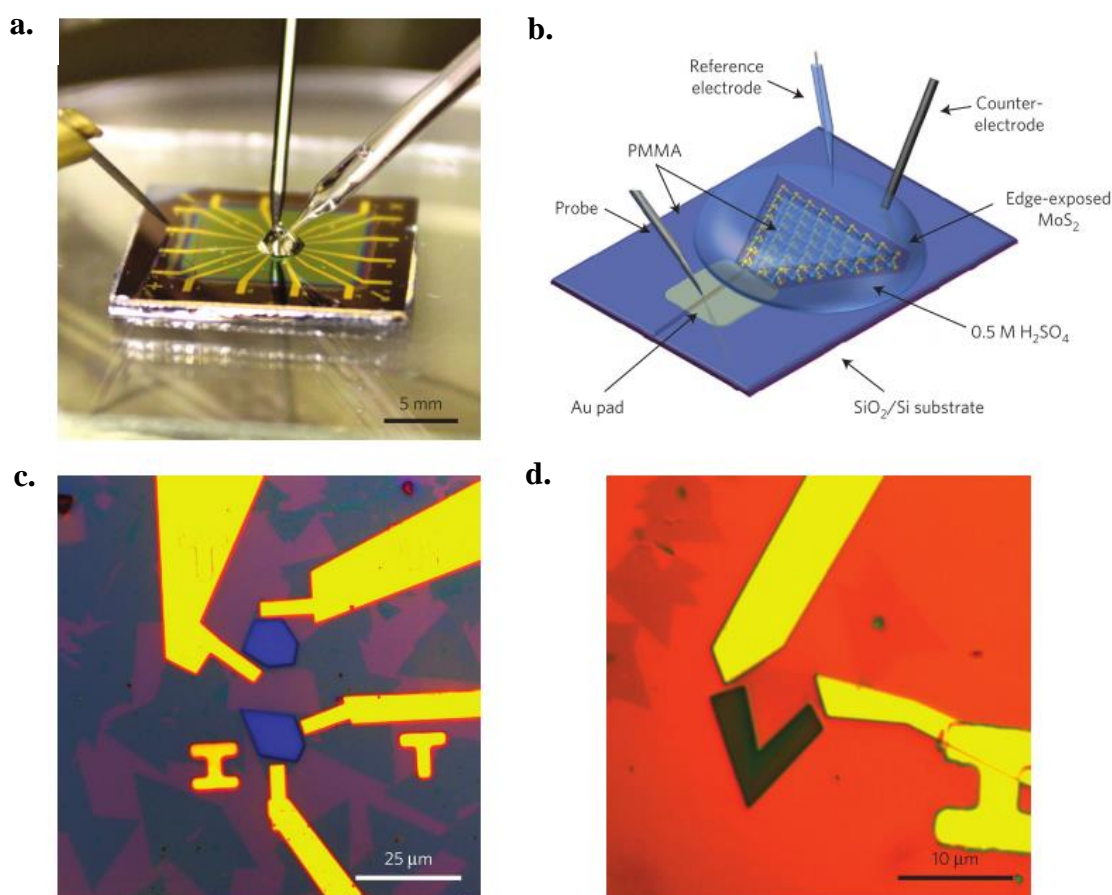


**Figure 5.7:** (a) Photograph of the electrochemical microcell. (b) Schematic of the electrochemical set-up showing a single layer of  $\text{MoS}_2$  deposited on  $\text{SiO}_2$  and contacted by one gold electrode. Glassy carbon counter electrode and Ag/AgCl reference electrode are also shown. Only the  $\text{MoS}_2$  sheet is contacted with the 0.5 M  $\text{H}_2\text{SO}_4$  electrolyte. (c,d) Optical microscope images of the different types of microcells: (c) edge covered and (d) edge exposed.



measurements were performed using an overpotential of 0.250 V vs RHE from  $10^6$  to 0.1 Hz with an alternating current voltage of 10 mV.<sup>208</sup>

Using electron beam lithography to define our working electrode area offers a high degree of flexibility. With this technique, we can not only determine the electrocatalytic behavior of individual nanosheets of MoS<sub>2</sub>, but also discrete regions of the triangular flake. As shown in Figure 5.7c,d, we were able to open windows directly on just the basal plane of a MoS<sub>2</sub> flake or focused along the edges. Since only the basal plane or edge of the MoS<sub>2</sub> flake is exposed to the electrolyte, we can measure the electrocatalytic behavior of only the basal plane or only the edge.

## **Chapter 6. Electrochemical Characterization of 2D MoS<sub>2</sub> for the Hydrogen Evolution Reaction**

Using this technique, we fabricated many electrochemical microcells on monolayer MoS<sub>2</sub> nanosheets synthesized using chemical vapor deposition. The electrocatalytic data shown is an average of the activity for devices with both basal plane exposed and edge exposed.<sup>208</sup>

### **6.1 Electrochemical Impedance Spectroscopy**

We first used EIS to observe any differences between the high and low resistance contact devices. Figure 6.1a shows typical Nyquist curves for microcells on single MoS<sub>2</sub> nanosheets with high and low contact resistance. We found that the internal series resistance ( $Z_s$ ) remains the same for both devices and relatively small at  $\sim 300\ \Omega$ . This implies that the contact resistance between the MoS<sub>2</sub> nanosheet and gold electrode is a

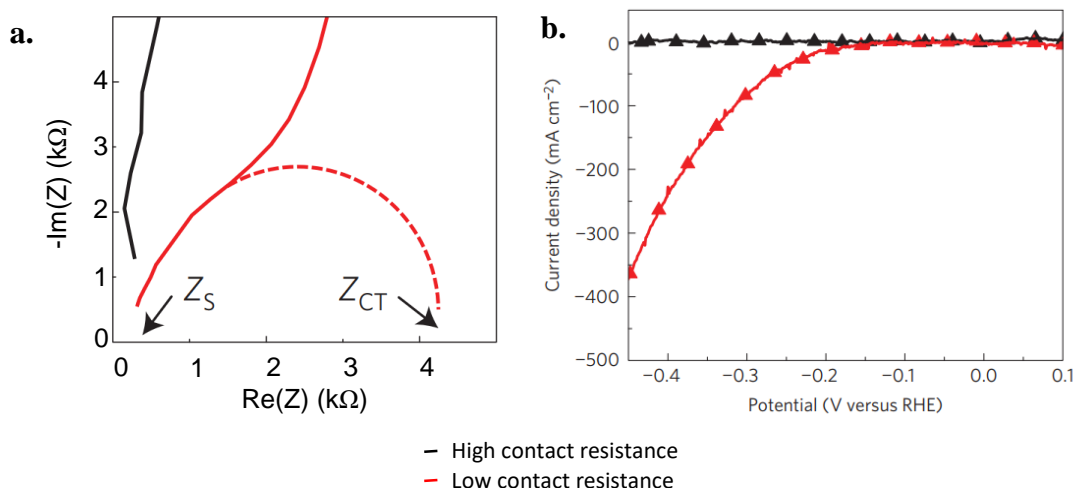


**Figure 6.1:** (a) Nyquist plots showing the impedance for devices with high and low contact resistance in black and red, respectively (b) Polarization curves measured from two  $\text{MoS}_2$  microcells with (solid line) and without iR correction (triangles). Curves for devices with high and low contact resistances are shown.<sup>208</sup>

variable independent from the internal resistance. The influence of the contact resistance can be seen in a marked decrease on the charge transfer resistance,  $Z_{CT}$ , which can be used to gauge how efficiently charger carriers are being transferred from the gold pad to the  $\text{MoS}_2$  electrocatalyst. From the Nyquist plot, we can see that the  $Z_{CT}$  of the low contact resistance devices is  $\sim 4 \text{ k}\Omega$  while for high contact resistance devices the  $Z_{CT}$  goes to near infinity. The reduced  $Z_{CT}$  in the low contact resistance devices suggest improved electron injection to the electrocatalyst. In Figure 6.1b are typical polarization curves for the corresponding devices. We performed an iR correction using the data extracted from the Nyquist plot in order to study the influence from the series resistance on our electrochemical experiments. After the iR correction is represented by the solid line, while without it is shown in triangle data points. There is minimal change between the two, showing there is little contribution from the internal resistance on these devices and the iR drop is negligible.<sup>208</sup>

## 6.2 Electrocatalytic Performance of 2D MoS<sub>2</sub>

The polarization curves of the current density of devices with varying contact resistances in 0.5 M H<sub>2</sub>SO<sub>4</sub> is shown in Figure 6.2a.<sup>208</sup> These polarization curves are averages taken from 2H and 1T phases and from the basal plane and edges of numerous samples. We found no relationship between edge concentration and electrocatalytic performance. Instead, as the contact resistance decreases, the HER performance increases with a decrease in the onset potential and overall increase in current density. It is noted that the current densities reported here are slightly lower than high-surface area mesoscopic electrodes reported in literature.<sup>15,21,209</sup> This is attributed to the flat nature of our MoS<sub>2</sub> electrodes.<sup>208</sup>

A figure of merit often used in catalysis is the turnover frequency (TOF) which has the units of s<sup>-1</sup>. The TOF is an indicator of the activity of the catalytic active sites and for the HER, it represents the total number of moles of H<sup>+</sup> that are being transformed into H<sub>2</sub> per active site per second. It can be calculated using

$$TOF = \frac{J}{n \times N \times 1.602 \times 10^{-19}} \quad (6.1)$$

where J is the current density in mA cm<sup>-2</sup>, n is the number of electrons taking part in the reaction, and N is the number of active sites. TOF values for MoS<sub>2</sub> catalysts for the HER remain virtually the same,<sup>176</sup> suggesting that the improvement in electrocatalytic behavior is due to an increase in the quantity of active sites, as opposed to an increase in the activity of each site. In standard electrocatalysis, it is often difficult to accurately calculate the TOF due to the challenge associated with precisely quantifying the number of active sites. However, the nature of the microcell structure allows accurate

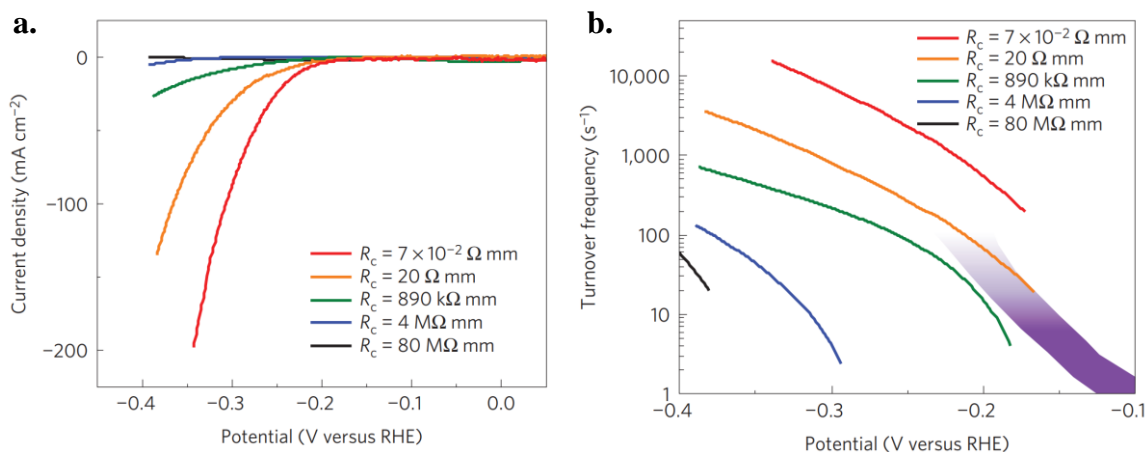


**Figure 6.2:** (a) Polarization curves obtained from MoS<sub>2</sub> devices with various contact resistances from 80 M $\Omega$  mm to  $7 \times 10^{-2} \Omega$  mm. As contact resistance decreases, the electrocatalytic performance increases (b) Evolution of the turnover frequency (TOF) with the overpotential. Our TOF values are compared to those obtained from metallic 2H-phsae MoS<sub>2</sub> edges grown on gold.<sup>18</sup>

measurements of the surface exposed to the electrolyte which we can use to calculate the density of the active sites. We assume that single sulfur vacancies are the only active site presented on the entire MoS<sub>2</sub> nanosheet, including vacancies from both the edge and basal plane. Using a lattice constant of 3.16 Å, the surface of a unit cell is calculated to be  $8.65 \times 10^{-16} \text{ cm}^2$ . With one sulfur atom per unit cell and assuming 9 % sulfur vacancies from our STEM results, the density of active sites is estimated to be  $1.04 \times 10^{14} \text{ cm}^{-2}$ . Using this we calculated the TOF values with applied potential for different contact resistances as shown in Figure 6.2b. For the low contact resistance devices, we see TOFs of  $>100 \text{ s}^{-1}$  and  $>1,000 \text{ s}^{-1}$  at overpotentials of 200 mV and 300 mV, respectively. Compared to other reports, our results are comparable for MoS<sub>2</sub> catalysts. For the lowest contact resistance, the activity of the MoS<sub>2</sub> nanosheets is higher than directly grown metallic 2H MoS<sub>2</sub> clusters grown on gold as shown with the purple region in Figure 6.2b from Jaramillo et.al.<sup>18,208</sup>

### 6.3 Contact Resistance and Electrocatalytic Performance for the Hydrogen Evolution Reaction

In order to better study the relationship between contact resistance and the electrocatalytic performance of our 2D MoS<sub>2</sub> microcells for the HER, we extracted three key characteristics and plotted them against the contact resistance in Figure 6.3a,b,c: onset potential, Tafel slope and the current density at an overpotential of 400 mV, respectively. Here we can see that exceptionally low onset potentials at less than 0.15 V can be achieved for low resistance contacts. Below a critical resistance value of ~10-100 k $\Omega$  mm, the Tafel slope and current density saturate at ~60 mV per decade and 100 mA cm<sup>-2</sup>. We can also see that in all three cases, similar HER performance can be achieved in the 2H phase where the edges are not exposed to electrolyte, eliminating them from the reaction. This shows that the basal plane of the 2H phase, which has typically been thought to be less catalytically active, will exhibit HER properties similar in the literature for edges and the 1T phase by improving the electrical contact. In devices where the 2H basal plane is exposed to electrolytes, we can fabricate the contact to have a low contact resistance at ~10<sup>-2</sup> k $\Omega$  mm. The HER performance of these devices is comparable to that of 1T phase and edge-exposed devices. Our results suggest that the catalytic activity of the basal plane and edges of CVD MoS<sub>2</sub>, irrespective of the phases, is comparable.<sup>208</sup>

In the case of the 2H-phase MoS<sub>2</sub>, efficient charge transfer will be limited and thus limit the Volmer reaction (Equation 3.5). If the catalyst material is not sufficiently conducting, then electron transport to the active sites is limited, preventing the Volmer reaction from proceeding. This can be seen in the Tafel slope analysis where low contact resistances

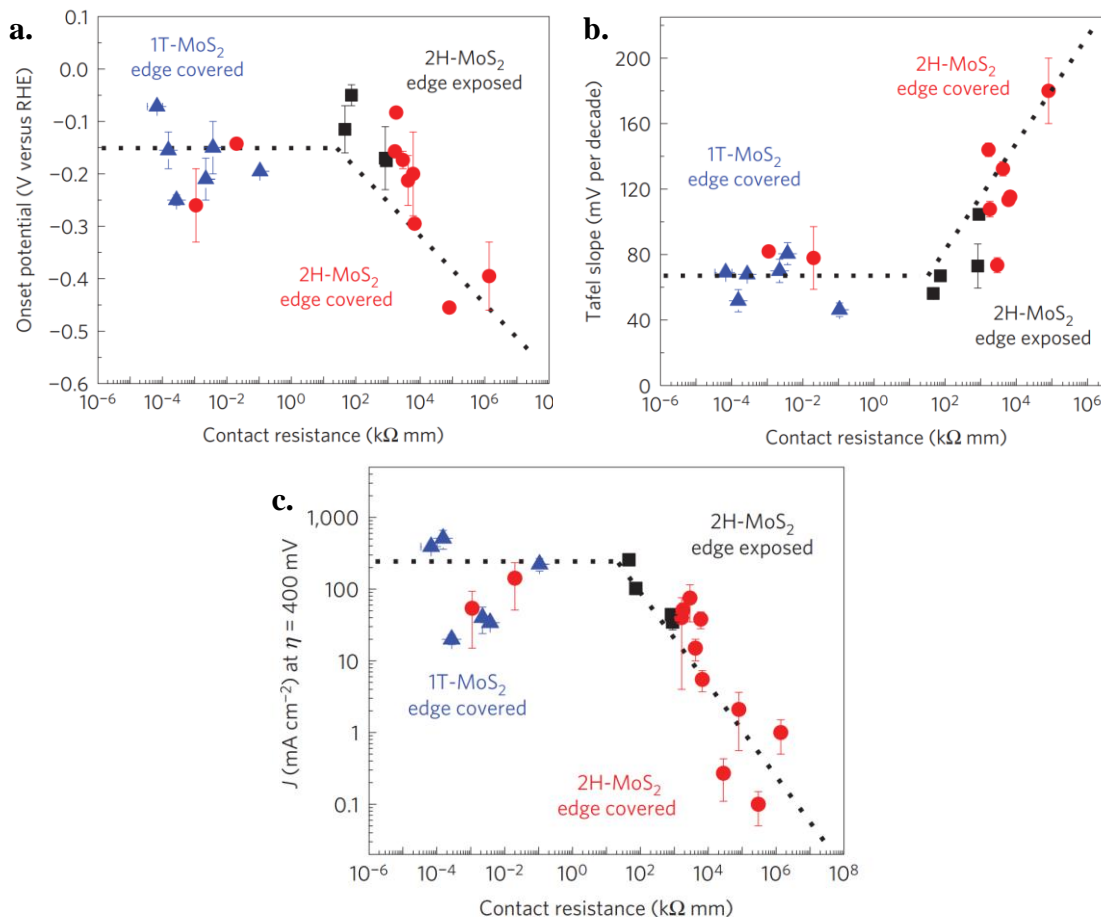


**Figure 6.3:** Variation of the (a) onset potential, (b) Tafel slope and the (c) current density measured at an overpotential of 400 mV with the contact resistance. The HER activity of the MoS<sub>2</sub> electrodes is progressively enhanced as the contact resistance decreases. No significant differences between edge-exposed and edge-covered devices have been observed from the samples, suggesting that both the surface and the edges of the MoS<sub>2</sub> crystals are active.<sup>208</sup>

yield low Tafel slopes of ~40 to 50 mV per decade while high contact resistances yield high Tafel slopes of up to ~120 mV per decade. This follows as Tafel slopes of ~40 mV per decade imply that the Volmer-Heyrovsky mechanism (Equation 3.5, 3.6) is being followed and that the Heyrovsky reaction (Equation 3.6) is the rate-determining step. In contrast Tafel slopes of ~120 mV per decade imply that the Volmer reaction (Equation 3.5) is the rate-determining step due to poor hydrogen adsorption. This is expected for the high contact resistance values due to poor electron injection so that hydrogen adsorption becomes difficult as electrons will not be present at the catalyst active sites, especially in

the case of poor electrical conductance of the catalyst. When electrical coupling is improved, electrons are efficiently injected into the catalyst and hydrogen adsorption can proceed readily.<sup>208</sup>

## **6.4 Sulfur Vacancies as the Active Site for the Hydrogen Evolution Reaction in 2D MoS<sub>2</sub>**

We attribute the catalytic activity of CVD MoS<sub>2</sub> nanosheets to sulfur vacancies. Recent calculations have shown that the basal plane of 2H phase MoS<sub>2</sub> can be activated by increasing the concentration of single S vacancies and the application of tensile strain on the nanosheets. Defect densities as low as ~3% were found to lower the  $\Delta G_H$  from 2 eV down to 0.2 eV. Without any strain, thermos-neutral hydrogen adsorption would require a defect density of ~14%.<sup>172</sup> We used high-angle annular dark-field scanning electron microscopy (HAADF-STEM) to directly image the defects present in our CVD grown MoS<sub>2</sub> samples. Depending the level of contrast on the atomic scale images, we could determine the absence of atoms in the lattice or vacancies. Different types of defects can be observed such as single S vacancies, double S vacancies, Mo vacancies and Mo-S<sub>x</sub> vacancies or antisite defects.<sup>210</sup> A typical STEM image of CVD MoS<sub>2</sub> is shown in Figure 6.4a, with corresponding line scans of the intensity shown in Figure 6.4b. Using the intensity profile along lines L1-L3, we can determine the vacancy type. With Mo intensity set to 100, an intensity of ~50% is assigned to 2 S atoms as in L1, ~30% is assigned to 1 S atom as in L2 and in L3 an intensity under 10% is an absence of any S atoms. These correspond to the STEM image with an orange circle representing a single sulfur vacancy and a yellow circle representing a double sulfur vacancy. After extensive

analysis MoS<sub>2</sub> basal plane areas of greater than 500 nm<sup>2</sup> using large area STEM images, such as Figure 6.4c, we found that the large majority of the defects consist of single S vacancies with a density of defects of up to ~9%. With a density of defects of 9%, the TOF at 0 V from single-layer MoS<sub>2</sub> reaches 0.2-0.5 s<sup>-1</sup>, in agreement with literature values reported at 0.1-0.15 s<sup>-1</sup>.<sup>172</sup> Thus, our results suggest that by tuning the contact

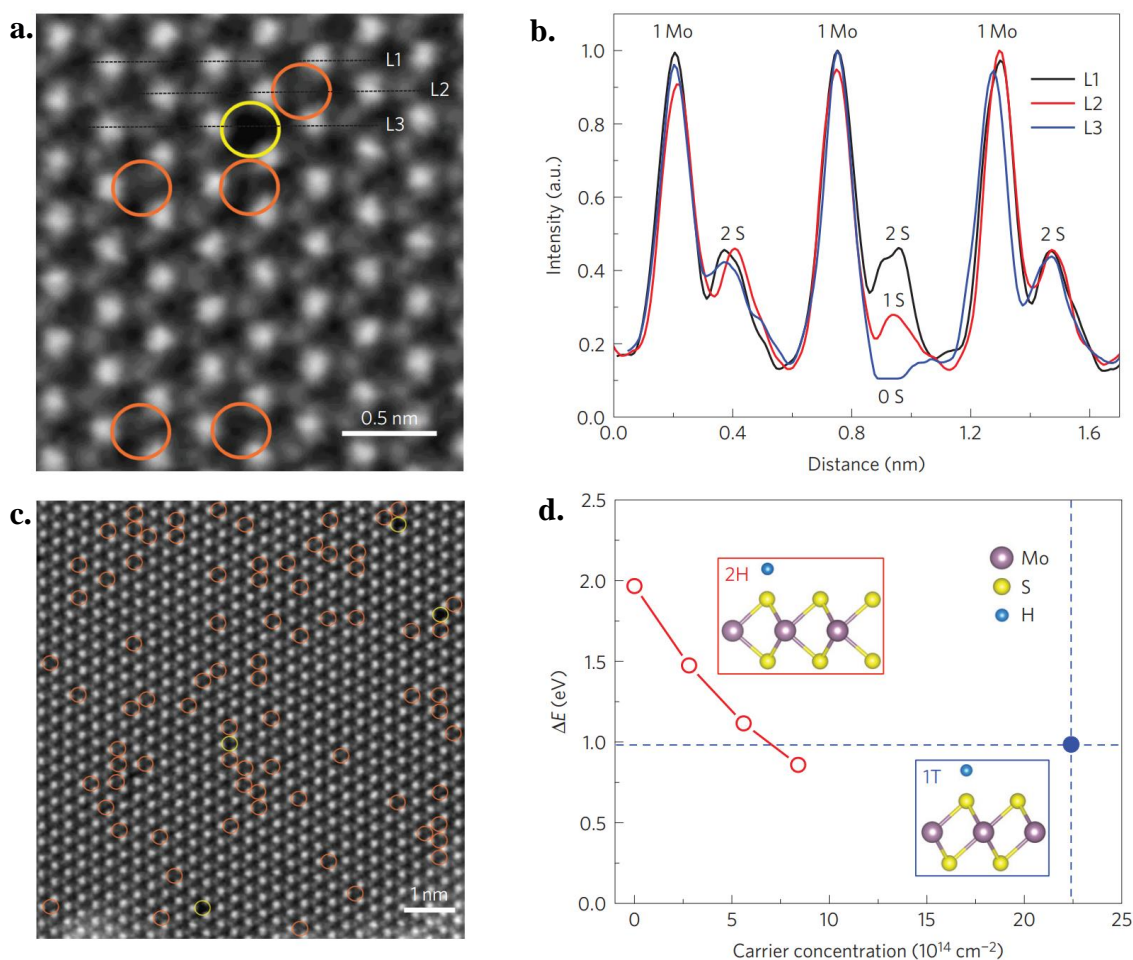


**Figure 6.4:** (a) STEM image of a single-layer CVD-grown MoS<sub>2</sub> nanosheet showing different types of defects: single sulfur vacancy (orange circles) and double sulfur vacancy (yellow circles). (b) Intensity profiles along lines L1-L3. Higher contrast is obtained from the Mo atoms compared to one sulfur atom (~30% of the Mo intensity) and two sulfur atoms (~45% of the Mo intensity). In absence of one sulfur atom (L3), the intensity decreases to <10%. (c) STEM image of a large-area single-layer MoS<sub>2</sub> nanosheet. The vast majority of the defects are formed by single sulfur vacancies. (d) The differential hydrogen adsorption energy ( $\Delta E$ ) in 2H-phase MoS<sub>2</sub> decreases significantly with an increased carrier concentration. When the carrier concentration approaches  $7 \times 10^{14} \text{ cm}^{-2}$ ,  $\Delta E$  in 2H-phase MoS<sub>2</sub> is close to that in the 1T phase.<sup>208</sup>



resistance allows for activation of the basal plane of MoS<sub>2</sub> for the HER at sulfur vacancies.<sup>208</sup>

Sulfur vacancies in MoS<sub>2</sub> act as n-type dopants and will increase the density of states at the Fermi level.<sup>105,176,210</sup> Dopants can influence HER performance in two ways. First excess electrons from dopants will lower the Schottky barrier at the contacts in order to improve charge transfer kinetics between the conducting substrate and the MoS<sub>2</sub> nanosheet. Secondly, additional electrons in the MoS<sub>2</sub> lattice will significantly decrease  $\Delta G_H$ , allowing for the Volmer reaction (Equation 3.50) to proceed more easily. This is shown by our DFT calculations in Figure 6.4d, where the variation of the energy of hydrogen adsorption ( $\Delta E$ ) fluctuates according to the carrier concentration in 2H phase and 1T phase MoS<sub>2</sub>. We calculated values for  $\Delta E$  on the basal plane of 2H phase MoS<sub>2</sub> at doping carrier concentrations of 0 cm<sup>-2</sup>, 2.8 x 10<sup>14</sup> cm<sup>-2</sup>, 5.6 x 10<sup>14</sup> cm<sup>-2</sup> and 8.4 x 10<sup>14</sup> cm<sup>-2</sup>. As the carrier concentration increases, the  $\Delta E$  decreases suggesting that in the 2H phase the basal plane can more readily adsorb hydrogen eventually reaching levels similar to the 1T phase. If a linear interpolation is applied, the  $\Delta E$  for 2H phase MoS<sub>2</sub> reaches levels similar to 1T phase MoS<sub>2</sub> at a carrier concentration of 7.3 x 10<sup>14</sup> cm<sup>-2</sup>, consistent with carrier concentrations calculated with a defect density of 9%.<sup>208</sup>

## 6.5 Conclusions

Through a combination of our electrochemical and STEM measurements and DFT calculations, we can conclude that unsaturated Mo atoms at sulfur vacancies are the active site for the HER in CVD MoS<sub>2</sub>. These unsaturated sites are similar to the metallic edge sites of MoS<sub>2</sub> that have been reported to be highly active.

In this work, we realized electrochemical microcell devices on MoS<sub>2</sub> triangular flakes grown by CVD. Using electron beam lithography we were able to measure the electrocatalytic properties of individual MoS<sub>2</sub> nanosheets as well as discrete areas on the flake, such as the edge or basal plane. In addition, we used organometallic chemistry to selectively transform 2H MoS<sub>2</sub> to the metallic 1T phase in order to fabricate microcells with low resistance contacts. Upon electrochemical testing, we found that after sufficiently decreasing the contact resistance, the basal plane of 2H phase MoS<sub>2</sub> can exhibit excellent catalytic activity, although it has previously been thought to be inactive. The basal plane was found to contain active sites for the HER in the form of sulfur vacancies, but were inaccessible due to high contact resistance. Facilitation of charge injection from the substrate to the catalyst is crucial for utilization of measuring the intrinsic catalytic properties of the 2H basal plane. High contact resistance acts as a large barrier for electron injection to active sites, and limits the catalytic activity.<sup>208</sup>

## **Chapter 7. Nitrogen doped Microwaved Reduced Graphene Oxide for the Oxygen Reduction Reaction**

### **7.1 High Quality Graphene via Microwave Reduction**

One of the challenges facing commercialization of graphene as a material in everyday consumer electronics, is its high cost and low yield for high quality graphene. One method discussed in Section 2.1 to overcome this challenge is to use solution processed GO which has high yield, but the resultant quality of material poor and not suitable for electronic applications, even after substantial reduction. Recently, our group has used a pulsed microwave reduction method on solution processed GO to make high quality graphene.<sup>211</sup> The synthesis starts using the modified Hummer's method as detailed above to realize GO solutions in water. We prepare the microwave reduced graphene oxide (MWrGO) by first making thin fibers of GO, with diameters of 0.5 mm. The fibers are synthesized using a syringe pump which will inject GO solution, at a concentration of 5.7 mg/mL, into a coagulation bath consisting of 1 wt%  $\text{CaCl}_2$  in 25 vol% ethanol and deionized water. The GO fibers are removed from the coagulation bath and washed in a bath of 50 vol% ethanol and water and in a bath of 100 vol% ethanol. The fibers are suspended in air under tension and allowed to dry for 24 hours. The fibers are cut to a manageable size and undergo a mild thermal reduction by annealing at 300 °C for 1 hour in Ar atmosphere. This mildly reduced GO fibers are placed in a vial that has been purged with Ar. A typical sample prior to microwave reduction is shown in Figure 7.1a. We used microwaves from a conventional microwave oven at 1000 W with 1 or 2s pulses. Digital photos of the process are shown in Figure 7.1b. A bright white arc is

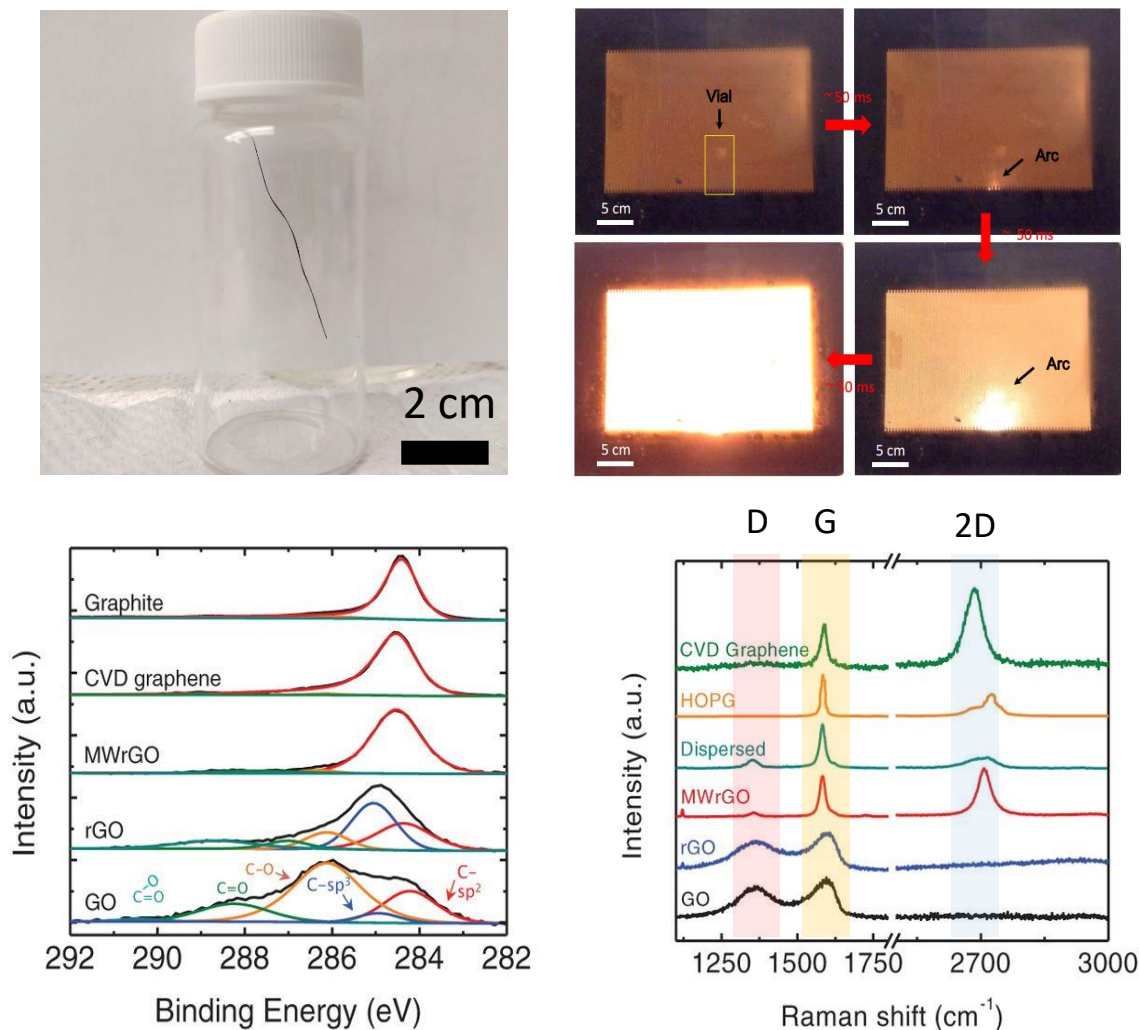


**Figure 7.1:** (a) A digital image of a reduced graphene oxide fiber sample before microwave reduction. The fiber is placed into a vial that has been purged with argon gas and is sealed hand tight (b) Digital images of the microwave reduction process. Pulses of a 1-2 seconds are applied to the vial resulting in an arc flash after a few ms of irradiation (c) C1s spectra obtained from x-ray photoelectron spectroscopy for graphite, CVD graphene, microwaved reduced graphene Oxide (MWrGO), reduced graphene oxide (rGO) and graphene oxide (GO). Each spectra can be deconvoluted to observe oxygen functional groups as well as the composition of the carbon-carbon bonds (d) Raman spectra of MWrGO and other graphene-based samples. The spectra for MWrGO is similar to the spectrum of CVD graphene with a high and symmetrical 2D band and a minimal D band.<sup>211</sup>

formed that typically last 50-100 ms, suggesting the fibers undergo an extremely fast annealing process which rapidly heats up the GO to greater than 1000 °C. No arcs were observed when microwaving GO, confirming that mild annealing of GO is crucial. The resultant MWrGO is allowed to cool and can be removed from the vial.<sup>211</sup>

In order to determine the quality of the MWrGO we used XPS and Raman spectroscopy. The XPS results, shown in Figure 7.1c, shows the C1s scan for graphite, CVD graphene, MWrGO, rGO and GO. A typical sample of GO shows a high degree of oxygen functionalization large amount of oxygen content. Various functional groups such as epoxy, carbonyl and others are present and the  $sp^2$  peak is low, implying a low concentration of  $sp^2$  hybridization. After thermal reduction, the rGO sample shows decreased oxygen functional groups and some restoration of the  $sp^2$  hybridization, however the majority remains  $sp^3$  hybridized. CVD graphene and graphite show almost no oxygenated functional groups. The signal for MWrGO is virtually identical, implying that the surface chemistry is similar to that of CVD graphene, which consists of conjugated  $sp^2$  hybridized carbon. Overall in plane oxygen content was found to be ~4 atomic %, much lower than what is theoretically possible for rGO.<sup>87,211</sup>

The Raman spectra for MWrGO is shown in Figure 7.1d alongside spectra for CVD graphene, HOPG, dispersed graphene, rGO, and GO. Highlighted in orange is the characteristic G band which is found at  $1580\text{ cm}^{-1}$  for all samples and is characteristic of graphitic materials. In CVD graphene is the 2D band, highlighted in blue and found at  $2700\text{ cm}^{-1}$ , which is characteristic of a high degree of order. Finally, highlighted in red is the D band at  $1350\text{ cm}^{-1}$ . The D band is activated by disorder and defects present in the sample and can be seen for GO and rGO. This is expected due to the defects associated with the oxidation process. In contrast, MWrGO, exhibits a clear 2D band; higher in intensity than even HOPG and dispersed graphene. The ratio in intensity between the 2D band and the G band can be used to determine the graphene character. We found that

MWrGO exhibited characteristics much closer to graphene than other carbon materials, with a smaller D band than other GO materials and even liquid dispersed graphene.<sup>211</sup>

Using aberration corrected high resolution transmission electron microscopy, we investigated the local atomic structure. It is well known that thermally reduced GO has a high degree of disorder due to holes and oxygen functional groups. In contrast, MWrGO exhibited a highly ordered atomic structure, suggesting there may be some reorganization of the carbon during the microwave reduction process. We further confirmed the high graphene character of MWrGO by implementing them into field effect transistors as the channel material. The FETs yielded mobility values of over  $1000 \text{ cm}^2 \text{ V}^{-1} \text{ s}^{-1}$ , much greater than what is typically seen for rGO ( $100 - 1000 \text{ cm}^2 \text{ V}^{-1} \text{ s}^{-1}$ ).<sup>211</sup>

With the newly developed microwave reduction, there are many opportunities of using the MW-rGO in further applications. Another recent paper from our group has shown that removal of water by serial solvent treatment improves the ORR activity in acidic medium.<sup>212</sup> We believe that the rapid reduction and strong graphene character in the MWrGO is due to rapid heating of the water that is trapped inside the rGO that quickly reduces the material. By nitrogen doping the MWrGO we sought to apply this material for the ORR and observe how high graphene character may improve the catalytic performance in acidic conditions.

## 7.2 NH<sub>3</sub> Annealing of MWrGO

We utilized ammonia (NH<sub>3</sub>) annealing in order to dope our MWrGO with nitrogen. This is a common method for the introduction of nitrogen into GO and rGO.<sup>102,109</sup> Initially, we followed a recipe used to simultaneously dope with nitrogen and reduce GO. Using a

tube furnace, we placed the MWrGO samples in a clean alumina boat that was inserted into a quartz tube. The alumina boat is partially covered with concave quartz in order to prevent the fibers from moving during annealing. The quartz tube is sealed from the atmosphere with Ar gas going into the inlet and the outlet is connected to a vacuum flask with water. The tube is flushed with Ar gas at 80 sccm for 20 minutes in order to remove oxygen and air. Next, anhydrous  $\text{NH}_3$  gas (Airgas) is introduced to the quartz tube at 100 sccm for 15 minutes, while Ar gas continues to flow. This step is used to uniformly mix the Ar and  $\text{NH}_3$  gases within the tube.  $\text{NH}_3$  gas is highly corrosive so only stainless steel piping and tubing is used within the system. At the outlet we bubble the  $\text{NH}_3$  and Ar gas mixture through water in order to dissolve  $\text{NH}_3$  to form ammonium hydroxide which can be readily neutralized or disposed of as strong basic waste. The furnace temperature is then ramped up to 200 °C in 10 minutes, then to 300 °C in 5 minutes, then slowly ramped to the target temperature of 700 °C. After maintaining the temperature at 700 °C for the desired amount of time, the furnace was allowed to cool naturally to below 100 °C. At this point the  $\text{NH}_3$  gas is turned off to allow for purging of the system. After 15 minutes and the temperature is below 50 °C, the samples are removed from the furnace. We first annealed our samples for 10 minutes at 700 °C, however only GO and rGO showed any incorporation of nitrogen. In order to increase the amount of nitrogen being doped into the sample, we varied the annealing time from 0.5 – 8 hours. After annealing in  $\text{NH}_3$ , the samples are removed from the tube furnace, termed N-MWrGO

### **7.3 Physical Characterization of N-MWrGO**

In order to determine the quality of N-MWrGO we first used Raman spectroscopy. Using a 514 nm excitation wavelength, the Raman spectra for each type of MWrGO was

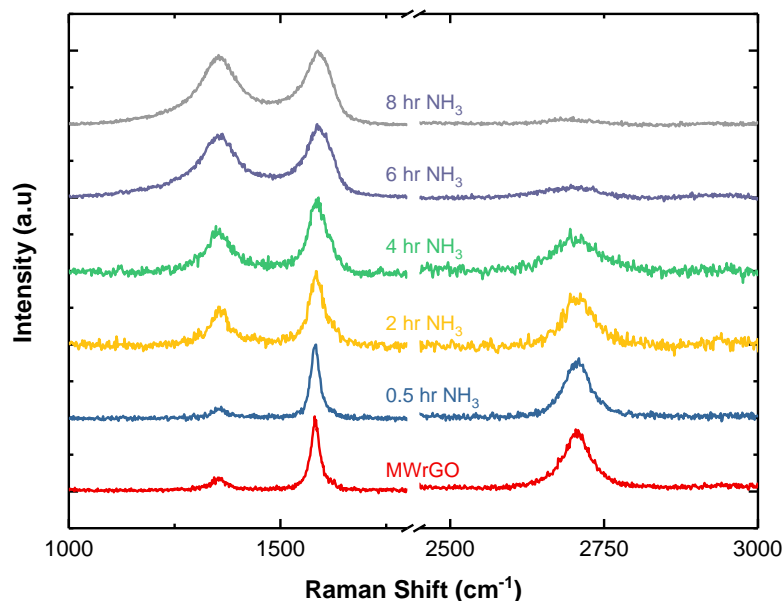


**Figure 7.2:** Raman spectra obtained on MWrGO after annealing at 700 °C in ammonia ( $\text{NH}_3$ ) gas for differing lengths of time. As annealing time increases the 2D peak of MWrGO continually decrease while the D peak increases, suggesting the introduction of defects and disorder as nitrogen is incorporated into the MWrGO lattice

collected and is shown Figure 7.2a, according to the length of time the sample was annealed in  $\text{NH}_3$ . A typical spectrum for MWrGO is shown as a reference, and each of the spectra was normalized to the G band. Each of the characteristic bands for graphene materials undergoes a change as the  $\text{NH}_3$  annealing time increases. The 2D band that is typically found in CVD grown graphene can be found at  $\sim 2700 \text{ cm}^{-1}$  and its intensity ( $I_{2D}$ ) can be used to determine the level of graphene character and order. As annealing time increases  $I_{2D}$  becomes broader and decreases in intensity. At the 4 hour point, it has decreased by about half until nearly disappearing after 8 hours. This implies that the N-MWrGO is decreasing in graphene character as more disorder is introduced by  $\text{NH}_3$  annealing. This is in agreement with the rise of the D band which can be found at  $\sim 1350 \text{ cm}^{-1}$ . Initially, MWrGO has a very small D band; indicative of the highly ordered atomic structure. As the annealing time increases, the D band intensity ( $I_D$ ) increases when at 8



hours,  $I_D$  is nearly equal in intensity of the G band ( $I_G$ ) as defects and disorder have been introduced into the MWrGO. Finally, the G band, which is at  $\sim 1582\text{ cm}^{-1}$ , broadens as annealing time increases, again indicating increasing disorder and defects. In addition, there is a slight upshift in the G band which can indicate atomic insertions into the lattice of graphene.<sup>104,149,150</sup> A slight shoulder at  $\sim 1620\text{ cm}^{-1}$  can be seen in the spectra for the samples annealed for 2 and 4 hours. This shoulder can be assigned to the D' band of graphene materials, which is also associated with defects and is seen in nitrogen doped graphene.<sup>109,213</sup> The overall trends can be summarized by examining the ratio  $I_{2D}/I_G$  as initially it is 0.85 and decreases to 0.07 as  $\text{NH}_3$  annealing time increases as disorder in the MWrGO lattice increases.

We next used XPS to examine the carbon and oxygen content of N-MWrGO as well as confirm that nitrogen has been doped into MWrGO and the bonding configuration. Our XPS results are summarized in Figure 7.3a,b for the C1s and N1s scan respectively, with increasing annealing temperature. MWrGO is included as a reference. The C1s scan for MWrGO shows high concentration of  $\text{sp}^2$  hybridized carbon at  $\sim 284.5\text{ eV}$  with little oxygen functionalization. As the  $\text{NH}_3$  annealing temperature increases, there is a slight increase in the concentration of  $\text{sp}^3$  hybridization, which can be found at  $\sim 285\text{ eV}$ , coupled with corresponding decrease in  $\text{sp}^2$  hybridization. The increase in  $\text{sp}^3$  hybridization suggests that some carbon atoms are being removed from the graphene lattice. This is in agreement with the Raman data, as we are creating defects during the  $\text{NH}_3$  annealing. However, even for the most defective samples, those annealed for 8 hours, still shows a majority of  $\text{sp}^2$  hybridization with little oxygen functionalization. This suggests that the disorder and defects seen in the Raman spectra come solely from

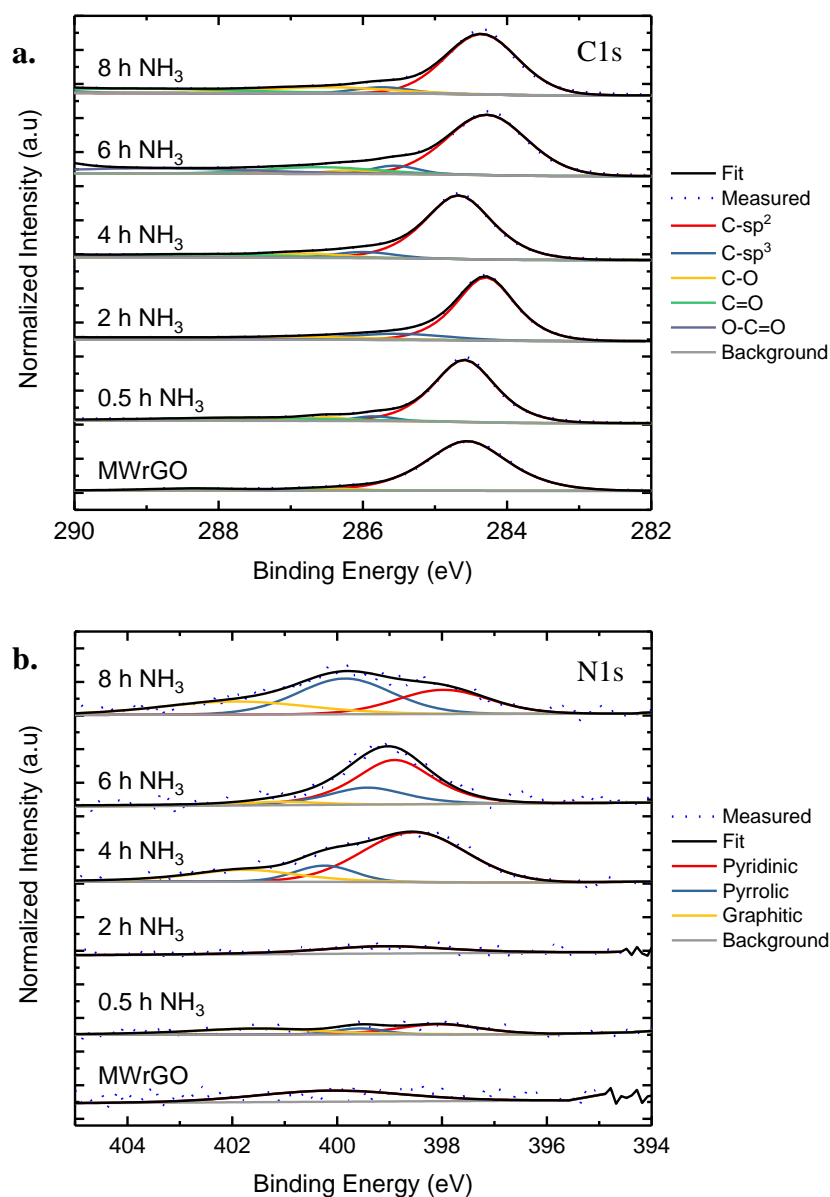


**Figure 7.3:** (a) C1s and (b) N1s spectra obtained from XPS for MWrGO after annealing at 700 °C in ammonia (NH<sub>3</sub>) gas at different lengths of time. The C1s spectra can be deconvoluted to determine the carbon composition as well as the oxygen functional group content. The C1s shows very little oxidation as annealing time increases with a slight increase in sp<sup>3</sup> hybridized carbon concentration. This implies that the defects can mostly be attributed to nitrogen incorporation. The N1s spectra can be deconvoluted into the three main nitrogen bonding configurations. Initially no nitrogen is found, but after 4 hours we see a clear distinct nitrogen peak

nitrogen that has been introduced into the N-MWrGO sheets. To quantify the concentration of nitrogen that has been doped into N-MWrGO, we can follow the

evolution of the nitrogen peak in the N1s scan. MWrGO, as expected, shows no nitrogen. At 0.5 and 2 hours, although we attempted to deconvolute the spectra, it is difficult to confirm the presence of nitrogen. We only started to see appreciable nitrogen after 4 hours of  $\text{NH}_3$  annealing, where a distinct peak is present. We can deconvolute the peak in order to determine the concentration of the different nitrogen binding configurations and found that the pyridinic configuration dominated. As the annealing time continues to increase the relative concentration of each configuration shifts to more pyrrolic.

We calculated the total nitrogen content as a percentage of the carbon and nitrogen content as well as concentration of each configuration as a percentage of total carbon and nitrogen content. The evolution of the nitrogen content over  $\text{NH}_3$  annealing time is shown

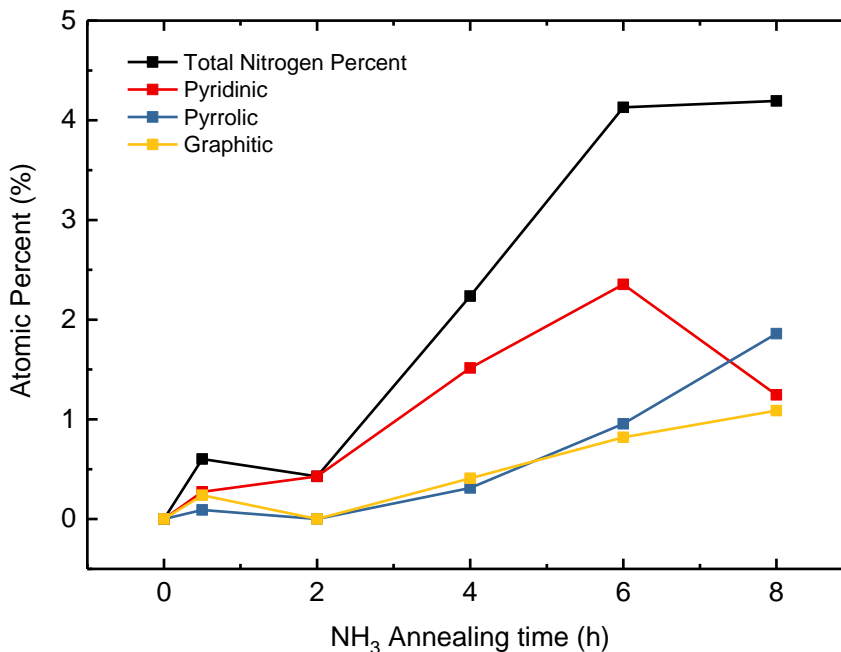


**Figure 7.4:** Evolution of the total nitrogen content and each of the nitrogen bonding configurations by atomic percent with increasing annealing time in ammonia ( $\text{NH}_3$ ) gas. Initially, very little nitrogen content is found until after 4 hours and continues to increase. At 4 and 6 hours of annealing time, the pyridinic nitrogen bonding configuration dominates until it decreases at 8 hours and the pyrrolic configuration overtakes it.

in Figure 7.4. As we expect from the XPS spectra, the total nitrogen content increases as annealing time increases. It does appear to saturate after 6 hours, with only a small increase after an additional 2 hours. In addition, the pyridinic configuration dominates the N-MWrGO reaching over 2 %; until after 6 hours, the pyrrolic configuration has begun to overtake the pyridinic configuration. The structure of the pyridinic and pyrrolic configurations are similar. They both occur at the edge, however pyridinic is in a six membered ring while pyrrolic forms a five membered ring. It is possible that as annealing time continues to increase, more carbon is being removed at the edge during the doping process due to increasing defects. This could result in the conversion of atoms in the pyridinic configuration from shifting to the pyrrolic configuration as more carbon atoms are being driven off. The graphitic configuration remains low, although slowly increasing as annealing time increases. Doping nitrogen into the graphitic configuration in graphene tends to be more difficult as nitrogen atoms have to break into the inert basal plane.<sup>102,213</sup> Due to the high graphene character of MWrGO, it is possible this may be preventing the formation of nitrogen doping in the graphitic configuration until a substantial concentration of defects has been created.

## 7.4 Preparation of N-MWrGO Ink for Electrocatalysis

The fiber form of N-MWrGO lends itself well for characterization using Raman and XPS. However, due to their brittle nature, it is difficult to use a single fiber or even a few fibers in electrochemical setups. We made some efforts towards using  $\text{NH}_3$  annealed individual free standing fibers, however upon introduction to the electrolyte they would quickly bend and fracture where the fiber was mounted. To circumvent these issues, we

developed the following procedure to make inks out of N-MWrGO that allow for easy dropcasting and electrocatalytic testing.

A collection of 20 to 30 rGO fibers under microwave reduction where the total microwaving time is no less than 2 minutes. The MWrGO then undergoes the  $\text{NH}_3$  annealing treatment to make N-MWrGO. The brittle N-MWrGO are placed into a 20 mL scintillation vial. We add 5-10 mL of 100% ethanol to the vial and sonicate for at least 1 hour. Additional sonication was sometimes done in order to ensure the fibers have been sufficiently broken apart. It is typical for the N-MWrGO to precipitate at the bottom of the vial after 30 minutes, resulting in a mostly clear ethanol supernatant. The supernatant is removed using a pipette, with extra care taken to prevent perturbation of the N-MWrGO layer. Excess ethanol is allowed to evaporate in a fume hood until the total volume left is under 2 mL. This concentrated N-MWrGO is placed into a 2 mL microcentrifuge tube that has been pre-weighed. The remaining ethanol is then allowed to



**Figure 7.5:** Digital image of the as-prepared N-MWrGO ink within a microcentrifuge tube

completely evaporate in a fume hood. After 48 hours, the microcentrifuge tube and dried powder is weighed in order to get the mass of electrocatalyst. Finally, the ink is prepared using a concentration of 4.2 mg/mL in ethanol:water with the ratio of 80:20. To disperse the N-MW<sub>r</sub>GO ink, the ink is sonicated for 30 minutes. Nafion is added to the ink at a concentration of 2  $\mu$ L of 5 wt.% Nafion (Sigma Aldrich), which is sonicated for a final 30 minutes. Spectroscopy measurements were performed both on a film prepared by dropcasted ink and the as-prepared N-MW<sub>r</sub>GO fiber with no differences found between the samples. A digital image of the prepared ink for N-MW<sub>r</sub>GO after 0.5 hours of NH<sub>3</sub> annealing is shown in Figure 7.5

We observed the morphology differences of MW<sub>r</sub>GO fibers and dispersed N-MW<sub>r</sub>GO using SEM as shown in Figure 7.6a,b. A cross sectional image of the MW<sub>r</sub>GO fibers is shown in Figure 7.6a, as viewed down the length of the fiber. The fibers show a porous structure with visible voids at the edge that seem to run through the length of the fiber. The morphology at the surface of the fiber is consistently flakey with some porosity. The size of the pores varies greatly from 2  $\mu$ m to 15  $\mu$ m. The dispersed films have not retained their fibrous form, and instead form a pockmarked film with uniform 2 to 3  $\mu$ m

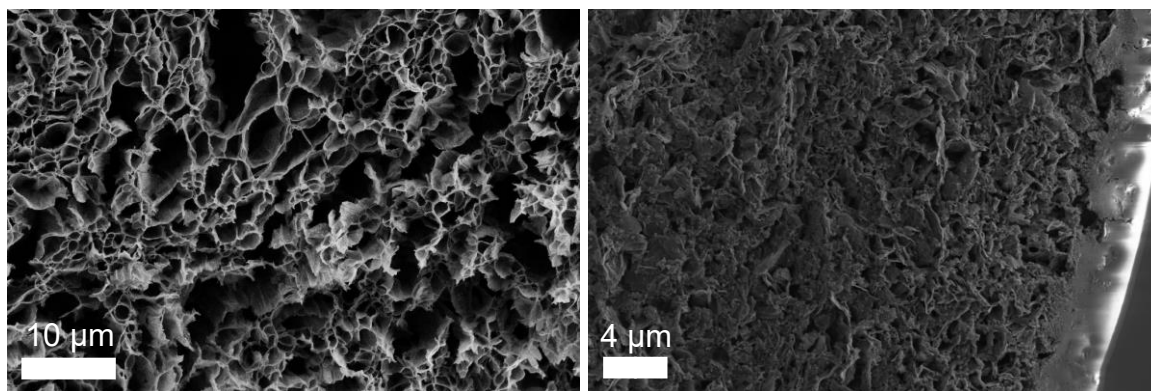


**Figure 7.6:** SEM images of a (a) MW<sub>r</sub>GO fiber as viewed down the length of the fiber and a (b) dropcasted thin film from the ink prepared from N-MW<sub>r</sub>GO. The fiber shows a very porous structure with large voids spread out through the structure. The dropcasted thin film has not retained its fibrous nature, instead forming a thin pockmarked film.

pockets. As the fibers are sonicated, they lose the porous structure as the sheets are broken apart. After dropcasting, the broken up sheets recondense into a thin film as shown in Figure 7.6b. No difference in morphology was noted between MWrGO dispersed or N-MWrGO dispersed films, suggesting no major differences in surface area exposed to the electrolyte.

## 7.5 Electrocatalytic Performance for the ORR of N-MWrGO

After confirming that our  $\text{NH}_3$  annealing process had successfully doped MWrGO with nitrogen, we investigated the electrocatalytic performance for the ORR of N-MWrGO. First, we studied the static ORR behavior of N-MWrGO using CV. We prepare the electrocatalyst by dropcasting N-MWrGO ink on a standard glassy carbon electrode (GCE) with a diameter of 3 mm. The catalyst loading on the electrode is  $0.3 \text{ mg/cm}^2$ . A carbon rod serves as the counter electrode and a saturated calomel electrode (SCE) or saturated Ag/AgCl was used as the reference electrode. Our static ORR measurements were performed using a Multistat 1480 potentiostat from Solartron Group in 0.5 M  $\text{H}_2\text{SO}_4$  at a scan rate of 10 mV/s. When studying ORR, it is best to measure the electrocatalytic performance in nitrogen ( $\text{N}_2$ ) or argon (Ar) and oxygen ( $\text{O}_2$ ) gas saturated electrolyte. The purpose of saturating the electrolyte with  $\text{N}_2$  gas is to remove any oxygen that is dissolved into the electrolyte from air; whereas we saturate the electrolyte with  $\text{O}_2$  gas in order to ensure that there is reactant present for the ORR to occur. Saturation was ensured by purging with each respective gas for 1 hour. This practice also confirms that any current we measure in  $\text{O}_2$  saturated electrolyte is truly coming from a reaction with ORR as opposed to a side reaction. This can be seen in Figure 7.7a, which contains cyclic

voltammograms for MWrGO and N-MWrGO after 4 hours of  $\text{NH}_3$  annealing. In  $\text{N}_2$  saturated electrolyte, no peaks are found for either sample and the current density is

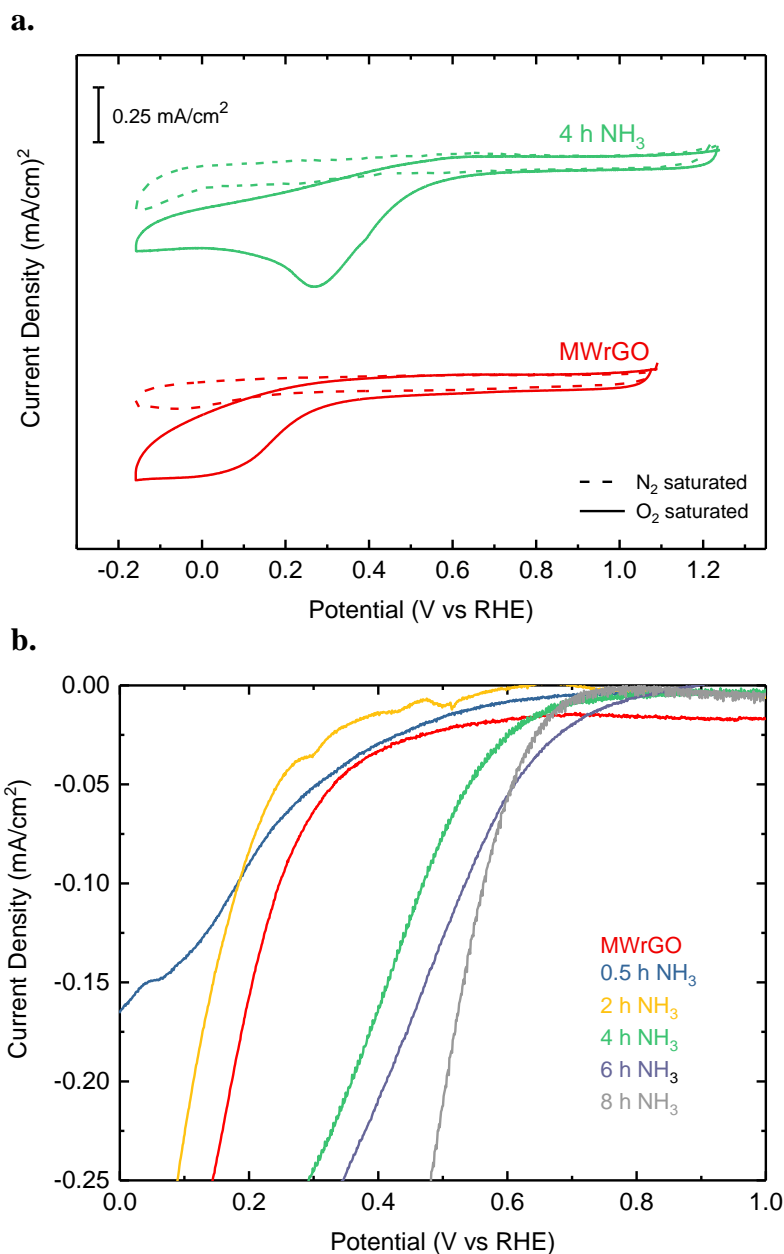


**Figure 7.7:** (a) Cyclic voltammograms for MWrGO and MWrGO that had been annealed in  $\text{NH}_3$  for 4 hours. Voltammograms are shown for  $\text{N}_2$  and  $\text{O}_2$  gas saturated 0.5 M  $\text{H}_2\text{SO}_4$  electrolyte. No peaks in  $\text{N}_2$  gas saturated electrolyte show any increase in current, suggesting that the reaction occurring is the oxygen reduction reaction (ORR) (b) Polarization curves extracted from cyclic voltammograms for MWrGO and samples annealed at increasing annealing time. As annealing time increases, the onset potential shifts further positive, until after 8 hours of annealing; it shifts negative. Measurements were taken at a scan rate of 10 mV/s at a catalyst loading of 0.3 mg/cm<sup>2</sup>



attributed to capacitance. In  $\text{O}_2$  saturated electrolyte, MWrGO has a clear ORR peak indicated by the increase of cathodic current at an onset potential of  $\sim 0.3$  V vs RHE. The N-MWrGO sample also demonstrates that it is catalyzing the ORR with a peak at a more positive onset potential at  $\sim 0.6$  V vs RHE. In addition, the maximum current generated by N-MWrGO after 4 hours of  $\text{NH}_3$  annealing is close to twice that of MWrGO, exhibiting higher performance for the ORR. We performed similar experiments and extracted the polarization curves, as shown in Figure 7.7b, for each of the N-MWrGO samples. Here, the capacitive current generated during the electrochemical test in  $\text{N}_2$  saturated electrolyte has been subtracted from the  $\text{O}_2$  saturated curve. Using MWrGO as a reference, we studied the behavior of the onset potential of N-MWrGO as  $\text{NH}_3$  annealing time increases. Initially, the electrocatalytic performance worsens as at 0.5 hours and 2 hours, the onset potential shifts by a few mV to more negative potentials, thus requiring more energy input to start the ORR. However, at 4 hours there is a dramatic shift to more positive onset potential at  $\sim 0.6$  V vs RHE. From our XPS study, we only see substantial nitrogen doping occurring above 4 hours of  $\text{NH}_3$  annealing. This suggests that nitrogen incorporation is crucial for improving electrocatalytic performance. This can be seen as at 6 hours; the onset potential is further improved to  $\sim 0.8$  V vs RHE. Interestingly, the onset potential decreases back to  $\sim 0.65$  V vs RHE at 8 hours of  $\text{NH}_3$  annealing. This could be related to the decrease of nitrogen in a pyridinic bonding configuration, although the overall nitrogen concentration is still higher at 8 hours. This could be the reason for the sample at 8 hours having a current density greater than the sample at 6 hours at  $\sim 0.6$  V vs RHE.

The current density of static ORR measurements can be used to determine some overall trends, but in order to maximize the current density we used hydrodynamic electrochemical measurements. Hydrodynamic measurements were performed using a Pine Bipotentiostat (Pine Research Instrumentation) and a Pine E6R2 Fixed-Disk RRDE tip was used on a Pine MSR Rotator apparatus. The RRDE is composed of a glassy carbon disk with a diameter of 5.5 mm and an outer ring of platinum and the catalyst was loaded at a concentration of  $0.3 \text{ mg/cm}^2$ . The electrochemical experiments were run in a glass three electrode cell with a graphite rod as the counter electrode and a saturated calomel electrode as the reference electrode in  $\text{N}_2$  or  $\text{O}_2$  gas saturated  $0.5 \text{ M H}_2\text{SO}_4$  electrolyte at a scan rate of  $5 \text{ mV/s}$ . In our collection experiments the electrode is rotating at 800 rpm and swept the voltage applied at the glassy carbon disk while a constant potential of  $1.4 \text{ V vs RHE}$  is applied at the platinum ring to react with any generated  $\text{H}_2\text{O}_2$ .

We measured the ORR activity of our N-MW<sub>r</sub>GO electrocatalysts and the polarization curves are shown in Figure 7.8 along with the absolute current measured at the ring electrode. The polarization curves show a similar overall trend as our static ORR measurements, where activity clearly increases with increasing  $\text{NH}_3$  annealing time as signaled by a positive shift in the onset potential and increase in current density. It's also interesting to note that the sample annealed at 0.5 h of  $\text{NH}_3$  annealing actually had improved performance on the static measurements. This could be due to facilitation of dissolved  $\text{O}_2$  gas having easier access to the catalyst due to the rotation. It is interesting to note that the sample annealed for 2 hours had the worst performance. This is attributed to a high amount of defects in the sample but without much nitrogen being incorporated into

the lattice. This could reduce the conductivity of the sample without introducing any nitrogen, resulting in decreased activity. As in our static samples, we see the best electrocatalytic performance in the sample annealed in  $\text{NH}_3$  for 6 hours, with the best onset potential at  $\sim 0.7$  V vs RHE and a maximum current density of  $\sim 3.5$   $\text{mA}/\text{cm}^2$ . Once again, the sample annealed for 8 hours in a negative shift in the onset potential to  $\sim 0.6$  V vs RHE with decreased current density. This is interesting because the nitrogen content of both samples annealed at 6 and 8 hours have similar nitrogen content, however the 8 hour sample has a lower concentration of the pyridinic nitrogen bonding configuration. The current measured at the platinum ring is directly associated with production of  $\text{H}_2\text{O}_2$  and suggests that the electrocatalyst is undergoing the undesired 2 electron ORR pathway. The ring currents for our electrocatalysts are low for our higher performing catalysts such

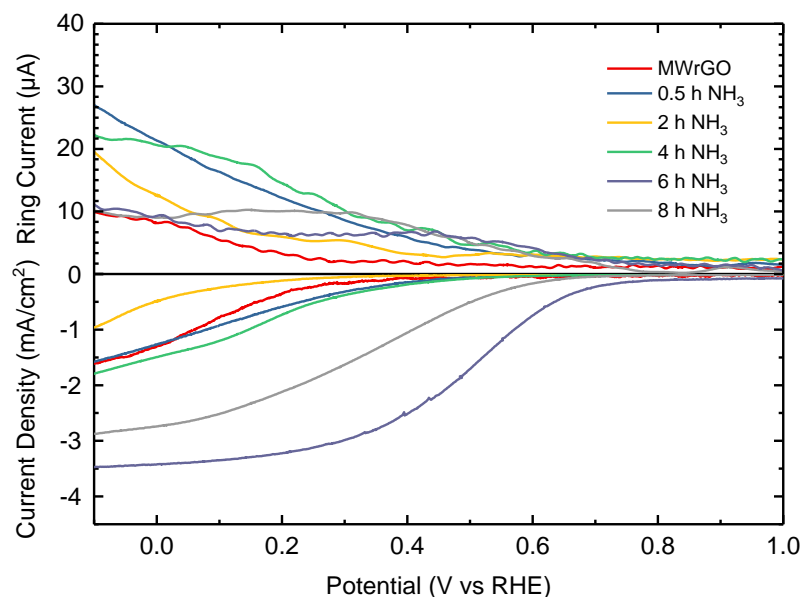


**Figure 7.8:** Hydrodynamic measurements using a rotating ring disk electrode (RRDE) on N-MWrGO at different  $\text{NH}_3$  annealing time. The current density is measured at the disk while the absolute current measured at the ring is shown. Measurements were taken in  $\text{O}_2$  gas saturated 0.5 M  $\text{H}_2\text{SO}_4$  electrolyte at a scan rate of 5  $\text{mV}/\text{s}$  and rotating at 800 rpm. The ring is maintained at a constant potential of 1.4 V vs RHE

as those annealed for 6 and 8 hour. In order to get a clearer picture, we extracted the electron number and calculated the percentage of  $\text{H}_2\text{O}_2$  (% $\text{H}_2\text{O}_2$ ) that is being produced by each catalyst. The results are shown in Figure 7.9. MWrGO exhibits a steady state electron number of  $\sim 3.7$  and  $\text{H}_2\text{O}_2$  production percentage of  $\sim 17\%$  at a potential of 0.1 V vs RHE. Although these results suggest that high performance for the catalyst, the onset potential remains poor. As annealing time increases, we initially see a decrease in electron number to  $<3$  and an increase in the percentage of  $\text{H}_2\text{O}_2$  being produced to greater than  $\sim 55\%$  for N-MWrGO annealed for 2 hours. Neither reaches steady-state prior to -0.1 V vs RHE. As the  $\text{NH}_3$  annealing time continues to increase, we see an improvement of the behavior at the catalyst annealed at 4 hours, although not surpassing the performance of MWrGO. A substantial improvement is seen after 6 hours of annealing where the electron number and percentage of  $\text{H}_2\text{O}_2$  production reach steady-

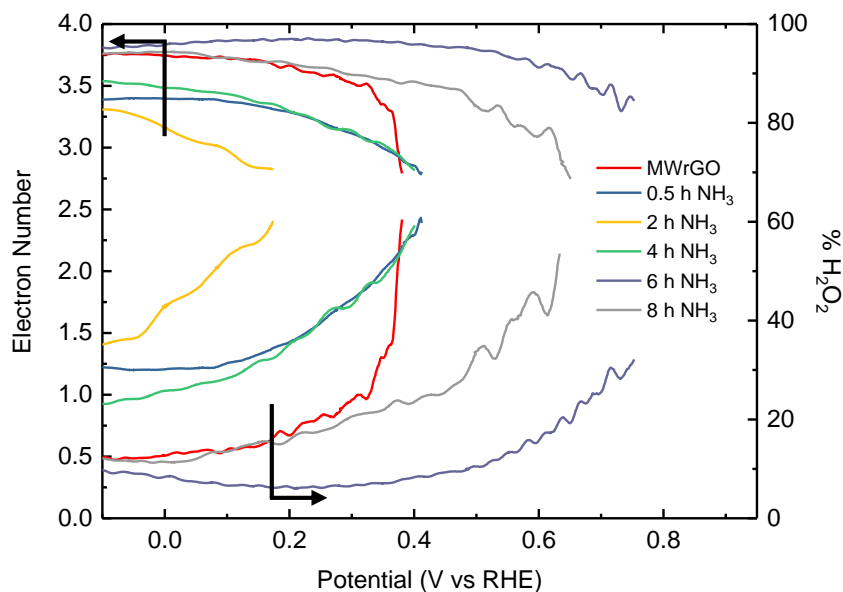


**Figure 7.9:** Electron number (left y-axis) and percentage of  $\text{H}_2\text{O}_2$  production (right y-axis) are calculated from the ratio of the disk current and ring current from the hydrodynamic voltammetry. Values are shown for N-MWrGO at different annealing time.

state values of  $\sim 3.8$  and  $\sim 8\%$ , respectively, at  $\sim 0.4$  V vs RHE. After 8 hours, N-MW<sub>r</sub>GO exhibits a decrease in performance achieving an electron number of  $\sim 3.5$  and H<sub>2</sub>O<sub>2</sub> production percentage of  $\sim 20\%$  at  $\sim 0.4$  V vs RHE. This decrease in performance could be due to the shift in the nitrogen bonding configurations, as the absolute nitrogen atomic percentage of N-MW<sub>r</sub>GO annealed for 6 and 8 hours are relatively close. At 6 hours, the pyridinic nitrogen bonding configuration dominates, whereas at 8 hours it decreases and the pyrrolic configuration dominates and the graphitic and pyridinic configurations are nearly equal. This suggests that the pyridinic nitrogen bonding configuration may have a greater effect on the ORR activity than the absolute nitrogen atomic percentage.

## 7.7 Conclusions

Using our recently developed microwave reduction process, we successfully incorporate nitrogen into MW<sub>r</sub>GO by way of annealing in NH<sub>3</sub> gas. Annealing in NH<sub>3</sub> gas leads to the creation of defects and disorder as shown by our Raman spectra. As the length of the annealing time increases, greater disorder is introduced into the MW<sub>r</sub>GO lattice until the 2D band of MW<sub>r</sub>GO is nearly completely quenched. We found that before nitrogen can incorporate into the MW<sub>r</sub>GO, defects needed to be created within the lattice as our XPS results show no incorporation of nitrogen until 4 hours of continuous NH<sub>3</sub> annealing. From XPS, we also found that the carbon content remains free of oxygen functional groups, suggesting that the incorporated nitrogen is the main contributor to the defects and disorder found in the Raman spectra. The nitrogen atomic percentage continually increased to  $>4\%$  after 8 hours of NH<sub>3</sub> annealing. The nitrogen content from our XPS spectra was broken down to determine the nitrogen bonding configuration from the NH<sub>3</sub>

annealing treatment. The pyridinic configuration was found to dominate the nitrogen content until after 8 hours, it decreases and the pyrrolic configuration overtakes it.

We then investigated the electrocatalytic activity of N-MWrGO samples for the ORR in acidic conditions. Initial static measurements confirmed that the N-MWrGO catalysts were active for the ORR by running experiments in  $N_2$  and  $O_2$  gas saturated electrolyte. Distinctive peaks observed in  $O_2$  gas saturated electrolyte were absent in  $N_2$  gas saturated measurements. We found that there was a clear improvement in the electrocatalytic activity as more nitrogen was incorporated into the N-MWrGO. Hydrodynamic measurements on a RRDE further confirmed this where high activity is observed for N-MWrGO annealed for longer lengths of time. Interestingly, the ORR activity peaks at 6 hours and actually decrease after 8 hours of  $NH_3$  annealing, although they have similar total nitrogen content. This suggests that the pyridinic nitrogen bonding configuration, which dominates in the N-MWrGO sample annealed for 6 hours, may have a greater effect on the activity for the ORR in N-MWrGO catalysts than the absolute nitrogen atomic percentage.

## Chapter 8. Nitrogen-Doped Graphene for the Oxygen

### Reduction Reaction

Our work on CVD grown 2D MoS<sub>2</sub> allowed us to measure the electrocatalytic behavior of discrete areas on a 2D MoS<sub>2</sub> nanosheet giving us insight into the active site for the HER. In addition, our study on N-MWrGO demonstrated that defects are important for incorporating nitrogen when we use NH<sub>3</sub> annealing. NH<sub>3</sub> annealing also seemed to yield graphene based catalysts with predominantly with the pyridinic nitrogen bonding configuration. Once successfully doped, we found that nitrogen does improve the electrocatalytic behavior of graphene based material. In particular, the pyridinic nitrogen bonding configuration seemed to improve the catalytic performance when compared to samples with similar total nitrogen content. Inspired by these two studies, we then doped CVD grown graphene with nitrogen through NH<sub>3</sub> annealing and attempted to measure the electrocatalytic properties.

### 8.1 NH<sub>3</sub> Annealing of Graphene

Similar to N-MWrGO, we annealed CVD graphene in NH<sub>3</sub> using a tube furnace. Previous reports have irradiated with N<sup>+</sup> ions in order to induce defects before annealing in NH<sub>3</sub> for Since CVD graphene is grown on copper substrates, we first transfer the graphene on to SiO<sub>2</sub>/Si substrates. This is done using PMMA as a polymer support for the graphene and ammonium persulfate as a copper etchant. Once the copper is completely etched, the PMMA and graphene are washed in water and transferred to SiO<sub>2</sub>/Si. These samples are placed into a quartz tube. The furnace apparatus is the same as with N-MWrGO along with the temperature scheme of the furnace. Briefly, we flush the tube

with Ar in order to remove any air or moisture for 20 minutes. We then slowly introduce  $\text{NH}_3$  gas and allow the atmosphere within the quartz tube to be uniform. The furnace temperature is then ramped up to 200 °C in 10 minutes, then to 300 °C in 5 minutes, then slowly ramped to the target temperature of 700 °C. For graphene, we only maintained the samples in  $\text{NH}_3$  at the target temperature for 30 minutes. The furnace is then allowed to cool and the nitrogen doped graphene, termed N-graphene, is removed once the  $\text{NH}_3$  line is closed and residual  $\text{NH}_3$  gas is flushed out.

## 8.2 Physical Characterization of N-Graphene

Prior to fabricating the electrical devices, we examined N-graphene using Raman and XPS. Raman spectra for graphene after transferring to  $\text{SiO}_2/\text{Si}$  and N-graphene after annealing in  $\text{NH}_3$  are shown in Figure 8.1. The spectra have been normalized to the

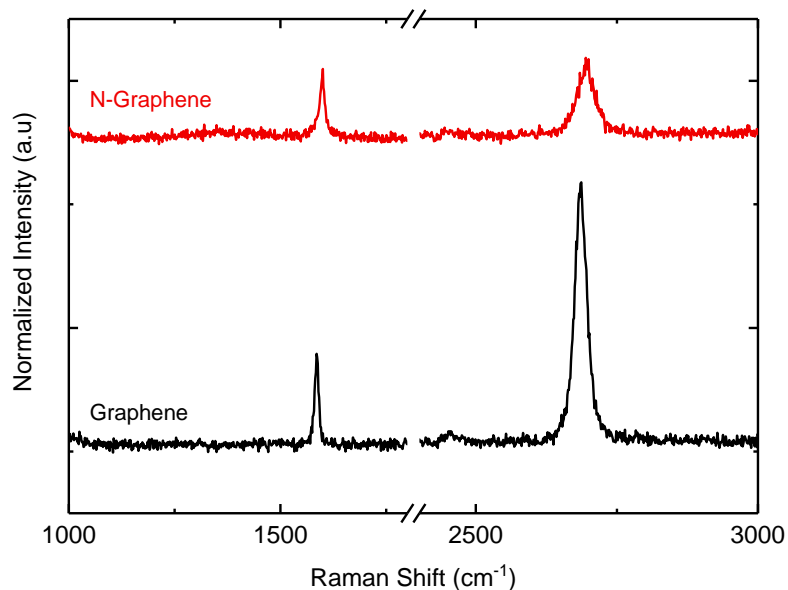


**Figure 8.1:** Raman spectra for CVD graphene and  $\text{NH}_3$  annealed graphene (N-graphene). Decreases in intensity of the 2D peak and a slight increase in the D peak can be seen in the N-graphene sample due to defect and disorder being introduced into the graphene sheet.



silicon peak typically found at  $\sim 520\text{ cm}^{-1}$ . There is a clear decrease in the intensity of the 2D peak after  $\text{NH}_3$  annealing. This suggests a decrease in  $\text{sp}^2$  hybridization and increase in defects. This is attributed to the introduction of foreign atoms, in this case nitrogen, creating disorder in the graphene lattice. This is in agreement with the overall broadening of both the 2D and G peaks. A slight upshift of the G band can also be seen, similar to N-MWGrGO. Directly comparing the  $I_{2D}/I_G$  ratio shows a decrease from 2.76 for pristine graphene to 1.15 for  $\text{NH}_3$  annealed graphene, demonstrating the disorder in the graphene lattice. A very broad and small D peak can be observed after  $\text{NH}_3$  annealing, also suggesting that some of the local symmetry has been disrupted due to defects.<sup>104,150,213</sup>

XPS allows us to study the concentration of  $\text{sp}^2$  and  $\text{sp}^3$  hybridization and directly quantify the concentration of nitrogen that has been incorporated into graphene as well as study the type of nitrogen bonding configurations present, as shown in Figure 8.2a,b respectively. If we observe the C1s scan, we first see a typical spectra for CVD grown graphene with a high concentration of  $\text{sp}^2$  hybridization at 284.5 eV with some  $\text{sp}^3$  hybridization at 285 eV and very little oxygen content at binding energies greater than 285. After annealing in  $\text{NH}_3$ , we see an increase in  $\text{sp}^3$  content due to the breaking up of carbon  $\text{sp}^2$  bonds, creation of defects and introduction of nitrogen into the graphene lattice. We see evidence of nitrogen doping in the N1s scan. The N1s scan for graphene is flat with no signal, indicating no nitrogen is present. In N-graphene there is a clear distinct peak that can be deconvoluted into the three nitrogen bonding configurations, pyridinic, pyrrolic and graphitic. The total nitrogen percentage fluctuated slightly across samples and on average we found with  $\text{NH}_3$  annealing we could achieve nitrogen doping levels of 1-3 %, as calculated using the atomic percent. Through  $\text{NH}_3$  annealing, we have

found that the pyridinic configuration tends to dominate. In our samples of N-graphene, the concentration of pyridinic, pyrrolic and graphitic were found to be ~82 %, 13% and 3%, respectively, as a percentage of the total nitrogen content.

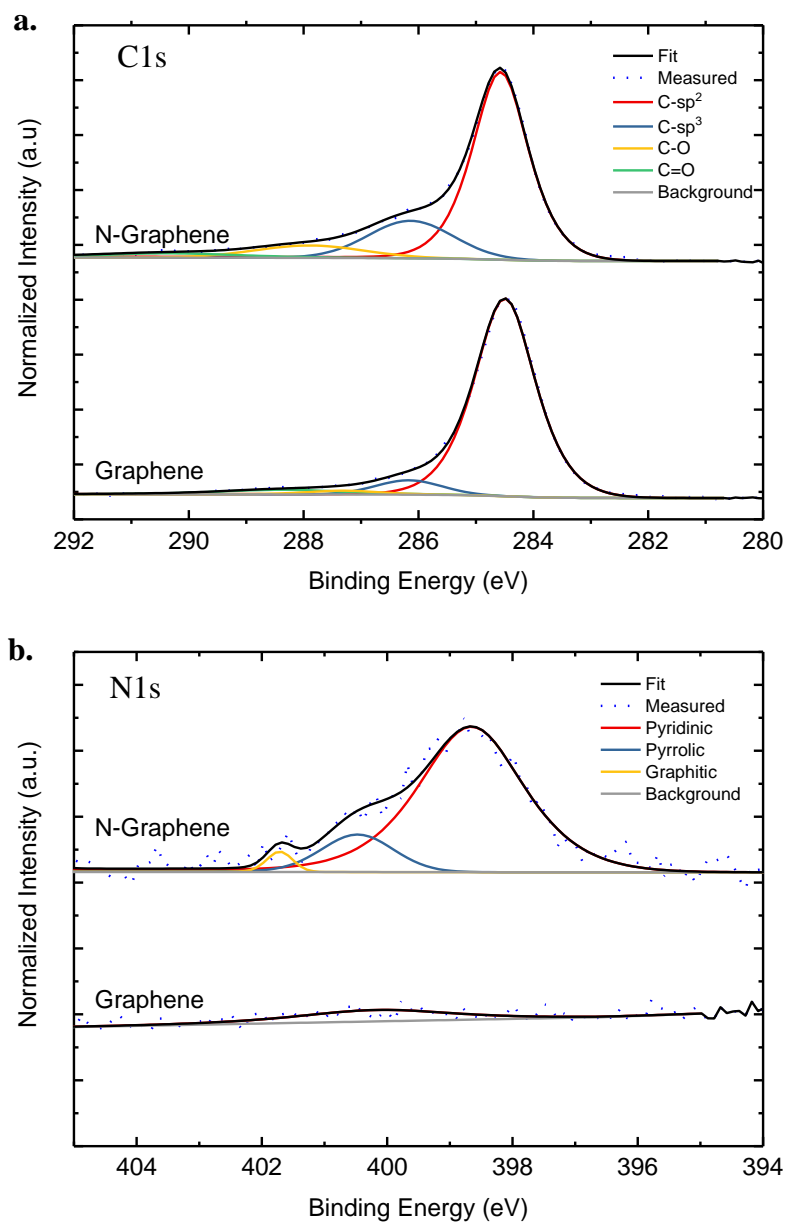


**Figure 8.2:** (a) C1s and (b) N1s spectra obtained from XPS for samples of graphene and N-graphene. The C1s spectra can be deconvoluted into its carbon constituents and oxygen functional groups. There is a clear increase in the concentration of sp<sup>3</sup> hybridized carbon matching well with a large increase in nitrogen content which are likely to introduce disorder and defects into the graphene lattice. The N1s spectra is deconvoluted into the different nitrogen bonding configurations, and the pyridinic configuration was found to dominate.

### 8.3 Patterning of N-graphene

Once we confirmed that we had successfully doped nitrogen in our N-graphene, we moved forward in fabricating electrochemical microcell devices, similar to our work on 2D MoS<sub>2</sub>. Due to the larger lateral dimensions of CVD graphene in comparison so 2D MoS<sub>2</sub>, we could not simply use the same fabrication procedure for devices on N-graphene. We first developed a method to pattern the graphene sheets using a negative electron beam resist, ma-N 2403 (Microchem).

After NH<sub>3</sub> annealing, the N-graphene samples are transferred to SiO<sub>2</sub>/Si substrates that have been pre-patterned with large gold pads and gold alignment marks using

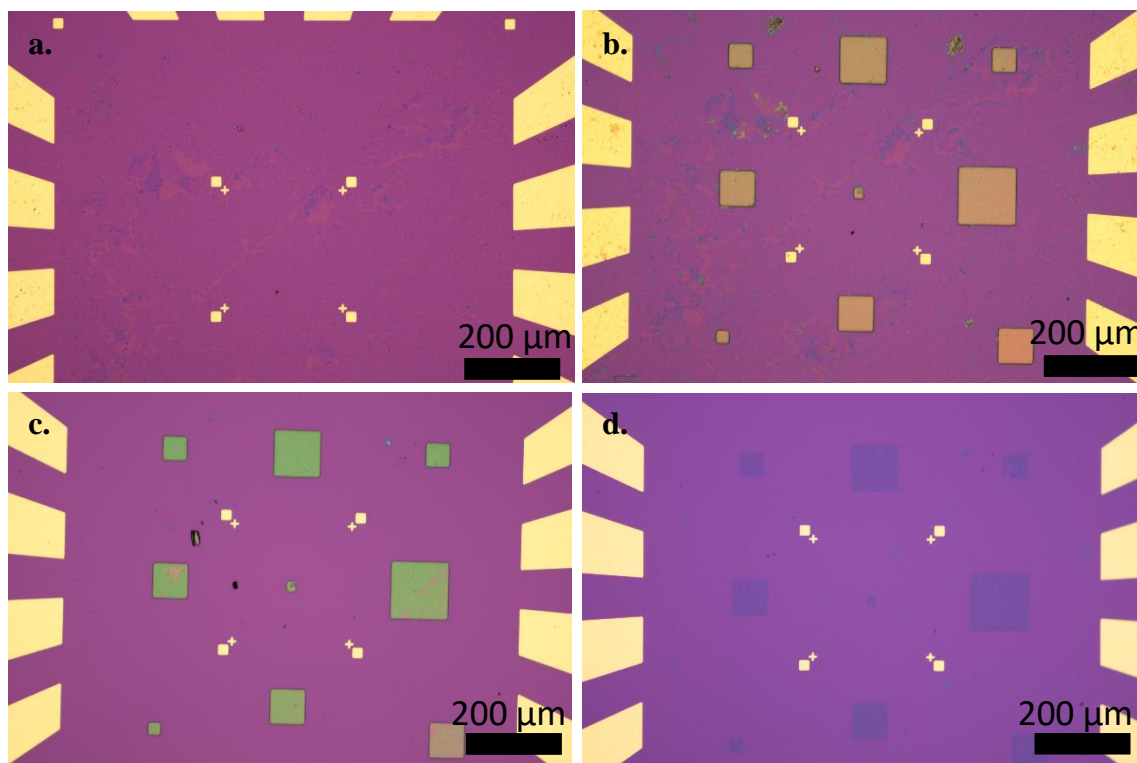


**Figure 8.3:** Optical microscope images of the different steps of the graphene patterning process using a negative electron beam resist. **(a)** The initial sample after N-graphene is transferred to the pre-patterned chip **(b)** The electron beam is exposed onto the sample in an array of squares of differing size **(c)** The sample is exposed to oxygen plasma in order to etch exposed graphene **(d)** After removal of the negative electron beam resist, the patterned N-graphene squares remain on the substrate

photolithography. We then spincoat the ma-N 2403 on top of the substrate at 1500 rpm for 45 seconds which yields a thickness of ~400 nm and cure the polymer at 100 °C for 4 minutes. Our CAD design is a pattern of squares meant to cover the N-graphene in specific areas throughout the working area of our sample. Shown in Figure 8.3a is an image of the N-graphene after transfer to the pre-patterned chip. The underlying SiO<sub>2</sub>/Si substrate can be seen through small tears and holes in the sample. It is easy to see why patterning of the graphene is necessary since the graphene sheet connects gold pads next to each other and on opposing sides. We take this sample and use electron beam lithography to expose the electron beam on top of the areas we wish to save. The exposure uses an area dose of 100  $\mu\text{C}/\text{cm}^2$  with a current of 100 pA. Since ma-N 2403 is a negative beam resist, the electron beam hardens the polymer and after development using ma-D (Microchem), a highly basic aqueous solution, the unexposed areas are washed away. The hardened polymer squares can be seen in Figure 8.3b, with the entire graphene sheet still remaining. Next we etch away the exposed N-graphene using medium powered O<sub>2</sub> plasma until it is removed. After 5 minutes of exposure, only the polymer remains with the protected N-graphene underneath as shown in Figure 8.3c. A layer of the polymer also appears to have etched, as the surface of the polymer appears clean and changes in color. The remaining polymer can be dissolved away in acetone leaving the patterned N-graphene as shown in Figure 8.3d. This process was also used to pattern graphene for comparison. The patterned N-graphene appears clean with few holes and tears as shown in Figure 8.4a. Once the graphene has been patterned, we again use electron beam lithography to put down electrical contacts to the patterned N-graphene and once more to open windows to allow electrochemical contact with the catalyst.

PMMA is used as the electron beam resist in each step. A thicker layer is used when opening windows to prevent the possibility of electrical connections through the polymer. Extra care is taken to open the window only on the graphene catalysts to ensure the electrochemical behavior measured is due to the electrocatalyst. Completed electrochemical devices are shown in Figure 8.4b with different sizes of patterned N-graphene. An individual electrochemical microcell is shown in Figure 8.4c, with the

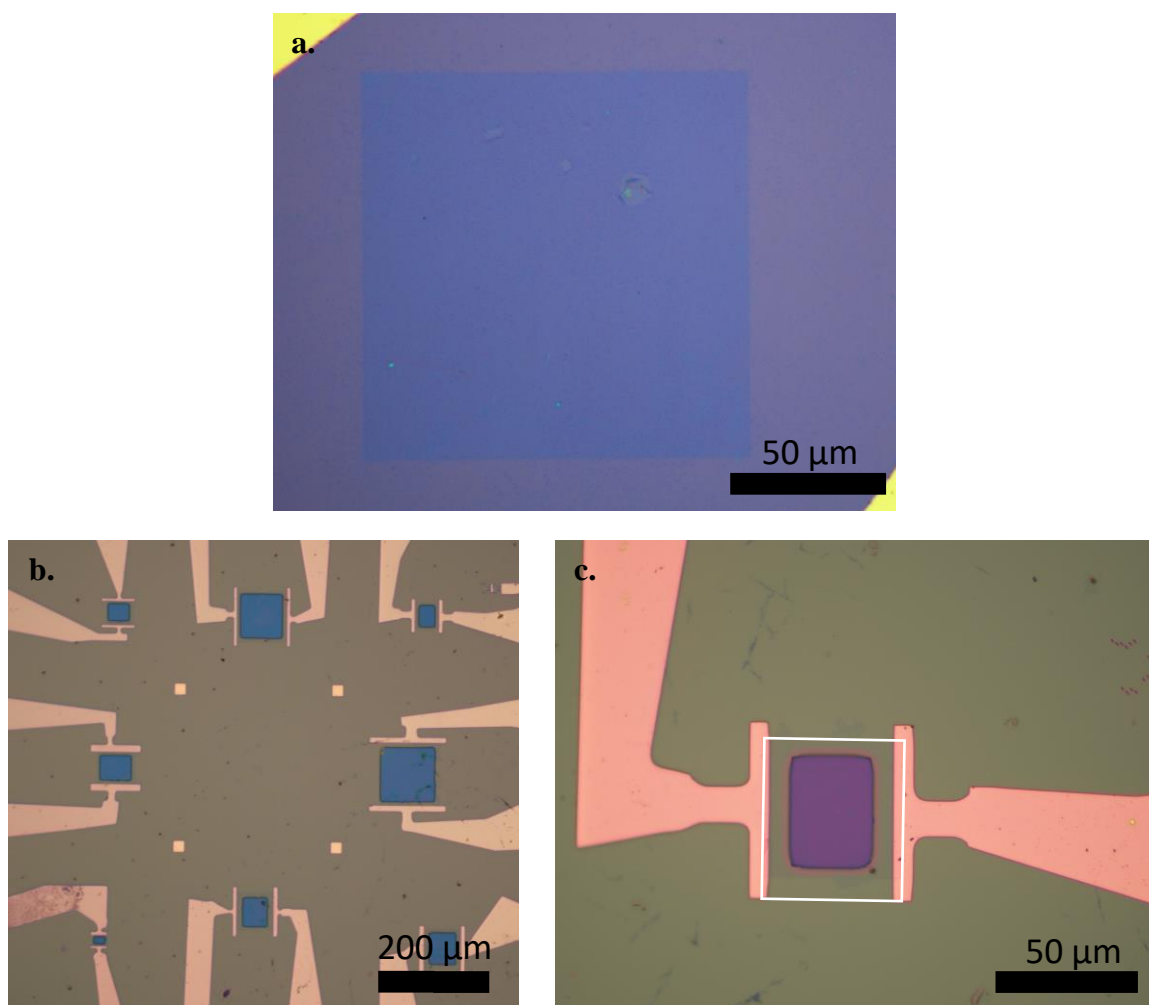


**Figure 8.4:** Optical microscope images of the (a) patterned graphene squares which would be the target of an electrochemical microcell fabrication, (b) multiple devices can be fabricated on one chip and (c) an individual microcell device for N-graphene with the graphene sheet outlined in a white square.

window opened onto the basal plane of the N-graphene sheet which is outlined in a white box for visibility.

## 8.4 Electrocatalytic Performance of N-Graphene

### Electrochemical Microcells

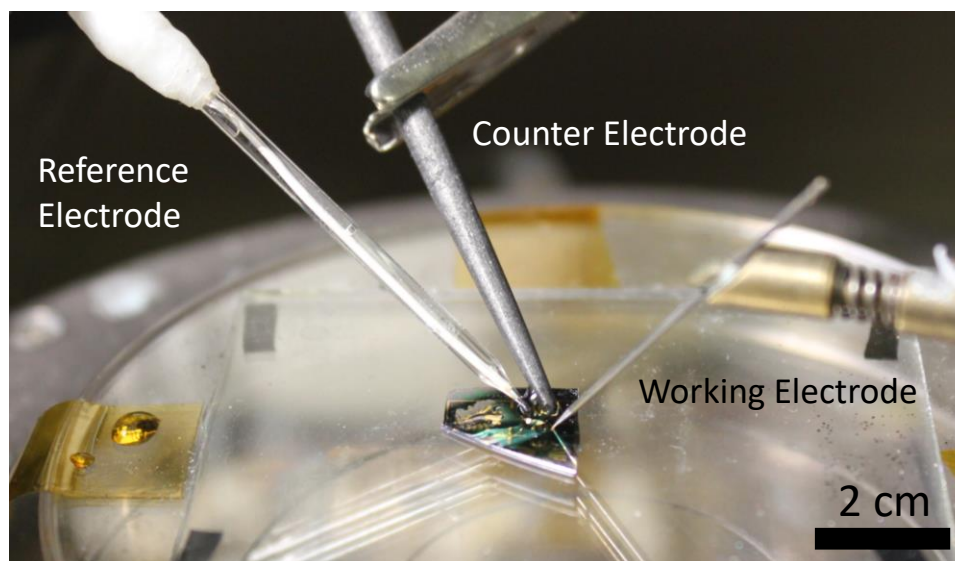


**Figure 8.5:** A digital photograph of the electrochemical microcell set up used for testing N-graphene for the oxygen reduction reaction (ORR). The three electrode cell is composed of a homemade Ag/AgCl reference electrode, graphite or glassy carbon counter electrode and the probe is electrically connected to a N-graphene device.

We measured the electrochemical microcells of N-graphene in a similar manner as the 2D MoS<sub>2</sub> microcells. By probing the gold connected to the N-graphene, the opened window area was used as our working electrode and ranged from 50 to 10,000  $\mu\text{m}^2$ . Similar to the case of 2D MoS<sub>2</sub>, this small area limited our measurement set up. We used a glassy carbon needle as our counter electrode and a homemade Ag/AgCl microelectrode as our reference electrode with 0.5 M H<sub>2</sub>SO<sub>4</sub> as our electrolyte. The homemade reference microelectrode was fabricated using the same procedure as detailed

in Section 5.4. The microcells were measured using a Multistat 1480 potentiostat from Solartron Group. A digital photograph of the set-up is shown in Figure 8.5.

As in the case of N-MW<sub>r</sub>GO, we measured the electrocatalytic activity of graphene and N-graphene using CV in both N<sub>2</sub> and O<sub>2</sub> gas saturated electrolyte. The level of oxygen gas that can be dissolved into 0.5 M H<sub>2</sub>SO<sub>4</sub> is small at  $1.1 \times 10^{-6} \text{ mol/cm}^3$ .<sup>214</sup> In order to ensure that enough reactant was available for the catalyst, 10  $\mu\text{L}$  of electrolyte was used

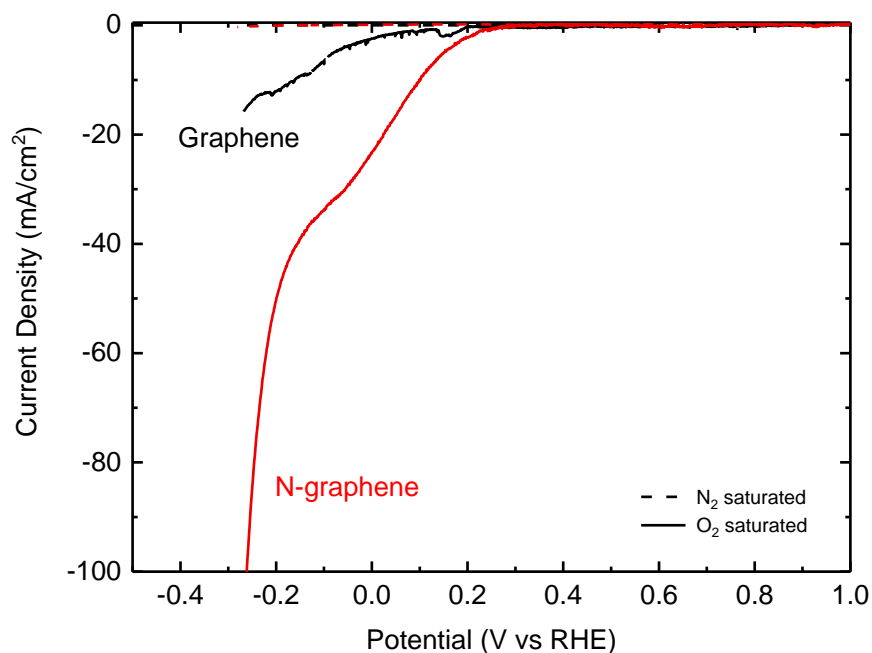


**Figure 8.6:** Polarization curves of graphene (black) and N-graphene (red) in both N<sub>2</sub> (dashed line) and O<sub>2</sub> gas (solid line) saturated 0.5 M H<sub>2</sub>SO<sub>4</sub> electrolyte. Clear deviations from N<sub>2</sub> gas saturated experiments can be seen in the O<sub>2</sub> gas saturated curve, suggesting that the ORR is taking place. Measurements were performed at a scan rate of 10 mV/s

each time and the scan rate set to 10 mV/s. The polarization curves are shown in Figure 8.6 for graphene and N-graphene in both N<sub>2</sub> saturated and O<sub>2</sub> saturated electrolyte. The curves in N<sub>2</sub> saturated electrolyte for both samples show close to zero current density for the entire potential range. This was repeated several using the same 10  $\mu\text{L}$  of electrolyte with no electrochemical peaks. This suggests that atmospheric oxygen is not being

diffused into the electrolyte before any electrochemical tests. In O<sub>2</sub> saturated electrolyte, we see a difference in current density and onset potential. The onset potential of graphene is more negative at ~0.5 V vs RHE while N-graphene has a more positive onset potential of 0.2 V vs RHE. Graphene reaches a current density of -6.6 mA/cm<sup>2</sup> at a potential of -0.1 V vs RHE. N-graphene outperforms graphene reaching a current density of -33.76 mA/cm<sup>2</sup>, a five times increase at the same over potential. There is a clear improvement in the electrocatalytic performance for the ORR in our catalysts after annealing in NH<sub>3</sub>. The poor onset potential observed in both samples can be attributed to the difficulty in doping of the inert basal plane in graphene.<sup>102,215</sup> This can prevent substantial concentrations of nitrogen to be incorporated into the graphene sheet, hindering the electrocatalytic activity. In addition, there was issues with the repeatability of the experiments, as some samples that had been NH<sub>3</sub> annealed showed no activity. We investigated these issues by studying the composition during the fabrication process.

## 8.5 Optimization of Electrochemical Microcells on N-graphene

Initially we used XPS, to confirm the nitrogen content on the completed electrochemical devices. The XPS C1s and N1s spectra for N-graphene before device processing and the finished devices are shown in Figure 8.7a,b respectively. In the C1s spectra, we can see that the concentration of sp<sup>2</sup> hybridization has decreased while the sp<sup>3</sup> hybridization has greatly increased. In addition, there has been an increase in oxygen functional groups such as C-O and O-C=O. This suggests that many defects were created in the graphene sheet and ambient oxygen or oxygen dissolved into the electrolyte has reacted and passivated the defects as it was exposed. The N1s scan shows a clear picture that the



nitrogen that had been doped into the graphene sheet has been removed as the spectra for the completed device shows no nitrogen peak.

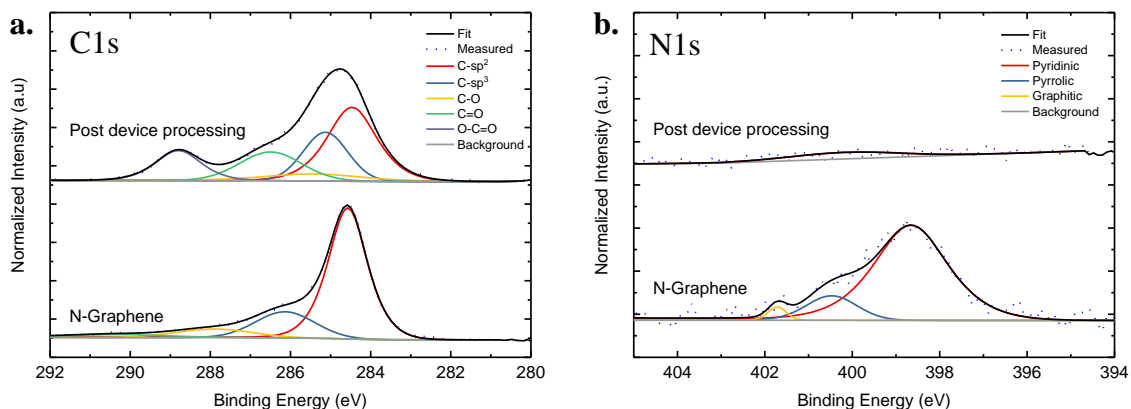


**Figure 8.7:** (a) C1s and (b) N1s spectra obtained from XPS for samples of N-graphene before and after device processing. The C1s spectra shows increased oxygen functional group concentration and sp<sup>3</sup> hybridized carbons suggesting that the sample has become very defective with much of the sp<sup>2</sup> hybridization being destroyed. The N1s spectra shows the complete removal of nitrogen from the sample.

We attempted to troubleshoot the issue and determine where in our fabrication process the nitrogen is being removed. We outlined four key steps in the fabrication process that we determined may be the issue and utilizing XPS, studied the carbon and nitrogen content at each of these steps. As a control, we studied graphene in parallel undergoing the same device processing. Step 1 is directly before spincoating the negative electron beam resist. Next, step 2 is after exposure and development of the electron beam resist. Step 3 follows after the excess N-graphene has been etched away using O<sub>2</sub> plasma. Finally, step 4 is after washing away the ma-N 2403 resist with acetone.

The XPS C1s spectra taken at each step are shown in Figure 8.8a,b for the for graphene and N-graphene, respectively. At step 1 we see the typical C1s spectra for graphene and N-graphene, where graphene has high  $sp^2$  hybridization and N-graphene also has mostly  $sp^2$  hybridization with some defects disrupting it to form some  $sp^3$  hybridization. When looking at step 2, we see an increase in carbonyl functional groups in both samples. This

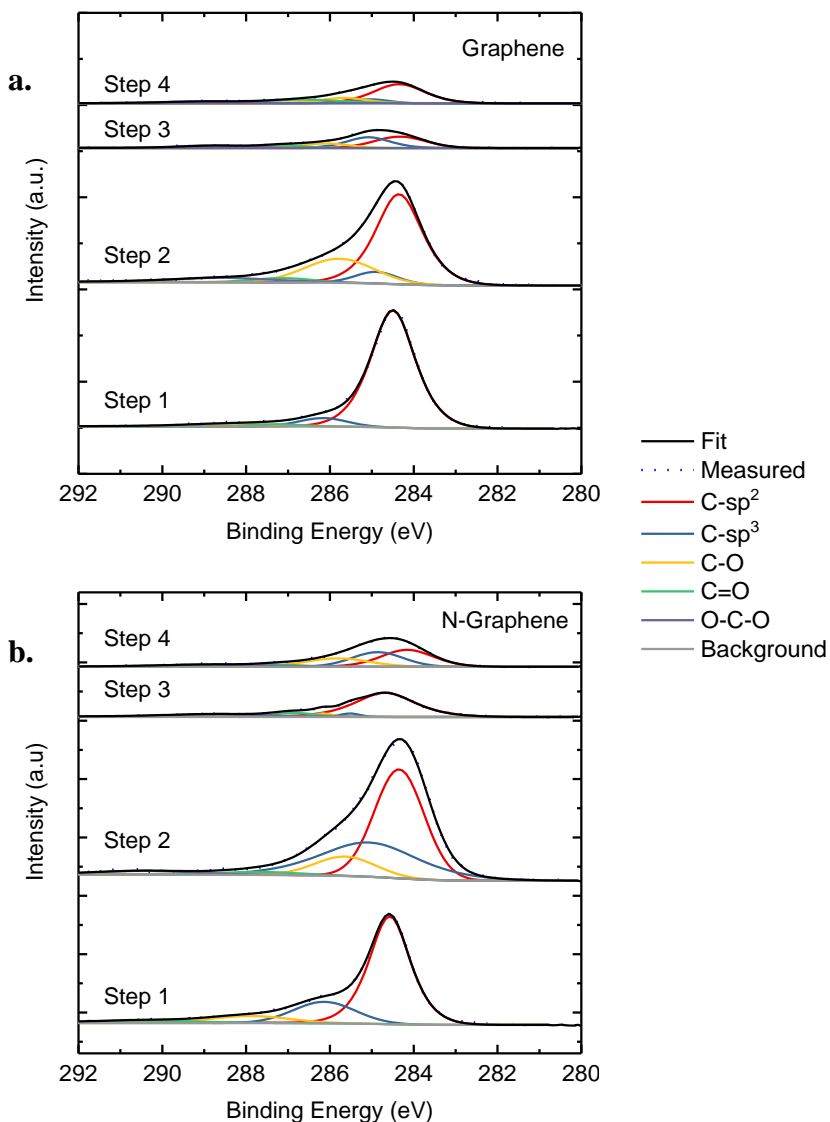


**Figure 8.8:** C1s spectra obtained from XPS for (a) graphene and (b) N-graphene along the negative electron beam resist patterning process. The overall decrease in signal at step 3 is attributed to the etching of graphene material. The spectra show minimal damage for graphene, but substantial damage to the graphene lattice in N-graphene due to the increase in  $sp^3$  hybridization.

can be attributed to the carbon based ma-N 2403 electron beam resist. In step 3, the overall signal for both samples has decreased. This is attributed to the loss of material due to etching. What can be observed is that graphene seems to have increased in  $sp^3$  carbon while N-graphene has decreased. Both samples maintain a dominant concentration of  $sp^2$  hybridization and have had an increase in oxygen functional groups. Finally step 4 shows similar spectra to what was observed in our completed devices. Graphene shows dominant  $sp^2$  carbon with a slight increase in oxygen functional groups, while N-graphene shows nearly equal  $sp^2$  and  $sp^3$  hybridization with a greater increase in oxygen functional groups. We attribute this behavior to the removal of nitrogen that had been previously doped into the N-graphene sheet. As it is removed during the electron beam lithography process, it is likely leaving defects result in increased  $sp^3$  hybridization and leaves room for passivation by oxygen as it reacts to form various functional groups. The XPS N1s spectra confirms the results from C1s spectra as shown in Figure 8.8a,b for graphene and N-graphene. Spectra for graphene is only shown for steps 3 and 4 as no nitrogen had been expected until after step 2. In step 1 of N-graphene, we see a typical N1s spectra for N-graphene. As we proceed to step 2, the intensity of the N1s scan has an overall increase indicating that the nitrogen content has increased. In addition, after deconvolution an additional peak can be seen at  $\sim 403$  eV, which had not previously been seen in N-graphene. For step 3, graphene exhibits a distinct nitrogen peak, when it had not been exposed to  $NH_3$  gas or any other nitrogen dopant. The deconvoluted peak has one peak at  $\sim 402$  eV which appears to match with the deconvoluted peaks from N-graphene at step 2 and 3. Step 4 clearly shows no nitrogen peaks in either sample, as any nitrogen present was removed as the ma-N polymer was dissolved away. These results

suggest that the ma-N resist is somehow participating in a side reaction with the nitrogen that had been doped into the graphene sheet. It seems likely that the electron beam is providing energy for this side reaction. From the XPS results on graphene, we expect

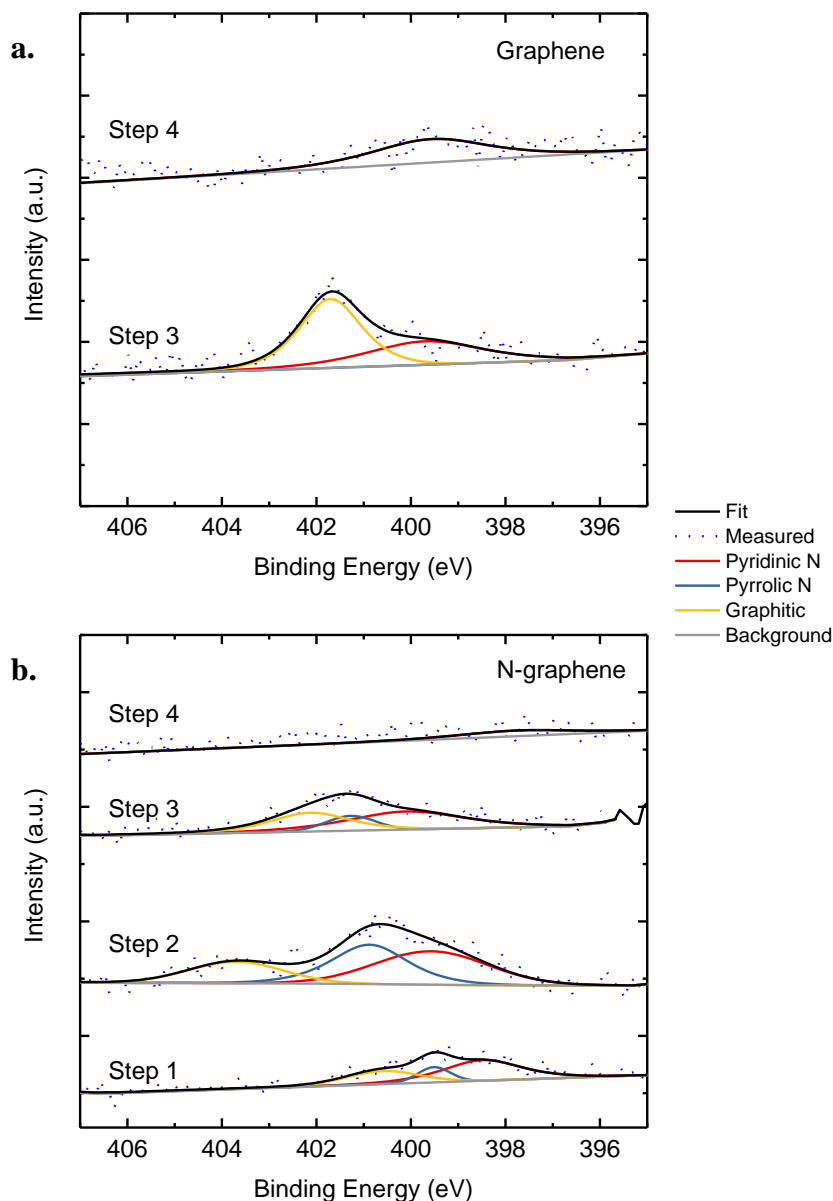


**Figure 8.9:** N1s spectra obtained from XPS for **(a)** graphene and **(b)** N-graphene. The spectra for each shows an increase in nitrogen content after step 2 for N-graphene and the presence of nitrogen in step 3 for graphene. This indicates that the ma-N negative electron beam resist contains nitrogen. Once washed away in step 4, nitrogen is no longer present in either sample

nitrogen to be present in the ma-N polymer itself. When we collected an XPS spectra of just the ma-N resist dropcasted on to SiO<sub>2</sub>/Si, nitrogen was present in the polymer. The N1s spectra has intense peaks indicating C-N bonds are present as well as a distinct peak at ~403 eV, which was found on our graphene and N-graphene samples.

Raman spectra for the graphene and N-graphene sample is shown in Figure 8.10 along with a corresponding spectra taken on the same sample after patterning. The spectra for graphene are mostly unchanged aside for a broadening of the 2D band, suggesting some disorder due to the processing. The graphene sample maintains a  $I_{2D}/I_G$  ratio of ~2.74. In the spectra for N-graphene, a mild increase in the D band can clearly be observed. In addition, the G band and 2D band both downshift due to the loss of the doped nitrogen in the graphene sheet. After patterning, the N-graphene sample experiences a broadening of the 2D band and a slight decrease in the  $I_{2D}/I_G$  ratio from 1.15 to 1.05. This is in

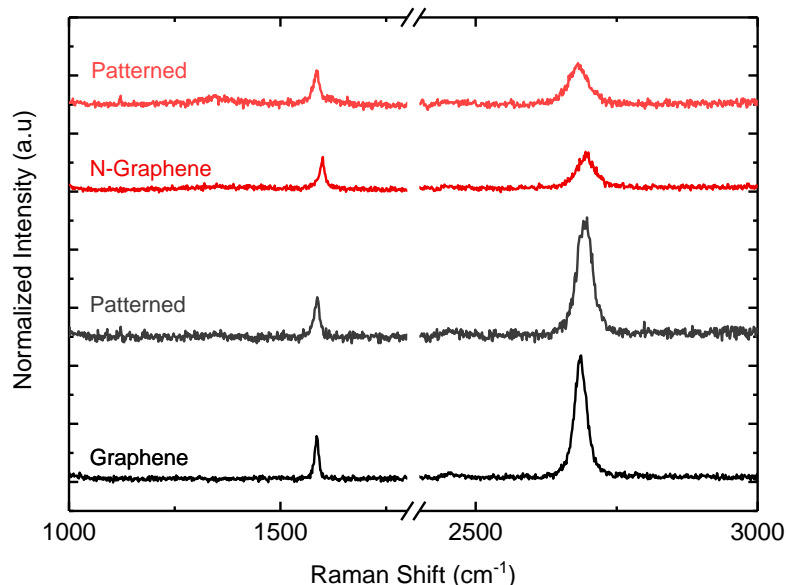


**Figure 8.10:** Raman spectra of graphene and N-graphene before and after being patterned using ma-N 2403 negative electron beam resist

agreement with our XPS results, as these changes indicate the increase of defects and disorder in the graphene sheet.

## **8.6 Maintaining Nitrogen in N-Graphene**

We determined that our issue of losing nitrogen in our completed electrochemical devices was due to the fabrication process involving the use of ma-N 2403 as a negative electron beam resist. In order to preserve the nitrogen content in N-graphene, we pursued two different approaches. From our XPS study, we found that the graphene sample is largely unaffected after patterning. In our first approach we attempted to anneal graphene samples in  $\text{NH}_3$  after patterning. Our motivation behind patterning the N-graphene was to prevent shorts when measuring the electrical properties as the large lateral dimension connected nearby gold pads. In our second approach, we opened windows directly on as transferred N-graphene without any patterning and studied the electrocatalytic properties.

### **8.6.1 Annealing Patterned Graphene in $\text{NH}_3$**

For our first approach, we took a graphene sample and used the negative resist based process detailed above to pattern the graphene. Next, we annealed the same sample on the pre-patterned  $\text{SiO}_2/\text{Si}$  substrate in  $\text{NH}_3$  at 700 °C for 30 minutes, following the typical procedure. Optically, the patterned graphene samples did not look different as shown in Figure 8.11a, however the large gold pads, that are part of the pre-patterned chip, contained several imperfections scattered across the gold surface and were tinted darker. To study the quality and carbon and oxygen content we used Raman and XPS to

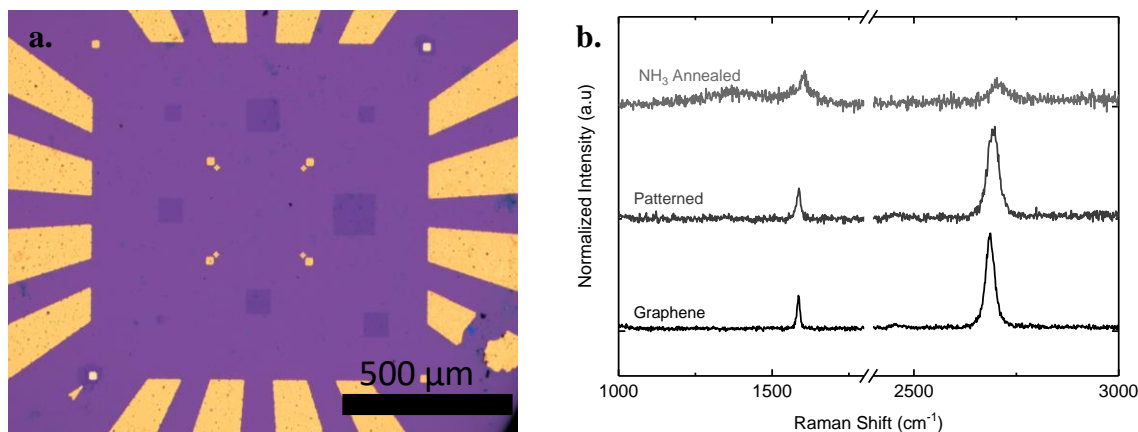


**Figure 8.11:** (a) Optical microscope image of the patterned sample that had undergone a  $\text{NH}_3$  annealing treatment. Imperfections and defects can be seen on the gold pads. (b) Evolution of the Raman spectra after patterning and after undergoing a  $\text{NH}_3$  annealing treatment. The 2D peak decreases in intensity with a slight increase in the D peak after the annealing treatment.

characterize the  $\text{NH}_3$  annealed patterned graphene. Figure 8.11b shows the evolution of the Raman spectra of a graphene sample from pristine to patterned using the negative resist method and finally  $\text{NH}_3$  annealed. We can see the stark contrast after  $\text{NH}_3$  annealing as the 2D band intensity has decrease greatly bringing the  $I_{2D}/I_G$  ratio down to 0.88. This is in agreement with the rise of the D band as defects and disorder have been created in the graphene sheet. A slight upshift in the G band can also be seen, suggesting that some nitrogen has been doped into the sheet. The XPS results are shown in Figure 8.12a,b for the C1s and N1s scan, respectively. The C1s scan shows that the graphene sheet contains a high concentration of oxygen functional groups that we do not typically see in  $\text{NH}_3$  annealed graphene. It is in agreement with the corresponding Raman spectra as this suggests a high degree of disorder due to the oxygen functional groups. Our initial results showed that nitrogen was present in the graphene sample, however the nitrogen concentration was found to be 31%, much greater than expected. In addition, a deconvoluted peak is found at 396 eV which was not observed previously. It can be

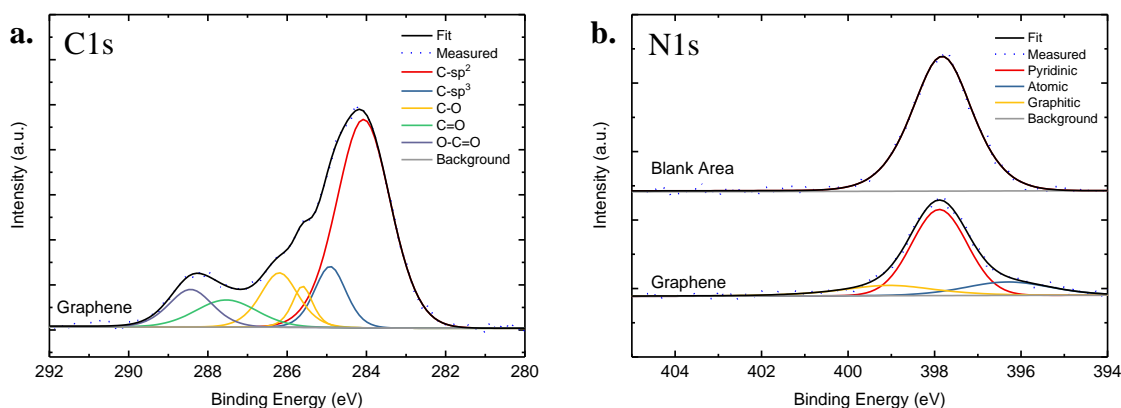


**Figure 8.12:** (a) C1s and (b) N1s spectra obtained from XPS on the graphene sample undergoing NH<sub>3</sub> annealing treatment after patterning. The C1s spectra shows substantial oxygen functional group content. While the N1s spectra does show nitrogen content, a spectrum taken on the same substrate but without any material shows a highly intense nitrogen peak that can be attributed to the formation of silicon nitride.

attributed to an atomic nitrogen bonding configuration on carbon and can be found at the edge or near a dangling bond.<sup>216</sup> This could be due to an excess of nitrogen being adsorbed onto the surface of the graphene sheet and SiO<sub>2</sub> or the formation of a thin layer of silicon nitride at the surface of the oxide layer. In order to confirm this we studied a blank area on the substrate by XPS and found a strong signal for nitrogen as shown in the N1s scan, in fact it is greater in intensity than our graphene sample. This peak can be attributed to silicon nitride, which exhibits a N1s peak at 397.9 eV.<sup>217</sup>

### 8.6.2 Open Windows without Patterning N-Graphene

The second approach involved the direct opening of electrochemical windows on as transferred N-graphene without any patterning. While this may allow access to electrocatalytic measurements, we will be unable to make electrical measurements on the same device.



Once the N-graphene is transferred we confirmed the presence of nitrogen in the sample through XPS. The N1s scan, as shown in Figure 8.13a, shows the presence of nitrogen within the graphene sheet and with the breakdown of nitrogen bonding configurations.

From the XPS we determined this sample to contain 3 % nitrogen as a percentage of total

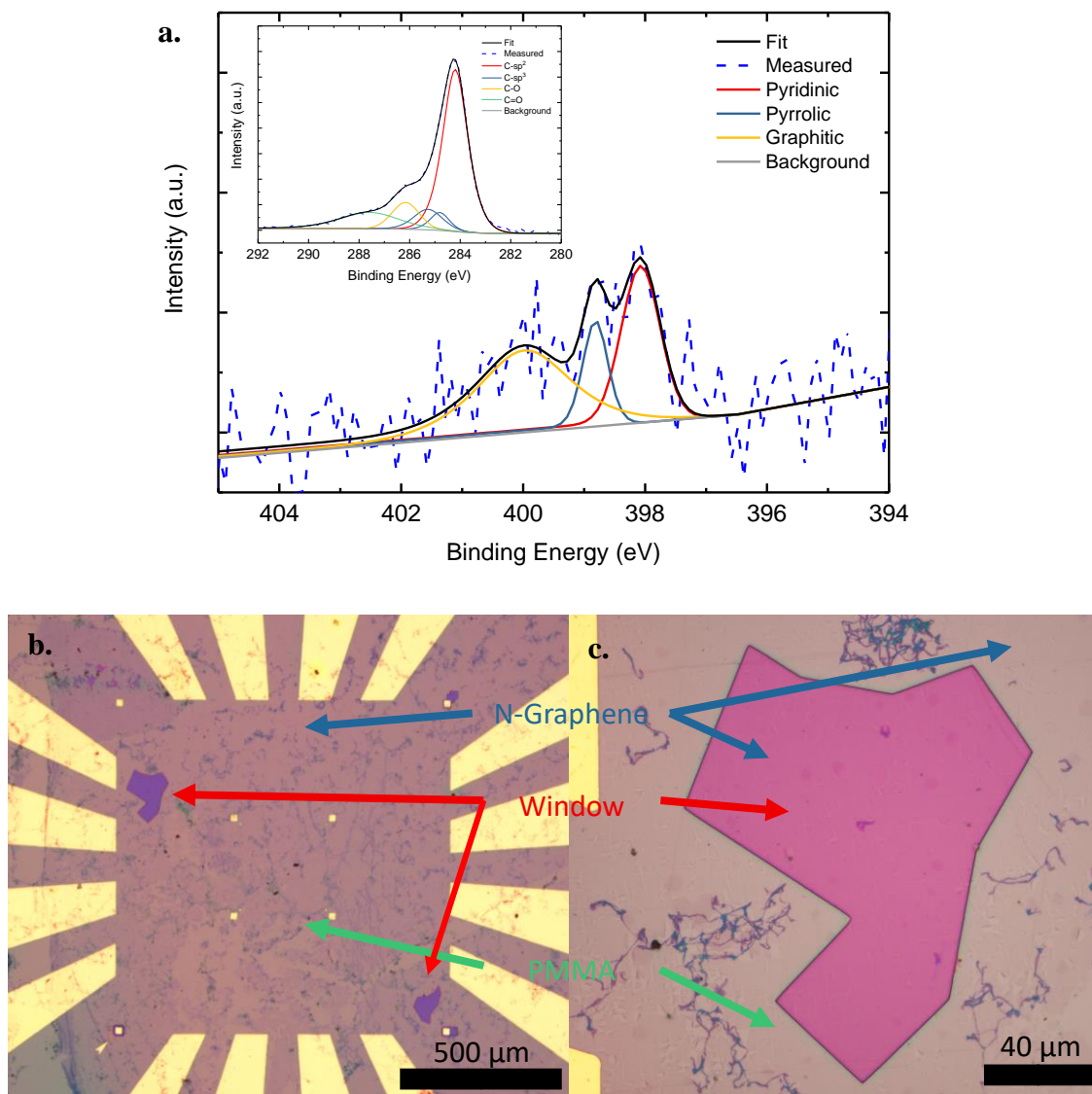


**Figure 8.13:** (a) Typical C1s and N1s spectra for the N-graphene sample after transferring to the pre-patterned chip. (b) Optical microscope images for the completed electrochemical microcell device demonstrating the full coverage of N-graphene throughout the substrate, open window and passivation with PMMA. (c) An individual opened window showing the underlying N-graphene and PMMA edges.

carbon and nitrogen. The inset contains the expected C1s spectra for NH<sub>3</sub> annealed graphene.

Once we confirmed that the graphene had been nitrogen doped, we moved to open windows using electron beam lithography and PMMA as our electron beam resist. Similar to our previous microcell measurements, we used thick layers of PMMA to prevent any electrical contact between the electrolyte and our gold pads. Extra care is taken to open windows only on the graphene electrocatalyst without exposing gold. Also, the windows are opened nearby a large gold pad to reduce the path and resistance for electrons supplied by the potentiostat to reach the catalyst surface. Areas where the graphene was found to be cleanest and near a gold pad were ideal. Optical images of the electrochemical microcell devices are shown in Figure 13b,c. The opened windows can be seen nearby a large gold pad, while everything else is covered in PMMA. When studied closely, the N-graphene can be seen in each of the windows as shown in Figure 8.13c.

Using the microcell set up we measured the electrocatalytic behavior for the ORR of N-graphene using CV at 10 mV/s in 0.5 M H<sub>2</sub>SO<sub>4</sub>. We extracted the polarization curves for N<sub>2</sub> and O<sub>2</sub> gas saturated conditions and these are shown in Figure 8.14 for several experiments on the same sample. The results are inconclusive as there is no distinct difference between the curves in the two conditions. In fact, one of the measurements performed in N<sub>2</sub> gas saturated electrolyte had a higher current density than any of the O<sub>2</sub> gas saturated measurements. It does appear that all of samples have an onset potential of

$\sim 0.3$  V vs RHE, however it is difficult to claim that this corresponds to the onset of ORR

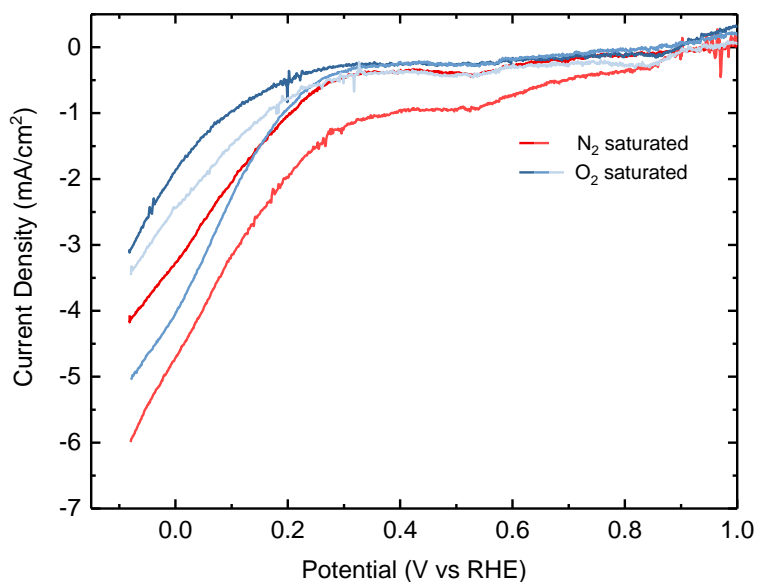


**Figure 8.14:** Polarization curves taken on the same device with N<sub>2</sub> and O<sub>2</sub> gas saturated 0.5 M electrolyte. No distinct difference is observed between the two electrolytes, suggesting that no ORR was taking place. Measurements were taken at a scan rate of 10 mV/s.

because it appears in both N<sub>2</sub> and O<sub>2</sub> gas saturated electrolyte. As mentioned previously, the ORR is very sensitive to the concentration of O<sub>2</sub> gas dissolved into electrolyte. These inconclusive results may be a result of the dissolved O<sub>2</sub> gas diffusing out of solution into the air before the measurement could be performed. This would greatly reduce any possible current density that could be generated by the electrocatalyst.

Alternatively, it is possible that the N-graphene was being etched or broken up by the electrocatalytic measurements. Directly after the initial electrochemical measurements, we noticed that the current had greatly reduced to the point of noise. In this experiment we were probing the activity of the window in the bottom right corner as shown in Figure 8.15a. Upon inspection of the open windows through an optical microscope, we found that the N-graphene inside of the windows had been etched and broken up as shown in

the before and after optical images in Figure 8.15b,c. However, we can also see that the N-graphene beneath the PMMA remains undamaged and the PMMA itself appears

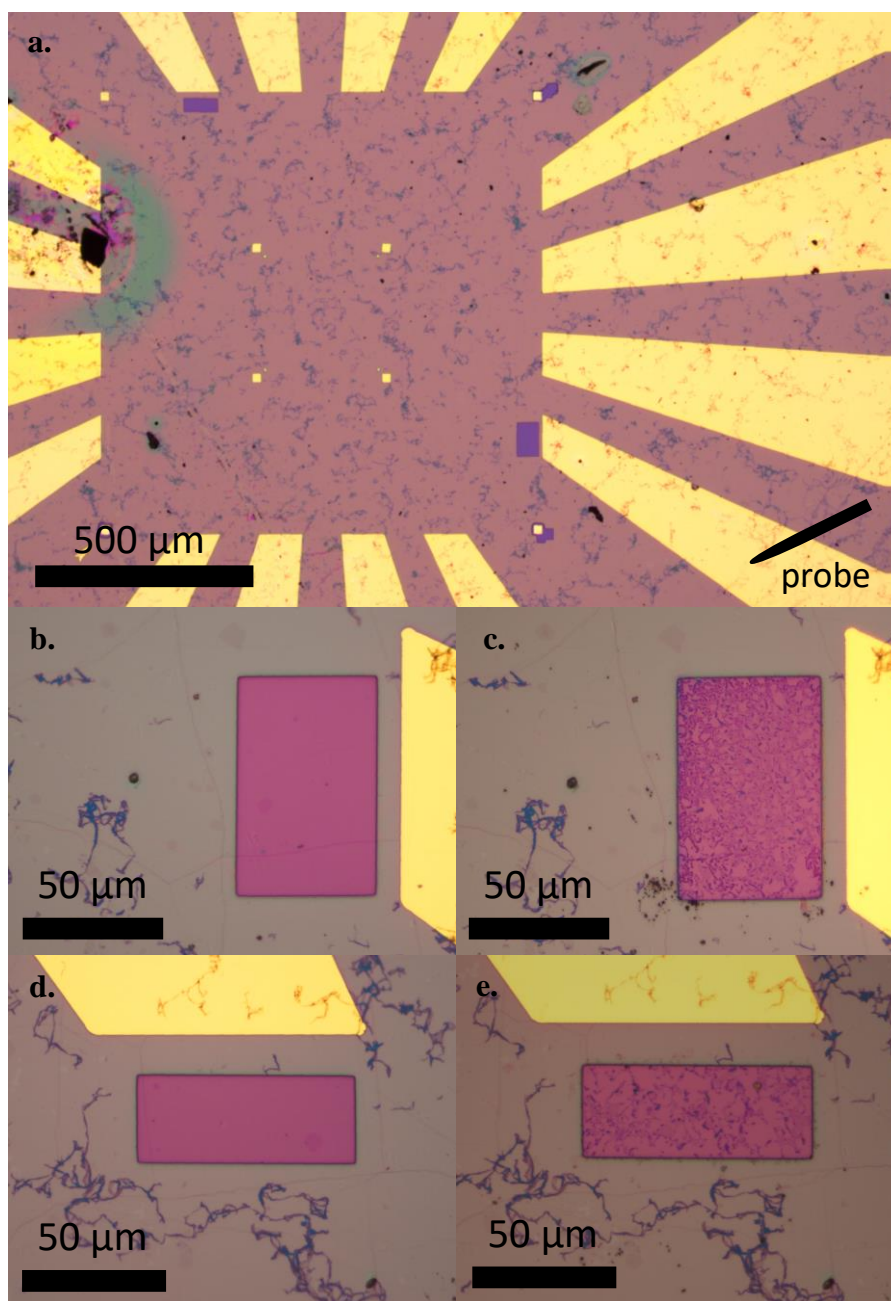


**Figure 8.15:** Optical microscope images of the damage during the electrocatalytic experiment. (a) Electrochemical microcell device with the aim to measure the electrocatalytic properties of the window in the bottom right corner by probing the nearby gold pad. Images (b) before and (c) after the electrochemical experiment of the opened window nearby the probed gold pad. Clear damage and etching can be seen to the N-graphene sheet. Images (d) before and (e) after the electrochemical experiment of the opened window far from the probed gold pad. Even more damage has occurred to the N-graphene sheet in comparison to the nearby window. Undamaged N-graphene can be seen underneath the PMMA layer.

undamaged. On samples where multiple windows were opened, N-graphene within a window not directly near the gold pad being probed but within the bubble of the electrolyte was also found to be etched as shown in Figure 8.15d,e. Windows not within the electrolyte remained intact. Etching was consistently found in both N<sub>2</sub> and O<sub>2</sub> gas saturated electrolytes. Continued measurement of the same window resulted in nearly complete etching of the N-graphene. We believe this may be happening due to the presence of N-graphene along the entire substrate. While we intend to only apply the voltage for our CV experiment to only the N-graphene within the open window, due to the high conductivity of graphene we actually are applying a voltage to the entire sheet through the substrate. This is evidenced by the fact that we saw etching in windows that had been opened far from the electrical probe, thus far from the initial injection point of electrons from the potentiostat. They would have to travel past the nearby window that is electrochemically connected to the counter electrode to the next opened window. It also appears that the voltage being applied to the graphene sheet is focused around the same area where the drop of electrolyte is located. This is expected because N-graphene in windows not included in the electrolyte bubble were not damaged. The etching may occur due to electrons supplied by the voltage trying to get through the PMMA layer to the electrolyte through the path of least resistance which is through the open windows. When the opened windows are saturated, the PMMA layer may act as a resistor and heat up leading to damage of the PMMA or boiling of the electrolyte. Boiling of the electrolyte was observed as the electrolyte began to evaporate while running CV experiments. The PMMA layer shows visible signs of damage and discoloration as shown in Figure 8.16.

The PMMA layer is clearly discolored in the area where the boiling electrolyte was seen. In addition, bubbles, bumps and some tears were observed throughout the entire area that are not seen on other areas of the PMMA. It is noted that the N-graphene sheet continues into the region where the discoloration and damage is seen

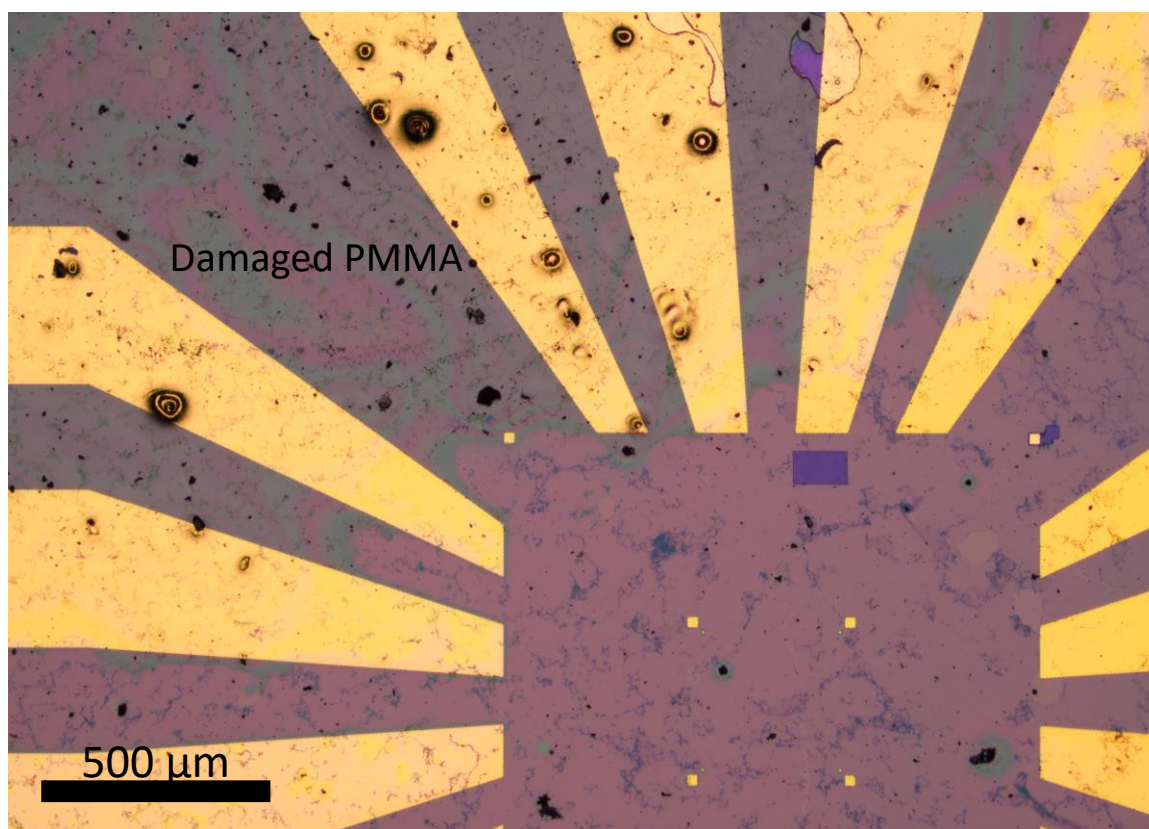


**Figure 8.16:** Optical microscope image showing the damage to the PMMA layer due to boiling of the electrolyte. Bubbles and bumps can be seen along the PMMA layer within the damaged region.

## 8.7 Conclusions

While our work on fabricating electrochemical microcells on nitrogen doped graphene was not conclusive on the active site for the ORR in nitrogen doped graphene materials, we were successful in developing methods that are promising for the effective fabrication of these devices. Our initial electrochemical measurements, although thought to be

graphene and nitrogen doped graphene, demonstrated that it is possible to measure the electrocatalytic activity of 2D graphene materials for the ORR using an electrochemical microcell. Our initial results did not compare and contrast directly graphene and nitrogen doped graphene, in reality our electrochemical measurements show the improvement in current density and onset potential based upon the creation of defects due to the patterning process. It is well known that defects can act as active sites for many electrocatalytic reactions.<sup>105,171</sup> Recently, surface oxygenated defects have been shown to improve activity and selectivity for hydrogen peroxide production in carbon materials.<sup>218</sup> It is possible with further optimization that this system could be further optimized towards hydrogen peroxide production.

Our troubleshooting approaches, although not successful for fabricating microcell devices, provide a pathway for different types of devices. Due to the flexibility of the patterning process, it is possible to pattern graphene into several different shapes such as graphene nanoribbons or more complex structures. By annealing the patterned graphene samples in  $\text{NH}_3$ , it is possible to achieve a n-type graphene sheet of specific shape and size that can be transferred onto arbitrary substrates for heterostructure electronic devices.



## **Chapter 9. Future Work and Conclusions**

### **9.1 Future Work**

Investigation and understanding of the active site for electrocatalytic reactions is crucial for further successful catalyst development. A few examples of future applications of the work shown in this thesis are discussed in this chapter.

#### **9.1.1 Nitrogen Bonding Configuration in Graphene based Materials**

It is likely that with further optimization of the patterning and fabrication process, electrochemical microcells on 2D nitrogen doped graphene can be realized. The development of different nitrogen doping methods have been shown that can influence the eventual bonding configuration.  $\text{NH}_3$  annealing has been shown to prefer the pyridinic configuration. Exposure to nitrogen plasma<sup>219</sup> or  $\text{NH}_3$  plasma<sup>102,105</sup> can preferentially incorporate nitrogen into the pyrrolic bonding configuration. Graphitic nitrogen bonding configurations have recently been shown to be possible by bubbling in acetonitrile during the CVD growth process.<sup>220</sup> Measuring the electrocatalytic properties is possible using the fabrication methodology we have developed, after some optimization of the graphene patterning process. The active site for nitrogen doped graphene has not yet been identified; measuring each of these nitrogen doped graphene samples may give some insight into how the nitrogen bonding configuration affects the performance.

#### **9.1.2 Electrochemical activity of other 2D Materials**



Other 2D materials, other than MoS<sub>2</sub>, have been shown to be active for both the HER and the ORR. Materials such as TaS<sub>2</sub><sup>221</sup>, NbS<sub>2</sub><sup>221</sup>, WS<sub>2</sub><sup>44</sup> and many others<sup>176</sup> have been investigated using a classic three electrode cell setup. With some TMDs even showing activity for the OER<sup>138</sup>, it is crucial for a well-developed and in depth study of what the active sites are in these materials. Measuring a single 2D flakes of these materials is challenging, but it eliminates many of the outside factors that can influence measurements in a classic three electrode cell. As we demonstrated, we could tune the contact resistance in our devices. The contact resistance is typically not considered, but could greatly affect the activity of your electrocatalyst. Microelectrodes will also exhibit less charging current due to the thinning of the diffusion layer at the surface of the electrode.<sup>148</sup> In 2D materials especially, reducing the thickness to a single flake removes any resistance due to electrons moving across the van der Waal's gap. Fabrication of an electrochemical microcell on 2D materials allows for a clean surface with the removal of many outside factors, or possibly control of them, that can yield an intrinsic study of the electrocatalytic activity.

### 9.1.3 Beyond Electrochemistry

While our primary focus has been on electrochemical applications, possibilities exist for using this fabrication technique in other applications. Opening windows directly on top of 2D materials could allow for the deposition of various solution-processed materials, if in non-polar to mildly polar solvents to prevent dissolution of the PMMA layer. For example, dropcasting or spincoating photo-absorbing polymers or photoactive hybrid-inorganic organic perovskite materials on top of 2D materials could allow for the fabrication of highly sensitive but very thin photodiode and photodetectors. Another

option is the use of solution processed gold nanoparticles, that can be made into different shapes to change their plasmonic properties. Coupling these particles with 2D materials can be challenging due to the difference in scale. Dropcasting these particles from solution onto a sample of 2D MoS<sub>2</sub> with an open window on the basal plane could improve the chances for contact. Focused functionalization is also possible of 2D materials. The flexibility that electron beam lithography gives for the shape and size of these open windows can allow the functionalization of discrete areas that could be useful for building sensors.

Each of the projects mentioned above are extensions of the electrochemical microcell fabrication technique we have developed. Additional optimization and experimentation would be fitting for the research of a doctoral student or post-doctoral researcher.

## 9.2 Conclusions

Developing cost-effective and efficient electrocatalysts for the HER and the ORR are crucial for the successful utilization of hydrogen as an alternative fuel. Two dimensional electrocatalysts such as MoS<sub>2</sub> and nitrogen doped graphene have been recognized as possible candidates for replacing expensive catalysts such as platinum, due to their to be high activity for the HER and the ORR, respectively. However, their performance has not yet exceeded platinum. Identifying the active site for these reactions on these materials is imperative for further improving their electrocatalytic behavior.

Using electron beam lithography, we developed a method of fabricating electrochemical microcells on 2D materials, such as MoS<sub>2</sub>, with lateral dimensions of 10 to 20  $\mu\text{m}$ . This allowed us to electrochemically test discrete areas of the 2D MoS<sub>2</sub> nanosheet, including

the basal plane. Coupled with organometallic chemistry, we could vary the contact resistance to the 2D MoS<sub>2</sub> nanosheet by converting from the semiconducting 2H phase to the metallic 1T phase. When the contact resistance is decreased, the performance of our MoS<sub>2</sub> electrocatalysts for the HER was improved. When sufficiently decreased we found that the basal plane, which has previously been thought to be inactive, exhibited excellent catalytic activity, comparable to 1T MoS<sub>2</sub>. When examined using STEM, the basal plane was found to contain sulfur vacancies, acting as the active site the HER. Improvement of the contact resistance facilitated charge transfer from the substrate to the catalyst, allowing for measurement of high catalytic activity of the 2H basal plane.

In parallel, we developed a method to efficiently reduce GO using conventional microwaves. This microwave reduction yielded high quality graphene, termed MWrGO. A combination of Raman spectroscopy and XPS study demonstrated the high graphene character of MWrGO that had very little oxygen functionalization. Further application of MWrGO in field effect transistor devices demonstrated the high conductivity and yielded mobility values of greater than  $1000 \text{ cm}^2 \text{ V}^{-1} \text{ s}^{-1}$ , much greater than typically seen for GO-based materials. We attribute the rapid reduction of MWrGO to the fast heating of water, by the microwave oven, that is trapped within the rGO sheets. Previously the removal of water in GO based materials has been shown to be important for the ORR activity in acidic condition.<sup>212</sup> Coupled with the high conductivity and graphene character of MWrGO, we sought to nitrogen dope MWrGO and study its electrocatalytic properties for the ORR in acidic conditions. When nitrogen is doped into graphene it can bond into three different configuration: pyridinic, pyrrolic and graphitic. We used NH<sub>3</sub> annealing to dope MWrGO with nitrogen, and studied the effects using Raman spectroscopy and XPS.

Initially, the  $\text{NH}_3$  annealing was creating defects within the MWrGO lattice. As we increased the annealing time, we successfully doped nitrogen into MWrGO. Coupled with XPS we found that very little oxygen functionalization occurs, instead the majority of defects are being created by the incorporation of nitrogen disrupting the local symmetry within the MWrGO lattice. We extracted the resultant atomic percentage of nitrogen from our XPS, and found that as  $\text{NH}_3$  annealing time increases so does the nitrogen content. The pyridinic nitrogen bonding configuration was found to dominate the N-MWrGO, until the pyrrolic configuration overtakes it at an annealing time of 8 hours. Our electrocatalytic results showed that as annealing time increased, so did the catalytic performance, until after 8 hours, where the onset potential actually shifts negative. We found that the onset potential shifted more positive coupled with an increases in current density for samples annealed at 6 hours. Although the absolute nitrogen content is similar, after 8 hours of  $\text{NH}_3$  annealing the electrocatalytic behavior decreases noted by a negative shift in onset potential and decrease in current density. This suggests that the pyridinic nitrogen bonding configuration has a stronger influence on the ORR activity of N-MWrGO.

To further study the effect of nitrogen doping on graphene materials, we attempted to apply our electrochemical microcell methodology to nitrogen doped CVD grown graphene (N-graphene). In order to build the devices, we developed a method to pattern the N-graphene to a size that would suit the microcell structure, using electron beam lithography with a negative resist. This was used to pattern both graphene and N-graphene and measured the electrocatalytic measurements. We did observe an improvement in the onset potential after  $\text{NH}_3$  annealing, however some inconsistent

measurements with subsequent samples lead to further investigation of the patterned N-graphene. Using XPS, we found that the nitrogen had been removed sometime during the device fabrication process, leaving defects and disorder in the graphene lattice. A step by step study of the fabrication process found that the patterning process using a negative electron beam resist was damaging the N-graphene. We made significant efforts to fabricate devices in which the N-graphene would remain undamaged. Our first approach took advantage of the fact that the patterned graphene samples did not show any damage from the process. These patterned graphene samples were then annealed in  $\text{NH}_3$  along with the pre-patterned  $\text{SiO}_2/\text{Si}$  substrate. When we investigated the nitrogen content of these samples using XPS, we found that nitrogen seemed to dope into the chip however it had also doped into the  $\text{SiO}_2$  substrate forming silicon nitride. In our second approach, we directly opened windows on as transferred N-graphene in order to measure the ORR activity of the N-graphene sheet without patterning. This resulted in N-graphene covering the entire pre-patterned substrate, connecting adjacent gold pads. Unfortunately, our electrocatalytic measurements were unsuccessful as no differences were observed in  $\text{N}_2$  and  $\text{O}_2$  gas saturated electrolytes. In addition, we noticed that the N-graphene within the opened windows had been damaged or etched during the electrochemical measurement. This could be due to the fact that when potential was applied to the sample, the entire N-graphene sheet would be polarized and electrons moving through the opened windows were causing damage.

Although our investigation into the active site for the ORR in graphene based materials was inconclusive, we successfully doped MWrGO by  $\text{NH}_3$  annealing and demonstrated that our microcell fabrication method could be applied to other 2D materials, such as

graphene. Our study on N-MWrGO suggest that the pyridinic nitrogen bonding configuration can have an effect on the catalytic performance, we were unable to confirm this result using our microcell setup. We were able to electrochemically test graphene and what we eventually determined to be defective graphene. After creating defects in the graphene sheet, we observed an improvement in the ORR performance. This is a promising result for future work and investigation into the active site in nitrogen doped graphene materials.

## References

1. International Energy Agency. World Energy Outlook 2015. Executive Summary. *Int. Energy Agency books online* 1–9 (2015). doi:10.1787/weo-2005-en
2. IEA International Energy Agency. World Energy Outlook 2017. *Int. Energy Agency* (2017). doi:10.1016/0301-4215(73)90024-4
3. McGlade, C. & Ekins, P. The geographical distribution of fossil fuels unused when limiting global warming to 2 °C. *Nature* **517**, 187–190 (2015).
4. Boden, T. A., Marland, G. & Andres, R. J. Global, Regional, and National Fossil-Fuel CO<sub>2</sub> Emissions. *Carbon Dioxide Inf. Anal. Cent.* (2015). doi:10.3334/CDIAC/00001\_V2015
5. Tester, J. W., Drake, E. M., Driscoll, J. M., Golay, M. W. & Peters, W. A. *Sustainable Energy: Choosing Among Options*. MIT Press (MIT Press, Cambridge Massachusetts, 2012).
6. Melillo, J. M., Richmond, T. C. & Yohe, G. W. Climate change impacts in the United States: The third National Climate Assessment. *U.S. Global Change Research Program*. Available at: <http://nca2014.globalchange.gov/>.
7. BP Statistical Review of World Energy. (2015). Available at: <http://www.bp.com/statisticalreview>.
8. BP. BP Statistical Review of World Energy 2017. *Br. Pet.* 1–52 (2017). doi:<http://www.bp.com/content/dam/bp/en/corporate/pdf/energy-economics/statistical-review-2017/bp-statistical-review-of-world-energy-2017-full-report.pdf>
9. Harvey, J. Platinum's days as fuel cell car component may be numbered. *Reuters* (2018).
10. Gray, R. The biggest energy challenges facing humanity. *BBC* (2017).
11. Fuel Cells. *U.S. Office of Energy Efficiency and Renewable Energy* Available at: <https://www.energy.gov/eere/fuelcells/fuel-cells>.
12. Garche, J. & Ludwig, J. Applications of Fuel Cell Technology : Status and Perspectives. *Electrochem. Soc. Interface* 39–43 (2015). doi:10.1149/2.F02152if
13. Sharaf, O. Z. & Orhan, M. F. An overview of fuel cell technology: Fundamentals and applications. *Renew. Sustain. Energy Rev.* **32**, 810–853 (2014).
14. Shao, M., Chang, Q., Dodelet, J.-P. & Chenitz, R. Recent Advances in Electrocatalysts for Oxygen Reduction Reaction. *Chem. Rev.* **116**, 3594–3657 (2016).
15. Lukowski, M. A. *et al.* Enhanced hydrogen evolution catalysis from chemically exfoliated metallic MoS<sub>2</sub> nanosheets. *J. Am. Chem. Soc.* **135**, 10274–10277 (2013).
16. Dai, L., Xue, Y., Qu, L., Choi, H.-J. & Baek, J.-B. Metal-Free Catalysts for Oxygen Reduction Reaction. *Chem. Rev.* **115**, 4823–4892 (2015).
17. Voiry, D. *et al.* keepConducting MoS<sub>2</sub> nanosheets as catalysts for hydrogen evolution reaction. *Nano Lett.* **13**, 6222–7 (2013).
18. Jaramillo, T. F. *et al.* Identification of active edge sites for electrochemical H<sub>2</sub> evolution from MoS<sub>2</sub> nanocatalysts. *Science* **317**, 100–2 (2007).
19. Guo, D. *et al.* Active sites of nitrogen-doped carbon materials for oxygen

- reduction reaction clarified using model catalysts. *Science* (80-. ). **351**, 1–24 (2015).
20. Qu, L., Liu, Y., Baek, J. B. & Dai, L. Nitrogen-doped graphene as efficient metal-free electrocatalyst for oxygen reduction in fuel cells. *ACS Nano* **4**, 1321–1326 (2010).
  21. Kibsgaard, J., Chen, Z., Reinecke, B. N. & Jaramillo, T. F. Engineering the surface structure of MoS<sub>2</sub> to preferentially expose active edge sites for electrocatalysis. *Nat. Mater.* **11**, 963–969 (2012).
  22. Li, X., Hao, X., Abudula, A. & Guan, G. Nanostructured catalysts for electrochemical water splitting: current state and prospects. *J. Mater. Chem. A* **4**, 11973–12000 (2016).
  23. Hoang, S. *et al.* Improvement of solar energy conversion with Nb-incorporated TiO<sub>2</sub> hierarchical microspheres. *ChemPhysChem* **14**, 2270–2276 (2013).
  24. Kudo, A. & Miseki, Y. Heterogeneous photocatalyst materials for water splitting. *Chem. Soc. Rev.* **38**, 253–278 (2009).
  25. Chhowalla, M. *et al.* The chemistry of two-dimensional layered transition metal dichalcogenide nanosheets. *Nat. Chem.* **5**, 263–75 (2013).
  26. Miro, P., Audiffred, M. & Heine, T. An atlas of two-dimensional materials. *Chem. Soc. Rev.* **43**, 6537–6554 (2014).
  27. Wilson, J. A. & Yoffe, A. D. The transition metal dichalcogenides discussion and interpretation of the observed optical, electrical and structural properties. *Adv. Phys.* **18**, 193–335 (1969).
  28. Xia, F., Wang, H., Xiao, D., Dubey, M. & Ramasubramaniam, A. Two-dimensional material nanophotonics. *Nat. Photonics* **8**, 899–907 (2014).
  29. Wang, R. *et al.* Ultrafast and spatially resolved studies of charge carriers in atomically thin molybdenum disulfide. *Phys. Rev. B - Condens. Matter Mater. Phys.* **86**, 1–5 (2012).
  30. Park, S. & Ruoff, R. S. Chemical methods for the production of graphenes. *Nat. Nanotechnol.* **4**, 45–47 (2009).
  31. Nicolosi, V., Chhowalla, M., Kanatzidis, M. G., Strano, M. S. & Coleman, J. N. Liquid Exfoliation of Layered Materials. *Science* (80-. ). **340**, 1226419 (2013).
  32. Gong, Y. *et al.* Direct chemical conversion of graphene to boron- and nitrogen- and carbon-containing atomic layers. *Nat. Commun.* **5**, 3193 (2014).
  33. Song, L. *et al.* Large scale growth and characterization of atomic hexagonal boron nitride layers. *Nano Lett.* **10**, 3209–3215 (2010).
  34. Castellanos-Gomez, A. Why all the fuss about 2D semiconductors? *Nat. Photonics* **10**, 202–204 (2016).
  35. Kalantar-zadeh, K. *et al.* Synthesis of nanometre-thick MoO<sub>3</sub> sheets. *Nanoscale* **2**, 429–433 (2010).
  36. Kalantar-zadeh, K. *et al.* Two dimensional and layered transition metal oxides. *Appl. Mater. Today* **5**, 73–89 (2016).
  37. Zhang, H. *et al.* Topological insulators in Bi<sub>2</sub>Se<sub>3</sub>, Bi<sub>2</sub>Te<sub>3</sub> and Sb<sub>2</sub>Te<sub>3</sub> with a single Dirac cone on the surface. *Nat. Phys.* **5**, 438–442 (2009).
  38. Lalmi, B. *et al.* Epitaxial growth of a silicene sheet. *Appl. Phys. Lett.* **97**, 223107–223109 (2010).
  39. Li, L. *et al.* Black phosphorus field-effect transistors. *Nat. Nanotechnol.* **9**, 372–



- 377 (2014).
40. Blancon, J.-C. *et al.* Extremely efficient internal exciton dissociation through edge states in layered 2D perovskites. *Science* (80-. ). **355**, 1288–1292 (2017).
  41. Tsai, H. *et al.* High-efficiency two-dimensional Ruddlesden–Popper perovskite solar cells. *Nature* **536**, 312–316 (2016).
  42. Splendiani, A. *et al.* Emerging photoluminescence in monolayer MoS<sub>2</sub>. *Nano Lett.* **10**, 1271–1275 (2010).
  43. Voiry, D., Yang, J. & Chhowalla, M. Recent Strategies for Improving the Catalytic Activity of 2D TMD Nanosheets Toward the Hydrogen Evolution Reaction. *Adv. Mater.* (2016). doi:10.1002/adma.201505597
  44. Voiry, D. *et al.* Enhanced catalytic activity in strained chemically exfoliated WS<sub>2</sub> nanosheets for hydrogen evolution. *Nat. Mater.* **12**, 850–855 (2013).
  45. Hu, C. & Dai, L. Multifunctional Carbon-Based Metal-Free Electrocatalysts for Simultaneous Oxygen Reduction, Oxygen Evolution, and Hydrogen Evolution. *Adv. Mater.* **29**, 1604942 (2017).
  46. Chhowalla, M., Jena, D. & Zhang, H. Two-dimensional semiconductors for transistors. *Nat. Rev. Mater.* **1**, 16052 (2016).
  47. Kappera, R. *et al.* Phase-engineered low-resistance contacts for ultrathin MoS<sub>2</sub> transistors. *Nat. Mater.* 1–15 (2014). doi:10.1038/nmat4080
  48. Radisavljevic, B., Radenovic, A., Brivio, J., Giacometti, V. & Kis, A. Single-layer MoS<sub>2</sub> transistors. *Nat. Nanotechnol.* **6**, 147–50 (2011).
  49. Sun, Z. *et al.* Infrared photodetectors based on CVD-grown graphene and PbS quantum dots with ultrahigh responsivity. *Adv. Mater.* **24**, 5878–5883 (2012).
  50. Acerce, M., Voiry, D. & Chhowalla, M. Metallic 1T phase MoS<sub>2</sub> nanosheets as supercapacitor electrode materials. *Nat. Nanotechnol.* **10**, 1–15 (2015).
  51. Cooper, D. R. *et al.* Experimental Review of Graphene. *ISRN Condens. Matter Phys.* **2012**, 1–56 (2012).
  52. Geim, A. K. & Novoselov, K. S. The rise of graphene. *Nat. Mater.* **6**, 183–91 (2007).
  53. Bae, S. *et al.* Roll-to-roll production of 30-inch graphene films for transparent electrodes. *Nat. Nanotechnol.* **5**, 574–578 (2010).
  54. Li, X. S. *et al.* Transfer of Large-Area Graphene Films for High-Performance Transparent Conductive Electrodes. *Nano Lett.* **9**, 4359–4363 (2009).
  55. Kim, K. S. *et al.* Large-scale pattern growth of graphene films for stretchable transparent electrodes. *Nature* **457**, 706–710 (2009).
  56. Novoselov, K. S. *et al.* A roadmap for graphene. *Nature* **490**, 192–200 (2012).
  57. Chua, C. K. & Pumera, M. The reduction of graphene oxide with hydrazine: elucidating its reductive capability based on a reaction-model approach. *Chem. Commun.* **52**, 72–75 (2016).
  58. Dreyer, D. R., Park, S., Bielawski, C. W. & Ruoff, R. S. The chemistry of graphene oxide. *Chem. Soc. Rev.* **39**, 228–240 (2010).
  59. He, H. Y., Klinowski, J., Forster, M. & Lerf, A. A new structural model for graphite oxide. *Chem. Phys. Lett.* **287**, 53–56 (1998).
  60. Lerf, A., He, H., Forster, M. & Klinowski, J. Structure of Graphite Oxide Revisited. *J. Phys. Chem. B* **102**, 4477–4482 (1998).
  61. Liu, Z. B. *et al.* Porphyrin and fullerene covalently functionalized graphene hybrid

- materials with large nonlinear optical properties. *J. Phys. Chem. B* **113**, 9681–9686 (2009).
62. Stankovich, S. *et al.* Synthesis of graphene-based nanosheets via chemical reduction of exfoliated graphite oxide. *Carbon N. Y.* **45**, 1558–1565 (2007).
  63. Fang, M., Wang, K. G., Lu, H. B., Yang, Y. L. & Nutt, S. Covalent polymer functionalization of graphene nanosheets and mechanical properties of composites. *J. Mater. Chem.* **19**, 7098–7105 (2009).
  64. Cai, W. *et al.* Synthesis and Solid-State NMR Structural Characterization of <sup>13</sup>C-Labeled Graphite Oxide. *Science (80-. )*. **321**, 1815–1817 (2008).
  65. Schniepp, H. C. *et al.* Functionalized single graphene sheets derived from splitting graphite oxide. *J. Phys. Chem. B* **110**, 8535–8539 (2006).
  66. Hernandez, Y. *et al.* High yield production of graphene by liquid phase exfoliation of graphite. *Nat. Nanotechnol.* **3**, 563–8 (2008).
  67. Li, D., Müller, M. B., Gilje, S., Kaner, R. B. & Wallace, G. G. Processable aqueous dispersions of graphene nanosheets. *Nat. Nanotechnol.* **3**, 101–105 (2008).
  68. Allen, M. J., Tung, V. C. & Kaner, R. B. Honeycomb carbon: A review of graphene. *Chem. Rev.* **110**, 132–145 (2010).
  69. Gilje, S., Han, S., Wang, M., Wang, K. L. & Kaner, R. B. A chemical route to graphene for device applications. *Nano Lett.* **7**, 3394–3398 (2007).
  70. Stankovich, S. *et al.* Stable aqueous dispersions of graphitic nanoplatelets via the reduction of exfoliated graphite oxide in the presence of poly(sodium 4-styrenesulfonate). *J. Mater. Chem.* **16**, 155–158 (2006).
  71. Shin, H.-J. J. *et al.* Efficient reduction of graphite oxide by sodium borohydride and its effect on electrical conductance. *Adv. Funct. Mater.* **19**, 1987–1992 (2009).
  72. Dong, L., Yang, J., Chhowalla, M. & Loh, K. P. Synthesis and reduction of large sized graphene oxide sheets. *Chem. Soc. Rev.* **46**, 7306–7316 (2017).
  73. Loh, K. P., Bao, Q., Eda, G. & Chhowalla, M. Graphene oxide as a chemically tunable platform for optical applications. *Nat. Chem.* **2**, 1015–1024 (2010).
  74. Becerril, H. A. H. A. *et al.* Evaluation of Solution-Processed Reduced Graphene Oxide Films as Transparent Conductors. *ACS Nano* **2**, 463–470 (2008).
  75. Guo, Y. L. *et al.* General Route toward Patterning of Graphene Oxide by a Combination of Wettability Modulation and Spin-Coating. *ACS Nano* **4**, 5749–5754 (2010).
  76. Yamaguchi, H., Eda, G., Mattevi, C., Kim, H. & Chhowalla, M. Highly uniform 300 mm wafer-scale deposition of single and multilayered chemically derived graphene thin films. *ACS Nano* **4**, 524–528 (2010).
  77. Eda, G., Fanchini, G. & Chhowalla, M. Large-area ultrathin films of reduced graphene oxide as a transparent and flexible electronic material. *Nat. Nanotechnol.* **3**, 270–274 (2008).
  78. Dikin, D. A. *et al.* Preparation and characterization of graphene oxide paper. *Nature* **448**, 457–460 (2007).
  79. Jiang, Y. *et al.* Versatile Graphene Oxide Putty-Like Material. *Adv. Mater.* n/a-n/a (2016). doi:10.1002/adma.201603284
  80. García-Tuñón, E. *et al.* Graphene Oxide: An All-in-One Processing Additive for 3D Printing. *ACS Appl. Mater. Interfaces* **9**, 32977–32989 (2017).

81. Stankovich, S. *et al.* Graphene-based composite materials. *Nature* **442**, 282–286 (2006).
82. Gómez-Navarro, C. *et al.* Electronic transport properties of individual chemically reduced graphene oxide sheets. *Nano Lett.* **7**, 3499–3503 (2007).
83. McAllister, M. J. *et al.* Single Sheet Functionalized Graphene by Oxidation and Thermal Expansion of Graphite. *Chem. Mater.* **19**, 4396–4404 (2007).
84. Eda, G., Mattevi, C., Yamaguchi, H., Kim, H. & Chhowalla, M. Insulator to semimetal transition in graphene oxide. *J. Phys. Chem. C* **113**, 15768–15771 (2009).
85. Jung, I., Dikin, D. A., Piner, R. D. & Ruoff, R. S. Tunable Electrical Conductivity of Individual Graphene Oxide Sheets Reduced at “Low” Temperatures. *Nano Lett.* **8**, 4283–4287 (2008).
86. Shen, B., Zhai, W. & Zheng, W. Ultrathin Flexible Graphene Film: An Excellent Thermal Conducting Material with Efficient EMI Shielding. *Adv. Funct. Mater.* **24**, 4542–4548 (2014).
87. Bagri, A. *et al.* Structural evolution during the reduction of chemically derived graphene oxide. *Nat. Chem.* **2**, 581–587 (2010).
88. Chua, C. K. & Pumera, M. Chemical reduction of graphene oxide: a synthetic chemistry viewpoint. *Chem. Soc. Rev.* **43**, 291–312 (2014).
89. Brown, W. H., Foote, C. S., Iverson, B. L. & Anslyn, E. V. *Organic Chemistry*. (Brooks/Cole Cengage Learning, 2009).
90. Kim, M. C., Hwang, G. S. & Ruoff, R. S. Epoxide reduction with hydrazine on graphene: A first principles study. *J. Chem. Phys.* **131**, 1–6 (2009).
91. Park, S. *et al.* Chemical structures of hydrazine-treated graphene oxide and generation of aromatic nitrogen doping. *Nat. Commun.* **3**, 638 (2012).
92. Abulizi, A. *et al.* Vitamin C Is an Ideal Substitute for Hydrazine in the Reduction of Graphene Oxide Suspensions. *J. Phys. Chem. C* **4**, 6426–6432 (2013).
93. Wang, X., Kholmanov, I., Chou, H., Ruoff, R. S. & Al, W. E. T. Simultaneous Electrochemical Reduction and Delamination of Graphene Oxide Films. *ACS Nano* (2015).
94. Wang, Y. *et al.* Reduced graphene oxide film with record-high conductivity and mobility. *Mater. Today* **21**, 186–192 (2018).
95. Matsumoto, Y. *et al.* Simple Photoreduction of Graphene Oxide Nanosheet under Mild Conditions. *ACS Appl. Mater. Interfaces* **2**, 3461–3466 (2010).
96. Salas, E. C., Sun, Z., Lüttge, A. & Tour, J. M. Reduction of Graphene Oxide via Bacterial Respiration. *ACS Nano* **4**, 4852–4856 (2010).
97. Maldonado, S., Morin, S. & Stevenson, K. J. Structure, composition, and chemical reactivity of carbon nanotubes by selective nitrogen doping. *Carbon N. Y.* **44**, 1429–1437 (2006).
98. Nevidomskyy, A. H., Csányi, G. & Payne, M. C. Chemically active substitutional nitrogen impurity in carbon nanotubes. *Phys. Rev. Lett.* **91**, 105502 (2003).
99. Kim, D., Lin, C. & Mihalisin, T. Electronic properties of nitrogen-doped graphite flakes. *Chem. Mater.* **67**, 686–692 (1991).
100. Wiggins-Camacho, J. D. & Stevenson, K. J. Effect of nitrogen concentration on capacitance, density of states, electronic conductivity, and morphology of N-doped carbon nanotube electrodes. *J. Phys. Chem. C* **113**, 19082–19090 (2009).

101. Wei, D. *et al.* Synthesis of N-Doped Graphene by Chemical Vapor Deposition and Its Electrical Properties. *Nano Lett.* **9**, 1752–1758 (2009).
102. Liu, H., Liu, Y. & Zhu, D. Chemical doping of graphene. *J. Mater. Chem.* **21**, 3335 (2011).
103. Duan, J., Chen, S., Jaroniec, M. & Qiao, S. Z. Heteroatom-Doped Graphene-Based Materials for Energy-Relevant Electrocatalytic Processes. *ACS Catal.* **5**, 5207–5234 (2015).
104. Jin, Z., Yao, J., Kittrell, C. & Tour, J. M. Large-scale growth and characterizations of nitrogen-doped monolayer graphene sheets. *ACS Nano* **5**, 4112–4117 (2011).
105. Jin, H. *et al.* Emerging Two-Dimensional Nanomaterials for Electrocatalysis. *Chem. Rev.* [acs.chemrev.7b00689](https://doi.org/10.1021/acs.chemrev.7b00689) (2018). doi:10.1021/acs.chemrev.7b00689
106. Zhang, J., Xia, Z. & Dai, L. Carbon-based electrocatalysts for advanced energy conversion and storage. *Sci. Adv.* **1**, e1500564–e1500564 (2015).
107. Liu, X. & Dai, L. Carbon-based metal-free catalysts. *Nat. Rev. Mater.* **1**, 1–12 (2016).
108. Lu, Y. F. *et al.* Nitrogen-doped graphene sheets grown by chemical vapor deposition: Synthesis and influence of nitrogen impurities on carrier transport. *ACS Nano* **7**, 6522–6532 (2013).
109. Li, X. *et al.* Simultaneous Nitrogen Doping and Reduction of Graphene Oxide. *J. Am. Chem. Soc.* **131**, 15939–15944 (2009).
110. Ni, Z. H. *et al.* Reflection and Contrast Spectroscopy Graphene Thickness Determination Using Reflection and Contrast Spectroscopy. *Nano Lett.* **7**, 2758–2763 (2007).
111. Wang, Q. H., Kalantar-Zadeh, K., Kis, A., Coleman, J. N. & Strano, M. S. Electronics and optoelectronics of two-dimensional transition metal dichalcogenides. *Nat. Nanotechnol.* **7**, 699–712 (2012).
112. Chen, Z. *et al.* Core-shell MoO<sub>3</sub>-MoS<sub>2</sub> nanowires for hydrogen evolution: A functional design for electrocatalytic materials. *Nano Lett.* **11**, 4168–4175 (2011).
113. Pham, V. H., Gebre, T. & Dickerson, J. H. Facile electrodeposition of reduced graphene oxide hydrogels for high-performance supercapacitors. *Nanoscale* **7**, 5947–5950 (2015).
114. Xiao, J. *et al.* Exfoliated MoS<sub>2</sub> nanocomposite as an anode material for lithium ion batteries. *Chem. Mater.* **22**, 4522–4524 (2010).
115. Stephenson, T., Li, Z., Olsen, B. & Mitlin, D. Lithium ion battery applications of molybdenum disulfide (MoS<sub>2</sub>) nanocomposites. *Energy Environ. Sci.* **7**, 209 (2014).
116. Kang, D. *et al.* An Ultrahigh-Performance Photodetector based on a Perovskite – Transition-Metal-Dichalcogenide Hybrid Structure. *Adv. Mater.* (2016). doi:10.1002/adma.201600992
117. King, L. a., Zhao, W., Chhowalla, M., Riley, D. J. & Eda, G. Photoelectrochemical properties of chemically exfoliated MoS<sub>2</sub>. *J. Mater. Chem. A* **1**, 8935 (2013).
118. Meng, F., Li, J., Cushing, S. K., Zhi, M. & Wu, N. (Nick). Solar Hydrogen Generation by Nanoscale p – n Junction of p - type Molybdenum Disulfide/ n - type Nitrogen-Doped Reduced Graphene Oxide. *J. Am. Chem. Soc.* **135**, 2–5 (2013).
119. Kappera, R. *et al.* Metallic 1T phase source/drain electrodes for field effect

- transistors from chemical vapor deposited MoS<sub>2</sub>. *APL Mater.* **2**, (2014).
120. Shanmugam, M., Bansal, T., Durcan, C. A. & Yu, B. Molybdenum disulphide/titanium dioxide nanocomposite-poly 3-hexylthiophene bulk heterojunction solar cell. *Appl. Phys. Lett.* **100**, (2012).
  121. Yue, G., Wu, J., Xiao, Y. & Huang, M. High performance platinum-free counter electrode of molybdenum sulfide/carbon used in dye-sensitized solar cells. *J. Mater. Chem. A* **1**, 1495 (2013).
  122. Shastry, T. A. *et al.* Mutual Photoluminescence Quenching and Photovoltaic Effect in Large-Area Single-Layer MoS<sub>2</sub>–Polymer Heterojunctions. *ACS Nano* **10**, 6065–6072 (2016). doi:10.1021/acsnano.6b06592
  123. Eda, G. *et al.* Photoluminescence from Chemically Exfoliated MoS<sub>2</sub>. *Nano Lett.* **11**, 5111–5116 (2011).
  124. Voiry, D., Mohite, A. & Chhowalla, M. Phase engineering of transition metal dichalcogenides. *Chem. Soc. Rev.* **44**, 2702–2712 (2015).
  125. Novoselov, K. S. *et al.* Electric field effect in atomically thin carbon films. *Science* **306**, 666–9 (2004).
  126. Yi, M. & Shen, Z. A review on mechanical exfoliation for the scalable production of graphene. *J. Mater. Chem. A* **3**, 11700–11715 (2015).
  127. Chen, J., Duan, M. & Chen, G. Continuous mechanical exfoliation of graphene sheets via three-roll mill. *J. Mater. Chem.* **22**, 19625 (2012).
  128. Huang, Y. *et al.* Reliable Exfoliation of Large-Area High-Quality Flakes of Graphene and Other Two-Dimensional Materials. *ACS Nano* **9**, 10612–10620 (2015).
  129. Novoselov, K. S. & Castro Neto, A. H. Two-dimensional crystals-based heterostructures: materials with tailored properties. *Phys. Scr.* **T146**, 014006 (2012).
  130. Cunningham, G. *et al.* Solvent Exfoliation of Transition Metal Dichalcogenides: Dispersibility of Exfoliated Nanosheets Varies Only Weakly between Compounds. *ACS Nano* **6**, 3468–3480 (2012).
  131. Wan, J. *et al.* Tuning two-dimensional nanomaterials by intercalation: materials, properties and applications. *Chem. Soc. Rev.* **6**, 183–191 (2016).
  132. Parades, J. I., Villar-Rodil, S., Martínez-Alonso, A. & Tascón, J. M. D. Graphene oxide dispersions in organic solvents. *Langmuir* **24**, 10560–10564 (2008).
  133. Paton, K. R. *et al.* Scalable production of large quantities of defect-free few-layer graphene by shear exfoliation in liquids. *Nat. Mater.* **13**, 624–630 (2014).
  134. Hummers, W. S. & Offeman, R. E. Preparation of Graphitic Oxide. *J. Am. Chem. Soc.* **80**, 1339–1339 (1958).
  135. Hirata, M., Gotou, T., Horiuchi, S., Fujiwara, M. & Ohba, M. Thin-film particles of graphite oxide 1: High-yield synthesis and flexibility of the particles. *Carbon N. Y.* **42**, 2929–2937 (2004).
  136. Joensen, P., Crozier, E. D., Alberding, N. & Frindt, R. F. A study of single-layer and restacked MoS<sub>2</sub> by X-ray diffraction and X-ray absorption spectroscopy. *J. Phys. C Solid State Phys.* **20**, 4043–4053 (1987).
  137. Joshi, R. K. *et al.* Hydrogen generation via photoelectrochemical water splitting using chemically exfoliated MoS<sub>2</sub> layers. *AIP Adv.* **6**, (2016).
  138. Wu, J. *et al.* Exfoliated 2D Transition Metal Disulfides for Enhanced

- Electrocatalysis of Oxygen Evolution Reaction in Acidic Medium. *Adv. Mater. Interfaces* **3**, 1500669 (2016).
139. Reina, A. *et al.* Large area, few-layer graphene films on arbitrary substrates by chemical vapor deposition. *Nano Lett.* **9**, 30–35 (2009).
  140. Li, X. *et al.* Large-area synthesis of high-quality and uniform graphene films on copper foils. *Science* (80-. ). **324**, 1312–1314 (2009).
  141. Lee, Y.-H. *et al.* Synthesis of Large-Area MoS<sub>2</sub> Atomic Layers with Chemical Vapor Deposition. *Adv. Mater.* **24**, 2320–2325 (2012).
  142. Dumcenco, D. *et al.* Large-Area Epitaxial Monolayer MoS<sub>2</sub>. *ACS Nano* **9**, 4611–4620 (2015).
  143. Zhou, J. *et al.* A library of atomically thin metal chalcogenides. *Nature* **556**, 355–359 (2018).
  144. Kidambi, P. R. *et al.* A Scalable Route to Nanoporous Large-Area Atomically Thin Graphene Membranes by Roll-to-Roll Chemical Vapor Deposition and Polymer Support Casting. *ACS Appl. Mater. Interfaces* **10**, 10369–10378 (2018).
  145. Lim, Y. F. *et al.* Modification of Vapor Phase Concentrations in MoS<sub>2</sub> Growth Using a NiO Foam Barrier. *ACS Nano* **12**, 1339–1349 (2018).
  146. Zhu, D. *et al.* Capture the growth kinetics of CVD growth of two-dimensional MoS<sub>2</sub>. *npj 2D Mater. Appl.* 1–7 (2016). doi:10.1038/s41699-017-0010-x
  147. Skoog, D., Holler, F. J. & Crouch, S. R. *Principles of Instrumental Analysis*. (Thomson Brooks/Cole, 2007).
  148. Harris, D. C. *Quantitative Chemical Analysis*. (W. H. Freeman and Company, 2010).
  149. Ferrari, A. C. & Basko, D. M. Raman spectroscopy as a versatile tool for studying the properties of graphene. *Nat Nanotechnol* **8**, 235–246 (2013).
  150. Wu, J.-B., Lin, M.-L., Cong, X., Liu, H.-N. & Tan, P.-H. Raman spectroscopy of graphene-based materials and its applications in related devices. *Chem. Soc. Rev.* **47**, 1822–1873 (2018).
  151. Ganose, A. M. *et al.* Beyond methylammonium lead iodide: prospects for the emergent field of ns<sup>2</sup> containing solar absorbers. *Chem. Commun.* **103**, 15729–15735 (2016).
  152. Cançado, L. G. *et al.* Quantifying Defects in Graphene via Raman Spectroscopy at Different Excitation Energies. *Nano Lett.* **11**, 3190–3196 (2011).
  153. Lee, C. *et al.* Anomalous lattice vibrations of single-and few-layer MoS<sub>2</sub>. *ACS Nano* **4**, 2695–700 (2010).
  154. Dave, K., Park, K. H. & Dhayal, M. Two-step process for programmable removal of oxygen functionalities of graphene oxide: functional, structural and electrical characteristics. *RSC Adv.* **5**, 95657–95665 (2015).
  155. Yang, D. *et al.* Chemical analysis of graphene oxide films after heat and chemical treatments by X-ray photoelectron and Micro-Raman spectroscopy. *Carbon N. Y.* **47**, 145–152 (2009).
  156. Wang, Q. *et al.* Pyridinic-N-dominated Doped Defective Graphene as Superior Oxygen Electrocatalyst for Ultrahigh-Energy-Density Zn-Air Batteries. *ACS Energy Lett.* **3**, acsenergylett.8b00303 (2018).
  157. Cheng, P., Sun, K. & Hu, Y. H. Memristive Behavior and Ideal Memristor of 1T Phase MoS<sub>2</sub> Nanosheets. *Nano Lett.* **16**, 572–576 (2016).

158. Lei, Z., Zhan, J., Tang, L., Zhang, Y. & Wang, Y. Recent Development of Metallic (1T) Phase of Molybdenum Disulfide for Energy Conversion and Storage. *Adv. Energy Mater.* **1703482**, 1–29 (2018).
159. Bard, A. J. & Faulkner, L. R. *Electrochemical Methods, Fundamentals and Applications*. Wiley (John Wiley & Sons, Inc., 2001).
160. Krol, R. van de & Grätzel, M. *Photoelectrochemical Hydrogen Production*. *Photoelectrochemical Hydrogen Production* **102**, (Springer US, 2012).
161. Elgrishi, N. *et al.* A Practical Beginner's Guide to Cyclic Voltammetry. *J. Chem. Educ.* **acs.jchemed.7b00361** (2017). doi:10.1021/acs.jchemed.7b00361
162. de Levie, R. The electrolysis of water. *J. Electroanal. Chem.* **476**, 92–93 (1999).
163. Roger, I., Shipman, M. A. & Symes, M. D. Earth-abundant catalysts for electrochemical and photoelectrochemical water splitting. *Nat. Rev. Chem.* **1**, 0003 (2017).
164. Voiry, D., Shin, H. S., Loh, K. P. & Chhowalla, M. Low-dimensional catalysts for hydrogen evolution and CO<sub>2</sub> reduction. *Nat. Rev. Chem.* **2**, 0105 (2018).
165. Quaino, P., Juarez, F., Santos, E. & Schmickler, W. Volcano plots in hydrogen electrocatalysis—uses and abuses. *Beilstein J. Nanotechnol.* **5**, 846–854 (2014).
166. Roduner, E. Understanding catalysis. *Chem. Soc. Rev.* **43**, 8226–8239 (2014).
167. Jaegermann, W. & Tributsch, H. Interfacial properties of semiconducting transition metal chalcogenides. *Prog. Surf. Sci.* **29**, 1–167 (1988).
168. Tributsch, H. & Bennett, J. C. Electrochemistry and photochemistry of MoS<sub>2</sub> layer crystals. I. *J. Electroanal. Chem. Interfacial Electrochem.* **81**, 97–111 (1977).
169. Hinnemann, B. *et al.* Biomimetic Hydrogen Evolution: MoS<sub>2</sub> Nanoparticles as Catalyst for Hydrogen Evolution. *J. Am. Chem. Soc.* **127**, 5308–5309 (2005).
170. Kibsgaard, J., Chen, Z., Reinecke, B. N. & Jaramillo, T. F. Engineering the surface structure of MoS<sub>2</sub> to preferentially expose active edge sites for electrocatalysis. *Nat. Mater.* **11**, 963–969 (2012).
171. Ye, G. *et al.* Defects Engineered Monolayer MoS<sub>2</sub> for Improved Hydrogen Evolution Reaction. *Nano Lett.* **16**, 1097–1103 (2016).
172. Li, H. *et al.* Activating and optimizing MoS<sub>2</sub> basal planes for hydrogen evolution through the formation of strained sulphur vacancies. *Nat. Mater.* **15**, 48–53 (2016).
173. Tsai, C. *et al.* Electrochemical generation of sulfur vacancies in the basal plane of MoS<sub>2</sub> for hydrogen evolution. *Nat. Commun.* **8**, 15113 (2017).
174. Tsai, C., Chan, K., Nørskov, J. K. & Abild-Pedersen, F. Theoretical insights into the hydrogen evolution activity of layered transition metal dichalcogenides. *Surf. Sci.* **640**, 133–140 (2015).
175. Li, Y. *et al.* MoS<sub>2</sub> nanoparticles grown on graphene: An advanced catalyst for the hydrogen evolution reaction. *J. Am. Chem. Soc.* **133**, 7296–7299 (2011).
176. Seh, Z. W. *et al.* Combining theory and experiment in electrocatalysis: Insights into materials design. *Science* (80-. ). **355**, eaad4998 (2017).
177. Conway, B. E. & Tilak, B. V. Interfacial processes involving electrocatalytic evolution and oxidation of H<sub>2</sub>, and the role of chemisorbed H. *Electrochim. Acta* **47**, 3571–3594 (2002).
178. PEMFC. *Fuel Cell Today* (2016). Available at: <http://www.fuelcelltoday.com/technologies/pemfc>.
179. Kirubakaran, A., Jain, S. & Nema, R. K. A review on fuel cell technologies and

- power electronic interface. *Renew. Sustain. Energy Rev.* **13**, 2430–2440 (2009).
180. Nie, Y., Li, L. & Wei, Z. Recent advancements in Pt and Pt-free catalysts for oxygen reduction reaction. *Chem. Soc. Rev.* **44**, 2168–201 (2015).
  181. Ambrosi, A. *et al.* Graphene and its electrochemistry – an update. *Chem. Soc. Rev.* **45**, 2458–2493 (2016).
  182. Gong, K., Du, F., Xia, Z., Durstock, M. & Dai, L. Nitrogen-Doped Carbon Nanotube Arrays with High Electrocatalytic Activity for Oxygen Reduction. *Science* (80-. ). **323**, (2009).
  183. Sheng, Z. H. *et al.* Catalyst-free synthesis of nitrogen-doped graphene via thermal annealing graphite oxide with melamine and its excellent electrocatalysis. *ACS Nano* **5**, 4350–4358 (2011).
  184. Lin, Z., Waller, G., Liu, Y., Liu, M. & Wong, C. P. Facile synthesis of nitrogen-doped graphene via pyrolysis of graphene oxide and urea, and its electrocatalytic activity toward the oxygen-reduction reaction. *Adv. Energy Mater.* **2**, 884–888 (2012).
  185. Lai, L. *et al.* Exploration of the active center structure of nitrogen-doped graphene-based catalysts for oxygen reduction reaction. *Energy Environ. Sci.* **5**, 7936 (2012).
  186. Jeon, I. Y. *et al.* Formation of large-area nitrogen-doped graphene film prepared from simple solution casting of edge-selectively functionalized graphite and its electrocatalytic activity. *Chem. Mater.* **23**, 3987–3992 (2011).
  187. Li, Y. *et al.* An oxygen reduction electrocatalyst based on carbon nanotube–graphene complexes. *Nat. Nanotechnol.* **7**, 394–400 (2012).
  188. Maldonado, S. & Stevenson, K. J. Influence of nitrogen doping on oxygen reduction electrocatalysis at carbon nanofiber electrodes. *J. Phys. Chem. B* **109**, 4707–4716 (2005).
  189. Kundu, S. *et al.* Electrocatalytic Activity and Stability of Nitrogen-Containing Carbon Nanotubes in the Oxygen Reduction Reaction. *J. Phys. Chem. C* **113**, 14302–14310 (2009).
  190. Yu, D., Zhang, Q. & Dai, L. Highly efficient metal-free growth of nitrogen-doped single-walled carbon nanotubes on plasma-etched substrates for oxygen reduction. *J. Am. Chem. Soc.* **132**, 15127–15129 (2010).
  191. Rao, C. V., Cabrera, C. R. & Ishikawa, Y. In search of the active site in nitrogen-doped carbon nanotube electrodes for the oxygen reduction reaction. *J. Phys. Chem. Lett.* **1**, 2622–2627 (2010).
  192. Liu, R., Wu, D., Feng, X. & Müllen, K. Nitrogen-doped ordered mesoporous graphitic arrays with high electrocatalytic activity for oxygen reduction. *Angew. Chemie - Int. Ed.* **49**, 2565–2569 (2010).
  193. Yasuda, S., Yu, L., Kim, J. & Murakoshi, K. Selective nitrogen doping in graphene for oxygen reduction reactions. *Chem. Commun. (Camb)*. **49**, 9627–9 (2013).
  194. Geng, D. *et al.* High oxygen-reduction activity and durability of nitrogen-doped graphene. *Energy Environ. Sci.* **4**, 760 (2011).
  195. Zheng, B., Wang, J., Wang, F. B. & Xia, X. H. Synthesis of nitrogen doped graphene with high electrocatalytic activity toward oxygen reduction reaction. *Electrochem. commun.* **28**, 24–26 (2013).
  196. Zhang, L. & Xia, Z. Mechanisms of oxygen reduction reaction on nitrogen-doped



- graphene for fuel cells. *J. Phys. Chem. C* **115**, 11170–11176 (2011).
197. Zhang, L., Niu, J., Dai, L. & Xia, Z. Effect of microstructure of nitrogen-doped graphene on oxygen reduction activity in fuel cells. *Langmuir* **28**, 7542–7550 (2012).
  198. Meyer, J. C. *et al.* Direct imaging of lattice atoms and topological defects in graphene membranes. *Nano Lett.* **8**, 3582–3586 (2008).
  199. Feng, Y. *et al.* Tuning the catalytic property of nitrogen-doped graphene for cathode oxygen reduction reaction. *Phys. Rev. B - Condens. Matter Mater. Phys.* **85**, 1–5 (2012).
  200. Ni, S., Li, Z. Y. & Yang, J. L. Oxygen molecule dissociation on carbon nanostructures with different types of nitrogen doping. *Nanoscale* **4**, 1184–1189 (2012).
  201. Wang, L., Ambrosi, A. & Pumera, M. ‘Metal-free’ catalytic oxygen reduction reaction on heteroatom-doped graphene is caused by trace metal impurities. *Angew. Chemie - Int. Ed.* **52**, 13818–13821 (2013).
  202. Wang, L. & Pumera, M. Residual metallic impurities within carbon nanotubes play a dominant role in supposedly ‘metal-free’ oxygen reduction reactions. *Chem. Commun.* **50**, 12662–12664 (2014).
  203. GAMRY. Understanding iR Compensation. *Gamry Appl. Notes* 1–19 (2014).
  204. Singh, R. K., Devivaraprasad, R., Kar, T., Chakraborty, A. & Neergat, M. Electrochemical Impedance Spectroscopy of Oxygen Reduction Reaction (ORR) in a Rotating Disk Electrode Configuration: Effect of Ionomer Content and Carbon-Support. *J. Electrochem. Soc.* **162**, F489–F498 (2015).
  205. *Nanofabrication Handbook*. (CRC Press, Taylor & Francis Group, 2012).
  206. *Handbook of Nanofabrication*. (Elsevier B.V., 2010).
  207. Bolotin, K. I. *et al.* Ultrahigh electron mobility in suspended graphene. *Solid State Commun.* **146**, 351–355 (2008).
  208. Voiry, D. *et al.* The role of electronic coupling between substrate and 2D MoS<sub>2</sub> nanosheets in electrocatalytic production of hydrogen. *Nat. Mater.* **15**, 1003–1009 (2016).
  209. Xiang, Q., Yu, J. & Jaroniec, M. Synergetic effect of MoS<sub>2</sub> and graphene as cocatalysts for enhanced photocatalytic H<sub>2</sub> production activity of TiO<sub>2</sub> nanoparticles. *J. Am. Chem. Soc.* **134**, 6575–8 (2012).
  210. Hong, J. *et al.* Exploring atomic defects in molybdenum disulphide monolayers. *Nat. Commun.* **6**, 1–8 (2015).
  211. Voiry, D. *et al.* High-quality graphene via microwave reduction of solution-exfoliated graphene oxide. *Science (80-. )*. **3398**, 1–7 (2016).
  212. Martinez, U. *et al.* Critical role of intercalated water for electrocatalytically active nitrogen-doped graphitic systems. *Sci. Adv.* **2**, 1–7 (2016).
  213. Guo, B. *et al.* Controllable N-doping of graphene. *Nano Lett.* **324**, 4975–4980 (2010).
  214. Song, C. & Zhang, J. Electrocatalytic Oxygen Reduction Reaction. *PEM Fuel Cell Electrocatal. Catal. Layers Fundam. Appl.* 89–129 (2008). doi:10.1007/978-1-84800-936-3\_2
  215. Lin, Z. *et al.* 2D materials advances: From large scale synthesis and controlled heterostructures to improved characterization techniques, defects and applications.

- 2D Mater.* **3**, 042001 (2016).
216. Susi, T., Pichler, T. & Ayala, P. X-ray photoelectron spectroscopy of graphitic carbon nanomaterials doped with heteroatoms. *Beilstein J. Nanotechnol.* **6**, 177–192 (2015).
  217. Lin, L. W. & He, Y. H. Synthesis and optical property of ultra-long alpha-Si<sub>3</sub>N<sub>4</sub> nanowires under superatmospheric pressure conditions. *CrystEngComm* **14**, 3250 (2012).
  218. Lu, Z. *et al.* High-efficiency oxygen reduction to hydrogen peroxide catalysed by oxidized carbon materials. *Nat. Catal.* (2018). doi:10.1038/s41929-017-0017-x
  219. Shao, Y. *et al.* Nitrogen-doped graphene and its electrochemical applications. *J. Mater. Chem.* **20**, 7491 (2010).
  220. Li, J. *et al.* Electron–Hole Symmetry Breaking in Charge Transport in Nitrogen-Doped Graphene. *ACS Nano* **11**, 4641–4650 (2017).
  221. Liu, Y. *et al.* Self-optimizing, highly surface-active layered metal dichalcogenide catalysts for hydrogen evolution. *Nat. Energy* **6**, 17127 (2017).

## Appendix. Acknowledgement of Previous Publications

This thesis dissertation is comprised of results from articles which have previously been published. Chapters 5 and 6 discuss experimental results that have been published in Voiry, D., Fullon, R., Yang, J., de Carvalho Castro e Silva, C., Kappera, R., Bozkurt, I., ... Chhowalla, M. (2016). The role of electronic coupling between substrate and 2D MoS<sub>2</sub> nanosheets in electrocatalytic production of hydrogen. *Nature Materials*, 15(9), 1003–1009. <http://doi.org/10.1038/nmat4660>.<sup>208</sup> Additionally some of the results mentioned in Chapter 7 have been published in Voiry, D., Yang, J., Kupferberg, J., Fullon, R., Lee, C., Jeong, H. Y. Y., ... Chhowalla, M. (2016). *Science*, 3398(September), 1–7. <http://doi.org/10.1126/science.aah3398>.<sup>211</sup>